Investigating the three-nucleon force through ^{10}C(p,p)^{10}C

By

Amit Kumar

A Thesis Submitted to
Saint Mary's University, Halifax, Nova Scotia
in Partial Fulfillment of the Requirements for
the Degree of Master of Science in Applied Science

in

August, 2015, Halifax, Nova Scotia

Approved :	Dr. Rituparna Kanungo Supervisor
Approved :	Dr. David Guenther Examiner
Approved :	Dr. Reiner Krücken Examiner
Approved :	Dr. David Hornidge Examiner
Date :	4$^{\text{th}}$ August, 2015

Abstract

Investigating the three-nucleon force through ^{10}C(p,p)^{10}C

By Amit Kumar

Abstract: We present the first effort to understand the effect of the three-nucleon force on the angular distribution of nucleus-proton scattering near the drip-line. We successfully performed the elastic scattering of the unstable nucleus ^{10}C with a proton target using the ISAC Charged Particle Reaction Spectroscopy Station (IRIS) facility stationed at TRIUMF, Canada. The facility utilizes a novel thin windowless solid H_2 target which made the reaction study possible with a beam intensity of $\sim 2.5\times10^3$ pps. The angular distribution measurement was based on the detection of the protons with the thin Si and CsI(Tl) detectors. We compared the measured cross section with the predictions made by *ab initio* no core shell model with continuum (NCSMC) based on the chiral NN (N^3LO) and 3N (N^2LO) forces. The study shows that the measured angular distribution is in better agreement with the theoretical prediction based on the chiral NN+3N forces.

August 4, 2015

Acknowledgment

Firstly, I would like to thank my supervisor, Prof. Rituparna Kanungo, for her constant guidance and support throughout the academic year both inside and outside the workplace. Thanks for showing me the beautiful TRIUMF and introducing me to the colleagues at TRIUMF. I am also grateful to her for providing me the opportunity to work with this challenging project that she gave me.

I would also like to express my sincere gratitude to my committee members: Dr. David Guenther, Dr. Reiner Krücken, and Dr. David Hornidge for their advice and support during my research.

Thanks to everyone I met at TRIUMF. To Alisher, for the valuable physics discussions and help me during my data analysis. To Martin, for his valuable insight during the research group meetings and for introducing me to sushi for the first time. Thanks for going through electronics and explaining the triggers and gate logics. Thanks to Ishimoto-san for the target system discussion, it was a pleasure working with you, thanks for introducing me the ramen. Thanks to Dr. Petr Navratil for his patience in hearing my never ending questions and providing me with a satisfactory answers. Thanks to the Borommeanies team for making the summer even more enjoyable and lively.

Thanks to everybody at Saint Mary's University. Thanks to Dr. Adam Sarty for teaching the "Radiation Detection Techniques" course which was extremely helpful. To Jaspreet, for introducing me to the graduate students at the Astronomy and Physics Department. Thanks for all the lively discussions we had on physics, being always there to listen to my problems and sharing the load, and encouraging me to follow my dream. It was extremely smooth and fun to explore

the Halifax (especially waterfront) and Vancouver. To Maan, for great times we had at work and outside, for being always supportive and making me drunk quite a few times. Thanks to Dr. Daniel Majaess, I learned a lot as Teaching Assistant, and it was pleasure to work with you. Thanks to Gream, Ismat and Dijana, I had a great time with you guys.

Finally, a big thank you to my family. To my sister for reminding me that there is a lot to explore outside the academia. Thanks to my parents, for their constant support, having faith on me, and encouraging me to pursue the things I enjoy.

Dedicated to my mother and father

Contents

1 Introduction **1**

2 Theoretical Formalism **8**

2.1 General properties of the nuclear force 8

2.2 Nuclear shell model 9

2.3 Meson exchange theory 11

2.4 Chiral perturbation theory 17

2.5 Towards *ab initio* theory 19

3 Experiment and Methodology **24**

3.1 Radioactive Ion Beam production at TRIUMF 24

3.2 IRIS 25

3.2.1 Ionization Chamber 25

3.2.2 Solid H_2 Target 26

3.2.3 Charged particle detectors 28

3.2.4 Scintillator and SSB detectors 29

3.3 Signal Processing and Trigger Logic 30

4 Analysis of elastic scattering ^{10}C(p,p)^{10}C **36**

4.1 Identification of beam particles 36

4.2 Detector Calibration 37

4.2.1 Silver foil thickness determination 38

4.2.2 S3d1 and S3d2 detectors 39

4.2.3 YY1 detector 45

4.2.4 Monitoring the solid H_2 target thickness 48
4.2.5 CsI(Tl) detector 51
4.3 Particle identification using ΔE-E analysis 56
4.4 Kinematics of protons 57
4.5 Excitation energy spectrum for ^{10}C 58
4.6 Measurement of differential cross section 61
4.6.1 Counting scattering flux 61
4.6.2 Counting incident flux 63
4.6.3 Solid angle 64
4.6.4 Geometric efficiency correction 65
4.6.5 Uncertainty in the measurement of differential cross section . 66

5 Results and Discussion **70**

5.1 Differential cross section 70

List of Figures

1.1 Binding energy of light nuclei. Experimental value (green) are compared with Green's function Monte Carlo calculations using only NN potential (AV18, blue) and with the addition of a 3N potential (IL7, yellow) [5–7]. 3

1.2 Energy levels in ^{10}B: NCSM/SRG calculations based on chiral NN and 3N forces [14]. 4

1.3 Nuclear Chart for light nuclei. The location of ^{10}C at the proton drip-line is marked by the blue circle. The blue line shows the proton drip-line. Data taken from the National Nuclear Data Center at Brookhaven National Laboratory [18]. 6

2.1 Energy levels in a nucleus using nuclear potential with Woods-Saxon and spin-orbit terms. 10

2.2 Nuclear force as exchange of pions between nucleons. (i) The one-pion exchange diagram. (ii) The two-pion exchange diagram [29]. . 13

2.3 A few examples of the three-nucleon force. (i) The Fujita-Miyazawa 3NF involves the excitation of one of the nucleon to a Δ particle accompanied by exchange of two pions. (ii) The two-pion exchange through S-wave excitation. (iii) The three-pion exchange with one Δ excitation state. (iv) The three-pion exchange with two Δ excitation states [29]. 16

2.4 The nuclear potential derived from chiral perturbation theory. The solid lines and dashed lines represent the nucleon and the pion, respectively. To differentiate the different vertex factors involved in interaction diagrams, small dot, large dot, solid square and solid star have been used. Terms at leading order, next-to-leading order, next-to-next-to-leading order, and next-to-next-to-next-to-leading order are represented by LO, NLO, N^2LO, and N^3LO, respectively [1]. 18

2.5 NCSM calculations for light nuclei. (a) Energy levels in ^{7}Li using CD-Bonn potential (NN) [86]. Energy levels in ^{10}B and ^{11}B based on NN and NN+NNN potentials [14]. (b) Energy levels in ^{12}C and ^{13}C based on NN and NN+NNN potentials [14]. The excitation energies are in MeV. Note, the ordering of energy levels in the ^{10}B depends on the three-nucleon (3N) interaction. 21

3.1 IRIS setup. 25

3.2 Design of the IRIS Ionization Chamber. 26

3.3 Solid H_2 target assembly. (a) Silver foil on copper cell. (b) View of copper cell. (c) Copper cell placed inside the cylindrical heat shield [88]. 28

3.4 Detectors for target-like nuclei. (a) YY1 detector. (b) CsI(Tl) detector. 29

3.5 S3d1 and S3d2 detector. 30

3.6 Pulse processing. (a) Output from a preamplifier unit and a shaping amplifier for a general detector. (b) Output from the shaping amplifier for CsI(Tl), SSB, IC, Pulser, and scintillator. 33

3.7 Output from the shaping amplifier for S3d1, S3d2 and YY1 detector. 34

3.8 Formation of trigger logic and analog to digital conversion to record the data. 35

4.1 ADC spectrum of IC. (a) For 8 Torr pressure. (b) For 19.5 Torr pressure. 37
4.2 Layout of material layers for the energy loss calculation in the SSB detector. 39
4.3 ADC spectrum of the SSB detector with SSB trigger. (a) The peak of ^{10}C particles using the IC ^{10}C events gate. (b) The peak of ^{10}B particles using the IC ^{10}B events gate. 40
4.4 Relative gain difference found using equation 4.3 and 4.4 versus thickness of Ag foil thickness. 40
4.5 Layout of material layers for energy loss calculation in the S3d1 and S3d2 detectors in the absence of solid H_2 target. 41
4.6 Energy loss calculation in the S3d1 and S3d2 detector. (a) For ^{10}C particle. (b) For ^{10}B particle. 41
4.7 Calibration of the S3d1 detector. (a) Pedestal data for the first ring. (b) Gaussian fitting of ^{10}C peak in ADC spectrum for first ring. (c) ADC spectrum for ^{10}C events in the outermost ring of S3d1 detector at 19.5 Torr IC pressure (without SHT target). . . . 43
4.8 The parameter check for the S3d1 detector calibration. 43
4.9 Calibration of the S3d2 detector. (a) Pedestal data for first ring of the S3d2 detector. (b) ADC spectrum for the first ring of the S3d2 detector at 19.5 Torr IC pressure setting. 44
4.10 Calibration of the YY1 detector. The top panel shows the ADC spectrum and Gaussian fitting to the peak. The bottom panel shows the least square fit to the standard calibration equation 4.2 where three data points correspond to three alpha peaks. 46
4.11 Plot of ΔE-E for protons from ^{10}C+p elastic scattering (for incident ^{10}C energy 48.6 MeV and 100 μm SHT). ΔE and E represent the energy deposited by proton in silicon and CsI(Tl) detectors, respectively. 47

4.12 Illustration of different region where energy losses must be taken into account to find SHT thickness. Note that the ^{10}C particles stop in the S3d1 detector for the 19.5 Torr IC pressure condition. . 49
4.13 The solid H_2 target thickness determined throughout the experiment. 51
4.14 Selection of the proton events generated from the scattering of the ^{10}C particle with protons in the solid H_2 target. (a) Proton event selection from ^{10}C beam particle using silicon and CsI(Tl) detector. (b) Selection of elastic proton events from $^{10}C + p$ scattering using CsI(Tl) detector. 52
4.15 Material layers to account for energy loss for the purpose of calibration of CsI(Tl) detector. 53
4.16 Kinematics of the proton from elastic scattering of ^{10}C (E_{lab}=48.6 MeV) with the solid H_2 target. The quantity E on Y-axis represents the energy at the entrance of the CsI(Tl) detector after energy loss in the target and detector dead layers. 54
4.17 CsI(Tl) ADC spectrum for one of the 16 crystals in CsI(Tl) array to find the proton's peak. ^{10}C IC gate (figure 4.1b) and proton events inside the polygon (figure 4.14a and 4.14b) as condition have been used to select the protons from ^{10}C+p elastic scattering. (a) For YY1 rings 1-4. (b) For YY1 rings 5-8. (c) For YY1 rings 9-12. (d) For YY1 rings 13-16. 54
4.18 The measured energy (E in CsI(Tl)) and scattering angle of the scattered protons from the ^{10}C+p elastic scattering. The black curve shows the calculated values. 55
4.19 Particle identification plot for the light target-like particles. Events inside the polygon are protons. ΔE and E represent the energy deposited in silicon (YY1) and CsI(Tl) detectors, respectively. . . . 56
4.20 Particle Identification plot for heavy particles in the experiment. . 57

4.21 Plot of proton energy deposited in the detectors versus laboratory angle. 58
4.22 Q-value spectrum of ^{10}C(p,p)^{10}C reaction. (a) Data at 19.5 Torr IC pressure setting. We have used proton events inside polygon (see figure 4.19) and ^{10}C IC events (see figure 4.1b) as gate. (b) Data at 8 Torr IC pressure setting. We have used proton events inside polygon (see figure 4.19) and ^{10}C IC events (see figure 4.1a) as gate. 60
4.23 Full-width at half-maxima (FWHM) for the ground state of ^{10}C. . 60
4.24 Q-value spectrum for ^{10}C(p,p)^{10}C reaction at IC pressure of 19.5 Torr for the first ring of the YY1. The two vertical dashed lines show the 3σ range around the peak position. 63
4.25 DAQ live-time for data runs at 8 Torr IC pressure setting. 65
4.26 Simulated geometric efficiency of YY1/CsI(Tl) detector. 66
4.27 Differential cross section in laboratory frame for ^{10}C(p,p)^{10}C elastic reaction. (a) For incident ^{10}C energy E_{lab} = 48.21 MeV (8 Torr IC pressure setting). (b) For incident ^{10}C energy E_{lab} = 45.45 MeV (19.5 Torr IC pressure setting). 68
4.28 (a) The plot of centre-of-mass scattering angle versus scattering angle in the laboratory frame. Detector coverage is shown by two vertical dashed lines. (b) The Jacobian of the transformation from the laboratory frame to the centre-of-mass frame. 69

5.1 The differential cross section of ^{10}C(p,p)^{10}C elastic reaction. The solid curves (blue and black) represent the NCSMC calculations: The black solid curve shows the calculation based on the chiral NN force (N^{3}LO), and the blue curve shows the calculation based on the chiral NN + 3N force (NN-N^{3}LO + 3N-N^{2}LO). The red dots represent the data points from the experiment. (a) For E_{cm} = 4.4 MeV. (b) For E_{cm} = 4.16 MeV. 71

List of Tables

2.1 History of Nuclear Force. *Source*: Adapted from Ref. [1]. 12

2.2 Properties of the deuteron in its ground state using phenomenological NN potential models [43]. 14

2.3 Ground state triton's binding energy using phenomenological NN potential models [45]. 15

2.4 Binding energies of light nuclei in MeV using NN (AV18) and using NN+3N potential. Inclusion of 3N potential provides a comparable result [6]. 16

4.1 Standard triple alpha source energies. 45

4.2 Kinematic calculations for nuclear reactions. The KE_{min}^{lab} is the energy (in laboratory frame) required to initiate the given reaction with proton as target at rest. Expression for Q-value is given in equation 4.9. 57

Glossary

χPT	Chiral perturbation theory
2NF	Two-nucleon force
3N	Three-nucleon
3NF	Three-nucleon force
4NF	Four-nucleon force
ADC	Analog to digital converter
AV18	Argonne version-18
BE	Binding energy
CCM	Coupled-cluster method
CD-Bonn	Charge dependent Bonn
CM	Center-of-mass
CR	Capacitor-resistor
DAQ	Data acquisition live-time
EFT	Effective field theory
FWHM	Full-width at half-maxima
GFMC	Green's Function Monte Carlo Method
HO	Harmonic Oscillator
IC	Ionization Chamber
IL2	Illinois-2
IL7	Illinois-7
ISAC	Isotope Separator and Accelerator
ISOL	Isotope separation on-line method
IRIS	ISAC Charged Particle Reaction Spectroscopy Station
LED	Leading edge discriminator
LO	Leading order
MC	Monte Carlo

NCFC	No-core full configuration
NCSM	No-core shell model
NCSMC	No-core shell model with continuum
Nijm	Nijmegen
NLO	Next-to-leading order
N^2LO	Next-to-next-to-leading order
N^3LO	Next-to-next-to-next-to-leading order
NN	Nucleon-Nucleon
NNN	Three-nucleon
OBE	One-boson-exchange
OPEP	One-pion exchange potential
PMT	Photomultiplier tube
QCD	Quantum Chromodynamics
RC	Resistor-capacitor
RGM	Resonating group method
RIB	Radioactive ion beam
S3d1	Label for ΔE silicon detector (to detect beam-like particles)
S3d2	Label for E silicon detector (to detect beam-like particles)
SHT	Solid H_2 target
SNR	Signal-to-noise ratio
SRG	Similarity resonating group method
SSB	Silicon surface barrier detector
TM	Tucson-Melbourne
TM'	Tucson-Melbourne revised
TPEP	Two-pion exchange potential
VMC	Variational Monte Carlo
YY1	Label for ΔE silicon detector (to detect target-like particles)

Chapter 1

Introduction

The study of the nuclear force has been an interesting subject since the discovery of the atomic nucleus in 1909 by Rutherford through his famous gold foil experiment. It has attracted both theory as well as experiment. As scientists have probed deeper and deeper into the structure of the nucleus, it has shed light in understanding the behaviour of the nuclear force, and how the nuclei have come into existence. Nuclear physics encompasses the study of a diverse spectrum of phenomena: from fundamental interaction between quarks inside nucleons to the formation of chemical elements inside objects in our universe such as stars or supernovae. Study of these physical phenomena have led to the production of radioactive beams and establishment of experimental facilities. These developments have not only helped the scientific community to enhance its understanding about the physical processes occurring in nature but have also impacted and revolutionized other fields such as: medical science especially cancer treatment, nuclear energy production, semiconductor manufacturing, material science, archaeology and art.

Our current understanding dictates that the nuclear force, which is defined as a force between nucleons inside a nucleus is a residual effect of the strong force, which is an attractive force that bind particles known as quarks together, to form the nucleon itself. The fundamental theory behind the strong interaction is quantum

chromodynamics (QCD), which shows a non-perturbative[1] nature in the length scale relevant to nuclear physics [1]. Hence it is extremely challenging to give a complete description of the nuclear force from the fundamental constituent quarks and gluons. In nuclear physics, the interest is in understanding the evolution of structure in complex many-body nuclei from different observables such as binding energy (BE), charge distribution, nuclear spin, magnetic dipole moment and differential cross section [2]. To compute these observables theoretically, we construct an N-body problem in terms of the non-relativistic Schrödinger equation. In a first approximation, for the light nuclei a two-nucleon potential is sufficient to describe observables at low energies. Currently, a number of phenomenological nucleon-nucleon (NN) models exist that provide an accurate description of the NN-scattering data with a $\chi^2 \sim 1$. Recent studies have shown that for a three or more than three-nucleon system the existing NN-potential model either underestimates or overestimates the experimental value of the observables. One of the simplest and most extensively studied three-nucleon system is the triton. Calculations based solely on two-nucleon force (2NF) are well known to underestimate the binding energy[2] of triton [3, 4]. Similar discrepancies have been found in other light nuclei as well [5–7]. This can be seen in figure 1.1. Here the binding energies of light nuclei calculated using the two-body force and the three-body force have been compared with the experimental values. This clearly shows the importance of the three-nucleon force (3NF) and indicates the need to go beyond the two-body force.

Nowadays, understanding the effects and determining the properties of the 3NF is one of the important issues in nuclear physics. The 3NF cannot be reduced to pair-wise NN interaction and arises naturally in the meson-exchange theory and effective field theory (EFT) based on the symmetries of quantum chromodynamics (QCD). At present, various phenomenological 3NF models exist such as Tucson-Melbourne (TM) and Urbana-IX, both of which are typically based on the two-pion

[1] Small approximation is not valid.

[2] Energy required to disassemble a nucleus into its constituents.

exchange [8–10]. Despite their remarkable successes, there are various problems still unresolved. For instance, phenomenological NN potentials roughly involve 40-50 parameters and the three-nucleon (3N) potential requires an additional 5 parameters. In addition, these phenomenological models lack the relation to the fundamental underlying theory QCD. To resolve these issues, an alternate theory known as chiral effective field theory has been developed which is linked to QCD via its symmetries. This framework allows one to analyze the low-energy properties of hadronic systems in a systematic way. It also offers a natural explanation for the observed hierarchy of nuclear forces: $V_{2N} \gg V_{3N} \gg V_{4N}$, where V_{2N}, V_{3N}, and V_{4N} are the two-nucleon, three-nucleon, and four-nucleon potentials, respectively.

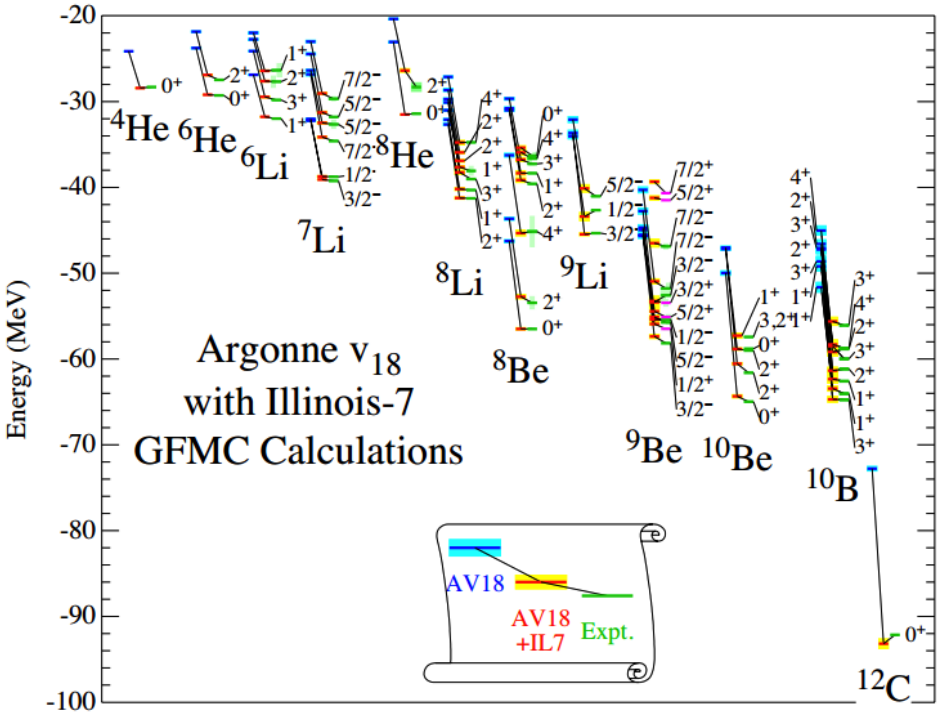

Fig. 1.1. Binding energy of light nuclei. Experimental value (green) are compared with Green's function Monte Carlo calculations using only NN potential (AV18, blue) and with the addition of a 3N potential (IL7, yellow) [5–7].

The ultimate aim of nuclear physics is to construct a model with a firm connection to quantum chromodynamics that can explain all known properties of existing nuclei. Such models fall under the category of *ab initio* theory of nuclear physics. Green's Function Monte Carlo Method (GFMC), No-core shell model with similarity resonating group method (NCSM/SRG) and No-core full config-

uration (NCFC) are few such methods. The NCSM has been applied to various light nuclei ($A \leq 20$) to probe the effects of three-nucleon force [11–13]. So far it has been extremely successful in explaining the binding energy and excitation spectra of light nuclei.

These calculations have shown that nuclei with mass number $A = 10$ possess interesting properties. For instance, figure 1.2 shows the NCSM/SRG calculation for energy levels in ^{10}B using chiral NN and 3N forces. We observe that there is an inversion of the $J^\pi = 1^+$ and $J^\pi = 3^+$ with the prediction using the three-nucleon force being consistent with the experiment. So far the three-nucleon force using the NCSM/SRG model has been investigated through the study of observables that are intrinsic to nuclei, but its effects have not been studied extensively in scattering observables such as differential cross section and analyzing power. Very

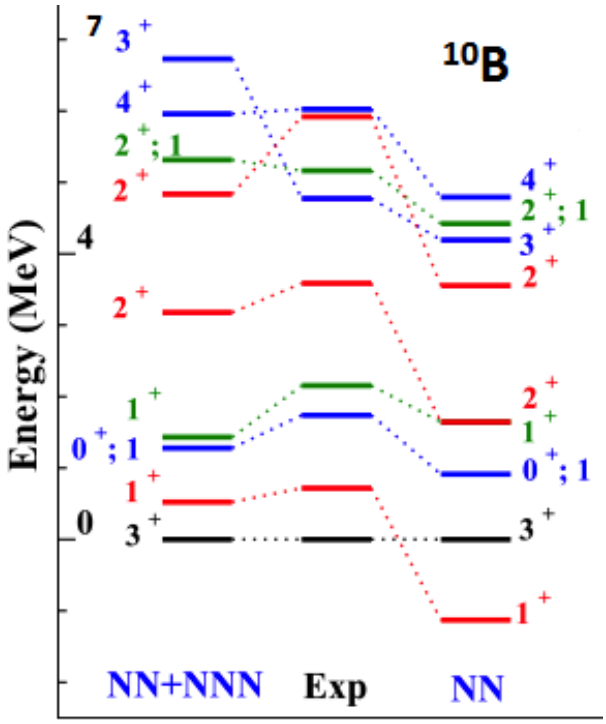

Fig. 1.2. Energy levels in ^{10}B: NCSM/SRG calculations based on chiral NN and 3N forces [14].

recently it has been possible to calculate the elastic and inelastic scattering angular distribution cross sections within the framework of chiral effective theory [15, 16]. The technique that has emerged is known as *ab initio* no core shell model with

continuum (NCSMC). The NCSMC model has been applied successfully to study the effect of 3NF on differential cross section of ^{4}He(d,d)^{4}He, ^{4}He(p,p)^{4}He, and ^{4}He(n,n)^{4}He [16, 17]. The *ab-initio* reaction theory development is still in its infancy and hence there is an ample amount of research going on in this frontier. There have not been any investigations on the effect of three-nucleon force on scattering observables for nuclei close to the proton or neutron drip-lines (the lines beyond which nuclei are particle-unbound). This motivates our study of $^{10}C + p$ elastic scattering since as discussed above a significant effect of 3NF has been seen in the level ordering in the $A = 10$ nucleus ^{10}B. In terms of computation it is less challenging to perform *ab initio* calculations for ^{10}C because it has a smaller number of excitation states. The reaction of ^{10}C with proton forms ^{11}N, an unstable compound nucleus as intermediate nucleus that also has fewer resonance states. So, these features motivate our choice of ^{10}C for studying the effect of the three-nucleon force in the scattering process. The chart of light nuclei is shown in figure 1.3. We have shown the proton-drip line, which is defined as point beyond which addition of one- or more than one- proton causes the nucleus to become unbound. The ^{10}C has 6 protons and 4 neutrons and it is located at proton drip line of the $N = 4$ isotones.

The scientific motivation of this thesis is to investigate the role of three-nucleon force through ^{10}C(p,p)^{10}C elastic scattering reaction. Using an *ab inito* NCSMC method based on chiral forces, the calculation for differential cross section of ^{10}C(p,p)^{10}C reaction has been done in collaboration with the TRIUMF theory group. Our aim is to measure the differential elastic scattering cross-section through ^{10}C(p,p)^{10}C for the first time using experimental facility IRIS located at TRIUMF, Canada, which will help us in understanding the role of three-nucleon force and hence shall provide guidance to *ab initio* reaction theory.

The subsequent chapters of this thesis are organized in the following manner:

- Chapter 2 presents brief theoretical background, which has lead us towards the *ab intio* theory. I shall give an informal introduction to chiral perturba-

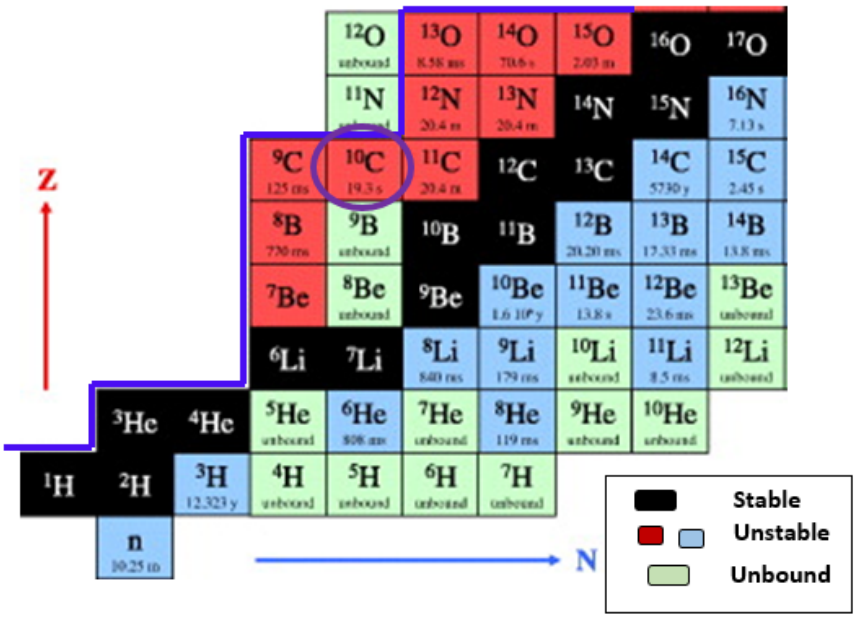

Fig. 1.3. Nuclear Chart for light nuclei. The location of ^{10}C at the proton drip-line is marked by the blue circle. The blue line shows the proton drip-line. Data taken from the National Nuclear Data Center at Brookhaven National Laboratory [18].

tion theory and explain qualitatively how NN and 3N forces are manifested inside nuclei. I shall also provide a brief account to the *ab initio* no core shell model with continuum to study observables related to nuclear reaction and nuclei itself.

- Chapter 3 gives an account of the experimental setup necessary for studying the ^{10}C(p,p)^{10}C elastic scattering. The end of this chapter focuses on the electronics and data acquisition components required to acquire and store the data for analysis of our reaction.

- Chapter 4 will discuss the techniques used in the analysis of the data obtained from our experiment. It includes the calibration of our detectors, monitoring solid H_2 target thickness, particle identification event by event, measuring the excitation energy of ^{10}C, and counting the incident beam particles using an Ionization Chamber (IC) scaler, and counting the scattered elastic protons to measure the differential cross section.

- Chapter 5 will discuss the results obtained from our experiment and com-

pare them with the theoretical predictions of angular distributions of $^{10}C+p$ elastic scattering using the newly developed *ab initio* reaction theory. The theoretical work is also a part of this project, developed by our theory collaborators with P. Navratil.

Chapter 2

Theoretical Formalism

To understand the exact nature of the nuclear force and use it to provide a unified description of properties of light and heavy nuclei is one of the primary goals of nuclear physics. In this chapter we present a brief review of studies done to explore the nuclear force.

2.1 General properties of the nuclear force

The basic properties of the nuclear force are the following [19]:

1. The nuclear force is a short range force (< 2 fm) in contrast to the electromagnetic force and gravitational forces. If it were a long range force, one would expect the binding energy of nuclei to increase with mass number.

2. The nuclear force is attractive at intermediate ranges ($1 < r < 2$ fm), where the attractive nature can be clearly seen from the nuclear binding energy.

3. The nuclear force shows repulsive nature at short distances (< 1 fm).

4. The nuclear force is independent of electric charge, i.e. nuclear force between n-n, n-p or p-p pairs is same.

5. The nuclear force possesses tensor characteristics, which can be clearly seen in the deuteron quadruple moment and the so-called D/S ratio (D-state to S-state wavefunction ratio) of the deuteron [20].

6. The nuclear force is spin dependent.

2.2 Nuclear shell model

Nuclear shell model was proposed by Maria Goeppert-Mayer and J. Jensen more than 60 years ago [21, 22] in order to explain the "magic number" (number of protons or neutrons) 2, 8, 20, 28, 50, 82, 126 appearing in a number of studies such as the binding energies of nuclei, the number of stable isotones with respect to neutron number, the first excited state energies of even-even nuclei, the neutron separation energy with respect to neutron number and nucleon capture cross section. The shell model considers each nucleon to be moving in an effective potential created by all the other nucleons present inside nucleus. If this is the case, the nuclear potential should be roughly proportional to the nuclear matter density. Experimental data suggest that the nuclear potential ($V_{\text{ws}}(r)$) has following form [23]:

$$V_{\text{ws}}(r) = \frac{-V_0}{1 + e^{(\frac{r-R}{a})}} \tag{2.1}$$

where V_0 is the potential well depth ($\sim$ 50 MeV), $R = r_0 A^{\frac{1}{3}}$ is the nuclear radius, A is the mass number, r_0 is a constant = 1.25 fm, and a is surface thickness ($\sim$ 0.5 fm). The nuclear potential $V_{\text{ws}}(r)$ given in equation 2.1 is also known as Woods-Saxon potential. On adding a spin-orbit interaction term arising from the interaction between orbital motion of nucleon and its intrinsic spin, the effective potential becomes:

$$V(r) = \frac{-V_0}{1 + e^{(\frac{r-R}{a})}} + W(r)\vec{L} \cdot \vec{S} \tag{2.2}$$

where $\vec{L}$ and $\vec{S}$ are orbital angular momentum operator and intrinsic spin operator, respectively. The second term in equation 2.2 is the spin-orbit potential where $W(r) = \frac{1}{r}\frac{dV_{\text{ws}}(r)}{dr}$. Using this potential model (equation 2.2) the energy levels can be found as shown in figure 2.1. The energy levels are labelled using quantum number j, m_j, l, s, where s is intrinsic spin quantum number, l is orbital angular

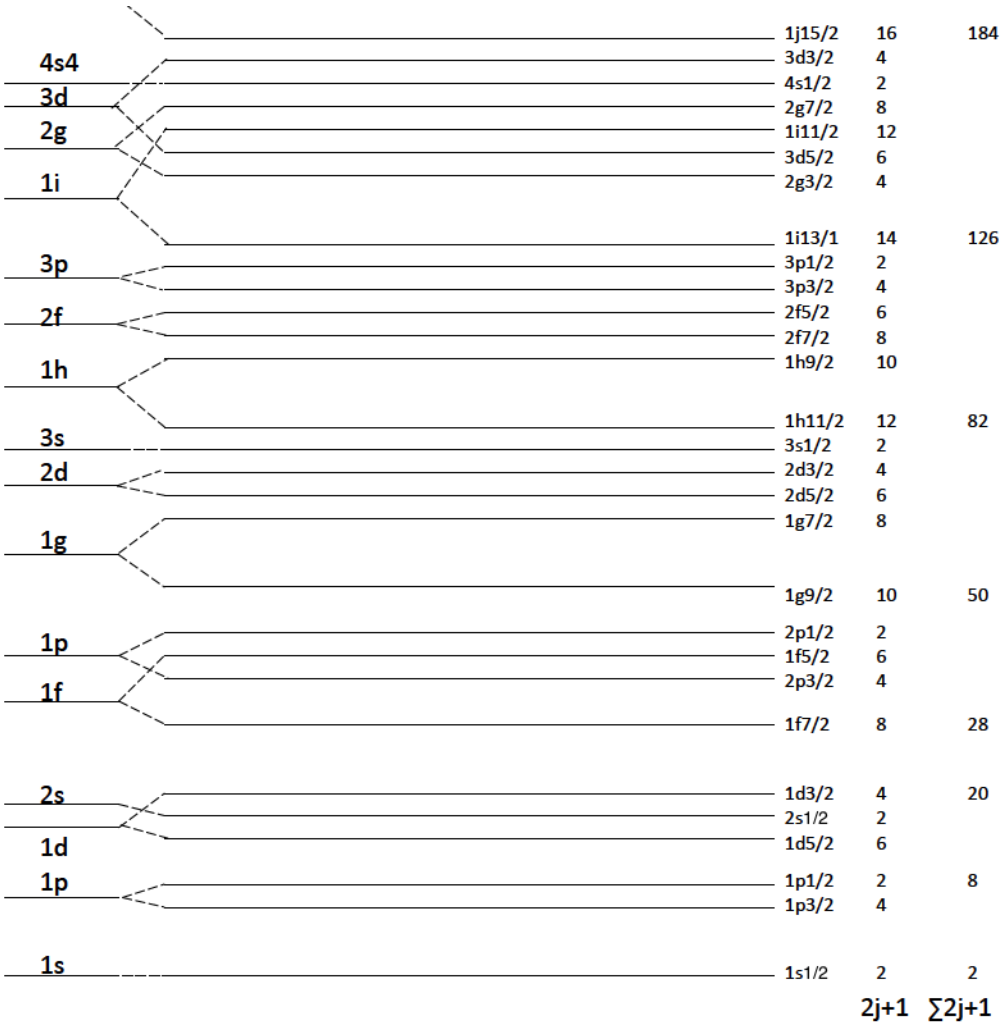

Fig. 2.1. Energy levels in a nucleus using nuclear potential with Woods-Saxon and spin-orbit terms.

momentum quantum number, m_j is magnetic quantum number that takes an integer values from $-j$ to $+j$, and j is total angular momentum, which take values $l+\frac{1}{2}$ or $l-\frac{1}{2}$. The degeneracy of each level is given as $2(2j+1)$. The shell model was a huge success; for the first time an explanation for particular stability at so called "magic number" was found. The model successfully reproduced experimentally measured excitation energies, spin/parities for the ground state and low-energy excited states. Although the success of this single particle model was tremendous, it suffered many shortcomings. For example, it was not able to explain the magnetic moment of the nuclide $^{17}_{9}$F which is $4.72\mu_N$ whereas value predicated from above model is -0.26μ_N. New phenomena such as disappearance of magic number at N= 8 and 20 for drip-line nuclei and emergence of new shells at nucleon

number = 14, 16, 32, were also not explained by the conventional shell model [24, 25]. Since, the shell model does not account for collective motion of nucleons, it was also not able to explain the rotational and vibrational levels in deformed nuclei. As discussed above, the shell model uses an approximate potential and hence is not able to explain many important features of nuclei mentioned above, it is necessary to examine the nuclear interaction within nuclei at a fundamental level.

2.3 Meson exchange theory

The nuclear force as an exchange force has a long history summarized in table 2.1. The first attempt to provide a microscopic description of the nuclear force was made by a Japanese physicist named Yukawa in 1935 [26]. Yukawa employed the idea from the theory of electromagnetic force (a long-range interaction) in which the force is manifested via the exchange of a massless photon. He hypothesized that the nuclear force between the two nucleons is mediated via the exchange of a massive particle, now known as π meson. Since the uncertainty principle allows the massive virtual particle to move a short finite distance, the nuclear force acts as a short range force. This particle was later discovered in cosmic rays (1947) and also in the Lawrence Berkeley National Laboratory (1948). Yukawa derived the following form of the nuclear potential known as the Yukawa potential

$$V(r) = \frac{-g^2 e^{-m_\pi r}}{r} \tag{2.3}$$

where g is a coupling constant and m is the mass of the mediator (~ 135 MeV/c^2) pion. The coupling constant can be determined by phase-shift analysis using the experimental data. The massive nature of the mediator makes the nuclear force a short range force. On adding spin and isospin effects, a more accurate one-pion

exchange potential (OPEP) can be written as

$$V(r) = \frac{f^2}{4\pi}\frac{m_\pi}{3}(\tau_1.\tau_2)\left\{\sigma_1.\sigma_2 + S_{12}\left[1 + \frac{3}{m_\pi r} + \frac{3}{m_\pi r^2}\right]\right\}\frac{e^{-m_\pi r}}{m_\pi r}, \tag{2.4}$$

where f^2 is a coupling constant, τ and σ are the isospin and spin of the nucleons, respectively. The term $S_{12} = 3(\sigma_1.\hat{r})(\sigma_2.\hat{r}) - \sigma_1.\sigma_2$ represents the tensor operator, where σ_i are the Pauli matrices.

Table 2.1. History of Nuclear Force. *Source*: Adapted from Ref. [1].

Year	Theory
1935	**Meson theory by Yukawa**
1950's	The "Pion Theories"
	One-pion exchange: good; Multi-pion exchange: failure.
1960's	Many pions $\equiv$ multi-pion resonances: σ, ρ, ω ,...
	The One-boson exchange Model: success.
1970's	Two-pions exchange models:
	Paris, Bonn, Stony Brook, Partovi-Lomon.
1980's	Discovered **QCD**: Quark Models
1990's	High-precision NN potentials:
	Nijmegen I, II, '93, Reid93, Argonne V18 and CD-Bonn.
	Advances in **effective field theory**: Weinberg, van Kolck...
3rd millennium	Effective Field theory: **Back to Meson (Pion) theory!**
	But, *Constrained by Chiral Symmetry.*

In 1951 a more detailed picture of the nuclear potential was initiated by the Japanese physicists Taketani, Nakamura and Sasaki [27, 28]. They proposed to divide the range of the nuclear potential into three interaction regions: long-range part, intermediate-range part, and hard-core part. The long-range part ($r > 2$ fm) is governed by exchange of one-pion. In intermediate-range, interaction is governed by exchange of two-pions and heavier mesons. Finally in the hard-core region ($r < 1$ fm) processes like multi-pion, heavier mesons play their role. The pion exchange diagram which contribute to the one-pion exchange potential (OPEP) and the two-pion exchange potential (TPEP) are shown in figure 2.2.

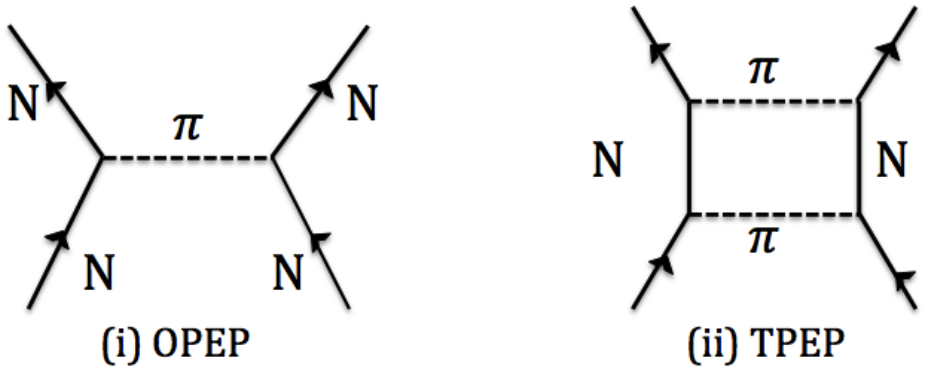

Fig. 2.2. Nuclear force as exchange of pions between nucleons. (i) The one-pion exchange diagram. (ii) The two-pion exchange diagram [29].

Although the one-pion exchange got well popularized for the long-range region during 1950's, a serious problem occurred when two-pion exchange contributions were included. It was not able to give short-ranged spin-orbit force [30]. For that reason, in 1960 it was suggested that multi-pion exchange can be well accounted by including the exchange of multi-pion resonances which lead to the one-boson-exchange (OBE) models [31–33]. The weak point of OBE model was the contribution from the scalar-isoscalar σ or ϵ boson, for which empirical evidence remains controversial and search for realistic 2π-exchange calculations was taken up again.

In 70's and 80's various nucleon-nucleon (NN) potentials were constructed based on meson-exchange theory. These were the Bonn [34], Nijmegen [35], Argonne [36] and Paris [37–39] potentials. Around 1990, the Nijmegen group, using phase-shift analysis developed high-quality potentials namely, Nijmegen-I, Nijmegen-II and Reid93 [40]. Consequently, the Bonn and Argonne groups also refined their potentials which are now known as Charge Dependent CD-Bonn potential [41] and Argonne-V18(AV18) [42] potentials. All the NN potential models describe the long-range part using one-pion exchange whereas for short and intermediate-range treatment varies from two-pion exchange potential to purely phenomenological potentials. For example, the AV18 potential contains three terms: the electromagnetic interactions term, the OPEP, the TPEP and a phe-

nomenological term for the short-range interaction:

$$V_{NN} = V_{NN}^{\gamma} + V_{NN}^{\pi} + V_{NN}^{R} \tag{2.5}$$

where V_{NN}^{γ} represents the electromagnetic term, which include the contributions from one- and two-photon exchange, vacuum polarization diagram with appropriate electric and magnetic form factors of protons and neutrons. The quantity V_{NN}^{π} is the OPEP (equation 2.4). The term V_{NN}^{R} includes the TPEP of the form $\frac{e^{-2m_\pi r}}{r^2}$ to account for the attractive nature of the nuclear force at intermediate-length scale, and the Woods-Saxon potential (equation 2.1) to represent the repulsive hard-core effect. In addition to these, a cut-off function is used in V_{NN}^{π} and V_{NN}^{R} so that the contribution from the OPEP and TPEP becomes zero at $r = 0$. The NN potential models also rely on the fitting to the NN scattering data with the χ^2 per degree of freedom near one which requires them to have a large number of parameters. The AV18 potential has 40 adjustable parameters and other NN potentials also have a similar number of parameters.

To see how efficiently these models describe the properties of nuclei, let us consider the simplest of all nuclei, the deuteron. The deuteron is a two nucleon system (one proton and one neutron), and its properties have been tabulated in table 2.2. We can observe that the phenomenological NN potential model predictions agree with the experimental values.

Table 2.2. Properties of the deuteron in its ground state using phenomenological NN potential models [43].

Observable	Experiment	AV18	Nijm II	Reid 93	CD Bonn
Matter radius r_d (fm)	1.971(5)	1.967	1.9675	1.9686	1.966
Magnetic moment (μ_N)	0.857406(1)	0.847			
Quadrupole moment (e-fm^2)	0.2859(3)	0.270	0.271	0.270	0.270
D/S state ratio	0.0256(4)	0.0250	0.0252	0.0251	0.0255

The two-nucleon potentials were able to accurately describe the properties of the two nucleon system, but when applied to study the triton (a three-nucleon

system), they failed to reproduce its experimental binding energy (see table 2.3). The NN potential models also underestimated the binding energies of ^{3}He and ^{4}He by about 1 and 4 MeV in the case of the three- or four-nucleon system, respectively. A similar underbinding was found for other nuclei as well [44]. The inability of the NN potential model to explain the binding energies of three or more than three-nucleon systems lies in the fact that nucleons were treated as point-like particles disregarding their internal quark structure. The three-nucleon force (3NF) emerges as a residual tidal force due to the excited states of the nucleon.

Table 2.3. Ground state triton's binding energy using phenomenological NN potential models [45].

Experiment (MeV)	AV18 (MeV)	Nijm II (MeV)	Reid 93 (MeV)
8.48	7.62	7.62	7.63

The first attempt to show the existence of the many-body forces among nucleons was made by Holstein and Primakoff in 1938 [46]. However, no definite estimate to find the three-nucleon force was made until 1956 due to the work of Fujita and Miyazawa [47]. They proposed that the 3NF among three-nucleons can be visualized as an exchange of two pions between three nucleons with the excitation of the nucleon at the centre to an isobar Δ (the first excited state of the nucleon, with spin 3/2 and mass 1232 MeV) as shown in figure 2.3(i). This interaction is attractive in nature, and provides more binding energy to the three-body system. There are other processes shown in figure 2.3(ii-iv) that contribute to the three-nucleon potential. So far various three-nucleon potentials have been developed, viz. Urbana [10], Illinois [6], Tucson-Melbourne (TM) [8, 9], and the Brazil models [48]. The Urbana potential include the contribution from the two-pion exchange diagram (Fujita-Miyazawa) as shown in figure 2.3(i) and a short-range phenomenological term. The three-nucleon Urbana potential in addition to the two nucleon potential (AV18), was found to improve the estimated binding energy but it still underbinds for most of the nuclei. This problem led to the investigation of other possible processes that can contribute to the three nucleon potential.

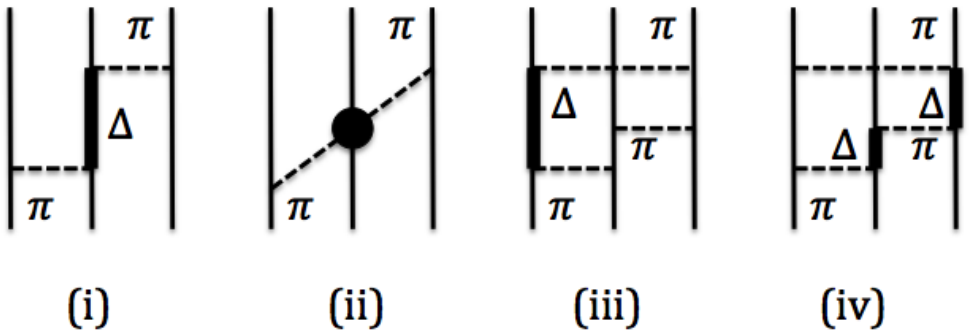

Fig. 2.3. A few examples of the three-nucleon force. (i) The Fujita-Miyazawa 3NF involves the excitation of one of the nucleon to a Δ particle accompanied by exchange of two pions. (ii) The two-pion exchange through S-wave excitation. (iii) The three-pion exchange with one Δ excitation state. (iv) The three-pion exchange with two Δ excitation states [29].

In 2001, the Illinois model was proposed, which included the contribution from processes shown in figure 2.3. The Illinois potential can be written as

$$V_{ijk} = V_{ijk}^{2\pi,Pwave} + V_{ijk}^{2\pi,Swave} + V_{ijk}^{3\pi} + V_{ijk}^{R} \tag{2.6}$$

where $V_{ijk}^{2\pi,Pwave}$ and $V_{ijk}^{2\pi,Swave}$ include the contribution from P-wave and S-wave two-pion exchange diagrams, respectively (figure 2.3 (i,ii)), whereas the $V_{ijk}^{3\pi}$ term represents the three-pion exchange diagram shown in figure 2.3 (iii,iv).

Table 2.4. Binding energies of light nuclei in MeV using NN (AV18) and using NN+3N potential. Inclusion of 3N potential provides a comparable result [6].

Potential	^{3}H	^{4}He	^{6}He	^{7}Li	^{8}Be
AV18	7.61(1)	24.07(4)	23.9(1)	31.6(1)	45.6(3)
AV18+UIX	8.46(1)	28.33(2)	28.1(1)	37.8(1)	54.4(2)
AV18+IL2	8.43(1)	28.37(3)	29.4(1)	39.6(2)	56.6(4)
Experiment	8.48	28.3	29.27	39.24	56.50

We review the results for quantitative interest in table 2.4. We can infer from the table that calculations using NN potential alone underestimate the binding energies of light nuclei. On inclusion of the three-nucleon potential, the estimates improve. Besides the 2NFs and 3NFs, there are also four-nucleon forces (4NFs), and other many-body forces. However, the 2NF is much stronger than the 3NF,

which in turn is much stronger than the 4NF, and so on. The phenomenological NN+3N potentials have been successfully applied to study the properties of light nuclei and are still popular and frequently used. Despite their tremendous success, due to the discovery of quantum chromodynamics in 1980's, the meson exchange formulation had to be viewed as a model for the nuclear force and hence the search for deriving the nuclear force from the underlying fundamental theory of QCD started again. The formulation of QCD provided a more detailed picture of nucleons. For instance, a proton is made up of two up quarks and one down quark whereas a neutron is made up of one up quark and two down quarks. Since QCD shows the non-perturbative nature at the low energy regime relevant to nuclear physics, it is extremely challenging to provide a converging solution to a nuclear N-body problem.

2.4 Chiral perturbation theory

The nuclear force can be derived from the theory of the strong interaction if the concept of EFT is applied to low-energy QCD [49–55]. The emergent theory is now known as chiral perturbation theory (χPT). Using the EFT, the Lagrangian is written as a function of relevant degrees of freedom (nucleons and pions) with terms consistent with the broken chiral symmetry of QCD and general symmetries. Massless particles follow the chiral symmetry, i.e. the spin and the projection of momentum in the direction of spin is always parallel or anti-parallel and does not change. Since quarks are almost massless, an approximate chiral symmetry is employed in the construction of the Lagrangian. When one uses this Lagrangian to calculate the nuclear potential, it generates an unlimited number of interaction diagrams, which seems cumbersome to handle. However, Weinberg in 1990 [53] showed a systematic way of expansion in terms of $(Q/\lambda_\chi)^\nu$, where Q denotes a pion mass/momentum, $\nu \geq 0$ is a power, and $\lambda_\chi \approx 1$ GeV is the chiral symmetry breaking scale. In the expansion, for a given order ν the number of contributing terms are finite and can be calculated. These terms are uniquely defined and the

prediction at each order is model independent. By adding higher order terms, the amplitude can be refined to a desired accuracy. This scheme is called χPT.

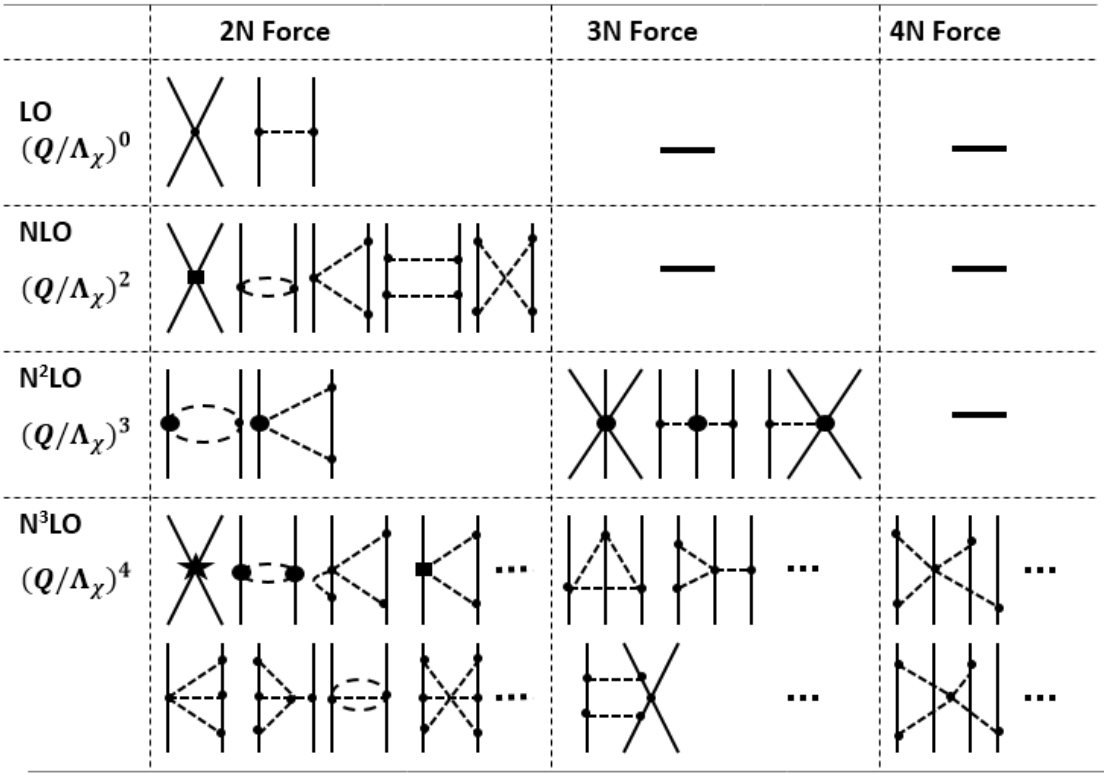

Fig. 2.4. The nuclear potential derived from chiral perturbation theory. The solid lines and dashed lines represent the nucleon and the pion, respectively. To differentiate the different vertex factors involved in interaction diagrams, small dot, large dot, solid square and solid star have been used. Terms at leading order, next-to-leading order, next-to-next-to-leading order, and next-to-next-to-next-to-leading order are represented by LO, NLO, N^{2}LO, and N^{3}LO, respectively [1].

The Feynman diagrams for the nuclear potential are shown in figure 2.4. The first diagram that contributes to the NN potential appears at the order of $\nu = 0$ whereas for the three-nucleon force it appears at the order of $\nu = 3$ which explains why 3NFs are weak as compared to 2NFs. One can note that OPEP, TPEP and the Fujita-Miyazawa interaction diagrams (see figures 2.2 and 2.3) based on meson-exchange model also appear here. χPT is a promising theory of the nuclear force at present. In the last decade, the chiral 2NFs have been used extensively to study the nuclear structure and reactions of nuclei [56–63]. The chiral 2NF and 3NF together have also been used successfully for predicting the structure of light- and medium-mass nuclei [14, 64–72].

2.5 Towards *ab initio* theory

The central goal of nuclear physics is to establish a unified fundamental theory that can be used to explain nuclei structure and nuclear reactions. Over the past decade a significant amount of progress has been made through techniques such as Green's Function Monte Carlo [5, 7, 44, 73], no-core shell model [74, 75], no-core shell model/resonating group method [76–78], no-core shell model with continuum [13, 15, 79], coupled-cluster method (CCM) [62, 72] and nuclear lattice effective field theory [80] in attempt to achieve the goal; such approaches are categorized as *ab initio* theory of nuclear physics. In the *ab initio* technique we aim to solve an A-body Schrödinger equation by constructing the Hamiltonian with two-, or possibly more, nucleon interaction terms. The real problem in solving the A-body Schrödinger equation is how to accommodate the possible interactions in a sensible and tractable manner. Each model employs a different technique and has its own features. For instance, the GFMC method uses a Variational Monte Carlo technique (VMC) to obtain the trial wavefunction as input parameter and propagate through the Hamiltonian with a realistic potential.

The approach closest to a traditional shell model is the no-core shell model in which one treats each nucleon as active and interacting through realistic inter-nucleon (NN or NN+3N) forces. The Hamiltonian for the A-nucleon system is written as [81]:

$$H_A = T_{rel} + V = \frac{1}{A}\sum_{i<j}^{A}\frac{(\vec{p_i}-\vec{p_j})^2}{2m} + \sum_{i<j-1}^{A} V^{NN}(\vec{r_i}-\vec{r_j}) + \sum_{i<j<k}^{A} V_{ijk}^{NNN} + ... \quad (2.7)$$

where m is the nucleon mass, $V^{NN}(\vec{r_i}-\vec{r_j})$ is the NN-interaction potential including both strong and electromagnetic components, V_{ijk}^{NNN} is the three-nucleon interaction, T_{rel} is the kinetic energy of A-nucleon system, and $\vec{p_i}$ is momentum of i^{th} nucleon. Calculations are performed using a harmonic oscillator (HO) basis. At present the no-core shell model has been successfully used for determining the

bound state properties of light nuclei ($A \leq 20$) [11–13]. Using the NN+3N interaction, the NCSM is able to calculate ^{3}H, ^{3}He, ^{4}He ground state energies that are in good agreement with measurement. The ground state of ^{6}Li has a very small quadrupole moment, Q = -0.0818(17) e fm^2 [82]. It has been a challenge for nuclear models to explain its quadrupole moment value. Various techniques have been used to attempt to explain this observable [82] and did not succeed. However, when the NCSM model with the chiral N^{3}LO NN potential was applied, its predicted value of Q = -0.08(2) $e$fm^2 was found to be in excellent agreement with experiment. Similar agreement was found when chiral 3NF was also included in the NCSM calculation [83]. The NCSM calculations using the CD-Bonn NN potential have been used extensively to predict the energy levels of light nuclei for instance, as in ^{7}Li. The energy levels for lowest 9 states of ^{7}Li are in correct order shown in figure 2.5. What is remarkable is that when it is applied to nuclei around mass number A=10, and ^{10}B in particular, it seems to be highly sensitive to the detail of the nuclear interactions among the nucleons. For ^{10}B, the NCSM model with the CD-Bonn NN potential predicts the ground state spin to be $J = 1^+$ which is in disagreement with the value of $J = 3^+$ from experiment (figure 2.5). Similar disagreement has been found using other NN potentials such as: the AV8' [84] and the chiral N^{3}LO NN potential [14, 85]. The GFMC model calculation with the AV18 (and V8') potential also report a similar result [5]. This ambiguity is resolved when the 3N interaction, such as the TM' is included. Similarly, the inclusion of the chiral N^{3}LO NN with the chiral N^{2}LO 3N interaction results in a correct description of ^{10}B energy levels [14]. I should point out here that the AV18 NN potential with Urbana IX 3N potential does not produce the correct ground state spin of $J = 3^+$ [5]. This fact shows that the fine details of the 3N potential significantly to improve the theoretical prediction especially for the nuclei with mass number $A = 10$.

The scope of the NCSM model is restricted in a sense that it is applicable to study only the bound states of nuclei. To study the nuclear reactions and

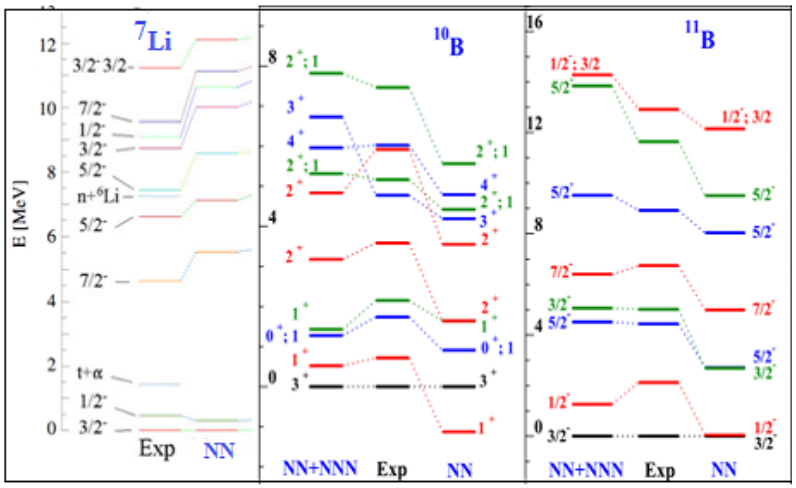

(a)

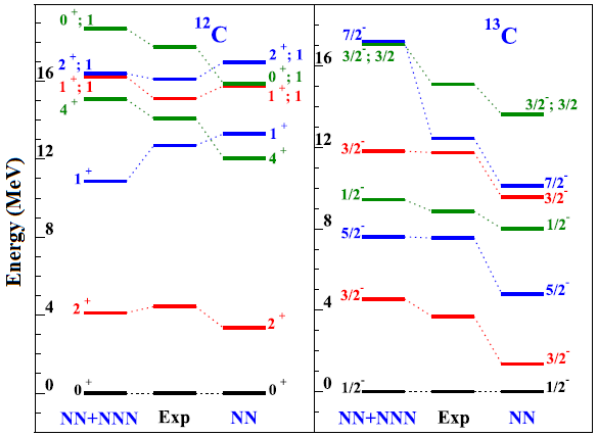

(b)

Fig. 2.5. NCSM calculations for light nuclei. (a) Energy levels in ^{7}Li using CD-Bonn potential (NN) [86]. Energy levels in ^{10}B and ^{11}B based on NN and NN+NNN potentials [14]. (b) Energy levels in ^{12}C and ^{13}C based on NN and NN+NNN potentials [14]. The excitation energies are in MeV. Note, the ordering of energy levels in the ^{10}B depends on the three-nucleon (3N) interaction.

scattering process, Navratil *et al.* [16, 78] have developed a method named no-core shell model/resonating group method (NCSM/RGM). It supplements the NCSM technique with a microscopic cluster technique (RGM) which assumes that nuclei can be grouped in clusters. The NCSM/RGM has been successfully applied to scattering reactions such as $^{3}\mathrm{H}(d,n)^{4}\mathrm{He}$, $^{3}\mathrm{He}(d,p)^{4}\mathrm{He}$, $^{4}\mathrm{He}(p,p)^{4}\mathrm{He}$, $^{4}\mathrm{He}(d,d)^{4}\mathrm{He}$, and $^{7}\mathrm{Be}(p,\gamma)^{8}\mathrm{B}$ [11].

Recently due to the efforts by Navratil *et al.* [15], the *ab initio* NCSM and NCSM/RGM approaches have been merged into a single unified model *ab initio* no-core shell model with continumm (NCSMC), capable of calculating both the

bound states and the scattering states in a nuclear system. In NCSMC, the set of A-nucleon system is studied by including both A-body NCSM basis and binary cluster ($(A-a)$-body and a-body systems) continuous basis. Thus, the many-body wave function can be written as [15]:

$$\left|\psi_A^{J^\pi T}\right\rangle = \sum_\lambda c_\lambda \left|A\lambda J^\pi T\right\rangle + \sum_\nu \int dr r^2 \frac{\gamma_\nu(r)}{r} \hat{\mathcal{A}}_\nu \left|\phi_{\nu r}^{J^\pi T}\right\rangle . \tag{2.8}$$

where $|A\lambda J^\pi T\rangle$ is an eigenstate with eigenvalue E_λ of A-body NCSM Hamiltonian H_A^{NCSM}, and $\left|\phi_{\nu r}^{J^\pi T}\right\rangle$ are the binary-cluster $(A-a, a)$ states, $\hat{\mathcal{A}}_\nu$ is an operator to take care of exchange of nucleons belonging to different clusters, and $\gamma_\nu(r)$ is the wave function of the relative motion. In equation 2.8, the first term represents the NCSM basis states, which accommodates the short- and medium-range structure of A-body system, where as the second term represents the NCSM/RGM cluster states to include the scattering physics of the system. One of the attractive features of this model is that its convergence properties are superior to either the NCSM or the NCSM/RGM models. This newly developed model has been applied to study the resonances of ^{7}He (an unbound nucleus) using a chiral NN+3N potential, thereby settling the controversy of $J = 1/2^-$ resonance above the ^{6}He + n threshold [79]. This could not be realized within the *ab initio* bound-state approaches such as the Green's function Monte Carlo method or the no-core shell model. The NCSMC model appears to be a unified realistic *ab initio* technique to study properties of nuclei and nuclear reactions. The NCSMC model has also been successfully applied to study the $d-^4$He, $n-^4$He, and $p-^4$He scattering using a chiral NN+3N interaction [16, 17].

As described above, there have been various studies on the effects of the nuclear forces on the energy levels and the static properties such as nuclear moments in the nuclei. However, investigation of the effect of the three-nucleon force on the reaction observables is very limited. In fact, so far there is no such study on the neutron or proton-rich rare isotopes.

In this thesis we report the first investigation of the effects of the three-nucleon

force on the differential cross section of $^{10}C + p$ elastic scattering. The newly developed *ab initio* reaction theory [87] with the framework of the NCSMC has been to used to calculate the angular distribution of $^{10}C + p$ scattering reaction. The predictions for the differential cross sections using NN only and NN+3N forces are found to show substantial differences as will be discussed in Chapter 5.

Chapter 3

Experiment and Methodology

In this chapter we will discuss the experimental facility used to perform the experiment.

3.1 Radioactive Ion Beam production at TRIUMF

The understanding of nuclear phenomena has been greatly enhanced since the advent of the radioactive ion beams (RIB). The production of such radioactive ion beams requires an experimental facility equipped with a primary production beam, a target or ion-source, a mass separator, and a beam transport system. For our experiment the ^{10}C RIB was produced at TRIUMF, one of the world's largest particle and nuclear physics experimental facilities, located in Vancouver, Canada. At TRIUMF, RIBs are produced using a method called the isotope separation on-line (ISOL) method. The ISOL technique requires a primary beam, a target/ion-source, a mass separator, and a beam transport system. TRIUMF also houses a 500 MeV cyclotron (the world's largest cyclotron), which is used to produce the primary proton beams. The primary proton beam interacts with a NiO target producing rare isotopes, which then effuse into an ion source. A mass separator is used for selecting the ^{10}C beam. The ^{10}C beam is then reaccelerated using superconducting linear accelerator to $6A$ MeV, and then used for reaction studies at the IRIS spectroscopy facility.

3.2 IRIS

The **I**SAC Cha**r**ged Part**i**cle **S**pectroscopy station (IRIS) is a facility stationed in the ISAC-II experimental area at TRIUMF. The scientific purpose of the facility is to study the transfer reactions, elastic and inelastic scattering of neutron- and proton-rich nuclei. The reactions studied with IRIS involve the isotopes of hydrogen (e.g. p, d) as the target. The energy and scattering angle of the target-like particles emitted after the reaction are measured to obtain the excitation spectrum of ^{10}C. To reduce background from other reactions the heavy particles are also detected. The detectors and target involved are placed inside the vacuum chamber to avoid energy losses in air.

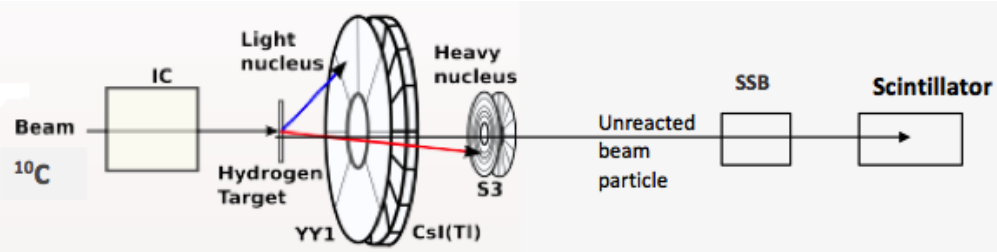

Fig. 3.1. IRIS setup.

A schematic view of the experimental setup is shown in figure 3.1. The IRIS facility consists of four major components:

- Ionization Chamber (IC)
- Solid H_2 Target
- Detectors for reaction products
- Scintillator and SSB detectors

These components will be discussed in the following subsections.

3.2.1 Ionization Chamber

The IRIS facility uses a low-pressure ionization chamber (with $\sim$ 5-20 Torr, isobutane gas) placed inside a vacuum box. It is placed upstream of the target and

hence enables us to identify the elements present in the incoming beam by identifying its atomic number (Z) through energy loss in the ionization chamber. The beam enters and exits the ionization chamber through the mylar windows that are typically $\sim 0.9\,\mu$m thick. We have shown the schematic design of the IC in figure 3.2.

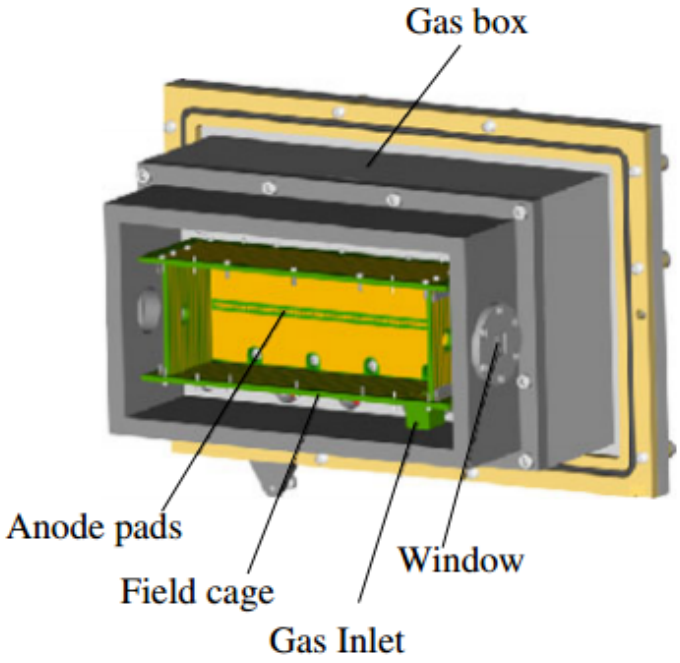

Fig. 3.2. Design of the IRIS Ionization Chamber.

The anode has been segmented into 16 sections and is used for the charge collection. The electrical signal produced in the anode is read out using the preamplifiers located outside the vacuum chamber. The anodes can be coupled together as well. For the ^{10}C(p,p)^{10}C experiment, the anodes were coupled to be equivalent to a single anode read out. The next component in the IRIS facility is a scattering chamber which houses the target and the detectors.

3.2.2 Solid H_2 Target

The novel feature of IRIS is the development of a thin windowless solid hydrogen target (SHT) which has been used for studying the desired reaction. Since we are working with an RIB of weak intensity, the use of SHT as a target is paramount

and greatly desired rather than utilizing the other conventional targets such as a liquid or gas H_2 target, or polyethylene target. The SHT enhances the scope of attaining a higher luminosity of scattered particles, thereby making the reaction study possible even with a weak beam intensity of $\sim$ 2500 pps for ^{10}C (a drip-line nucleus). The target assembly is depicted in figure 3.3. On the copper cell, a hole of 5 mm was bored at its centre, and its surface is affixed by a silver foil of $\sim$ 5 µm thickness. A cryocooler with a helium compressor is used to cool the target cell to a temperature of $\sim$ 4 K. We use a diffuser that sprays the H_2 gas on the surface of the silver foil used as a backing material to form the SHT target. The diffuser is retracted down after the formation of the SHT. The incoming beam of ^{10}C passes through the hole on the copper cell, and then through silver foil, and finally interacting with the SHT to produce scattered particles. Since the SHT is windowless at the exit channel, the scattered target-like particles only have to pass through the remaining part of the SHT, and hence do not undergo any significant energy straggling[1] and multiple scattering. This feature suppresses the broadening of the scattering angle and energy of the scattered protons, and hence improves the energy and angular resolution. Since SHT involves Ag-foil, we could get the background protons from fusion evaporation reaction of beam particles with Ag, but these background protons are far less in comparison to the case with the liquid hydrogen (produces background events from window material) or polyethylene targets $(CH_2)_n$ (background events originate due to the scattering from carbon nuclei in the target). The target cell is surrounded by a copper heat shield; it restricts the evaporation rate of solid H_2 due to the radiative heating from the ambient temperature and keeps the target temperature stable during the experiment. The heat shield has a vertical opening angle of $\pm 40^\circ$ and horizontal opening angle $\pm 60^\circ$ which allows the reaction products to reach the detectors.

[1]Phenomenon of spread in energy loss by incident particles due to random set of collisions.

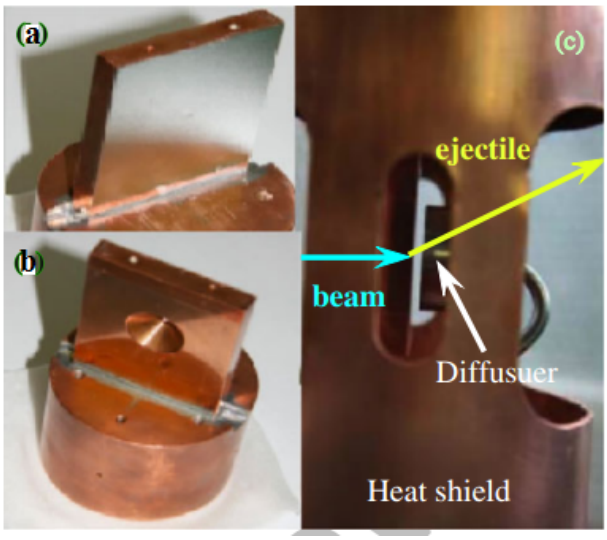

Fig. 3.3. Solid H_2 target assembly. (a) Silver foil on copper cell. (b) View of copper cell. (c) Copper cell placed inside the cylindrical heat shield [88].

3.2.3 Charged particle detectors

One of the goals of IRIS facility is to detect the charged particle reaction products produced in the reactions with isotopes of hydrogen as target. Therefore, the detection system is designed in such a way that it enables us to detect both the light target-like products as well as the heavy beam-like reaction residues. IRIS uses two pairs of thin and thick detectors for different purposes. To measure the energy loss and the scattering angle for target-like (e.g. *p, d, t*) light nuclei, we use a thin silicon detector [89] ($\sim$ 100 µm) represented as YY1, placed downstream of the target (figure 3.4a). It is segmented in 8 azimuthal sectors, and each sector is segmented in 16 rings. Each of these 8x16 segments act as an independent detector. To measure the remaining energy of target-like particles that passed through the YY1 detector, we place a 12 mm thick CsI(Tl) detector behind the YY1 detector downstream of the target. The CsI(Tl) array consists of 16 crystals arranged in the same azimuthal fashion as the YY1 array (figure 3.4b). The YY1 and CsI(Tl) arrays are placed in such a fashion that they can detect target-like particles in coincidence and allow the beam-like particles to pass through the hole in these detectors.

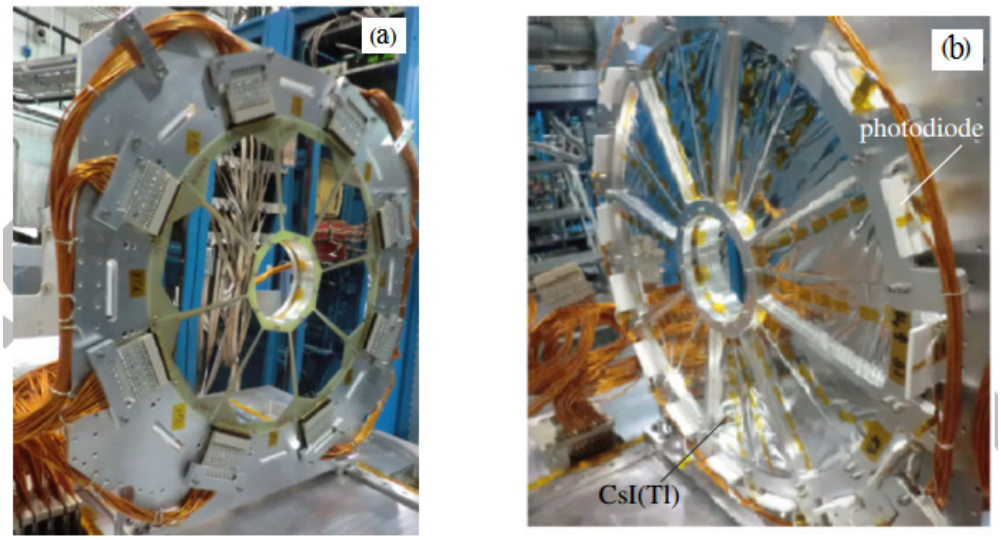

(a) (b)

Fig. 3.4. Detectors for target-like nuclei. (a) YY1 detector. (b) CsI(Tl) detector.

To detect the beam-like particles we require both a thin and a thick silicon S3 detector [89]. We represent the first as S3d1 and second as S3d2 (figure 3.5). The S3d1 detector is a thin ($\sim 60\,\mu m$) silicon detector used to measure energy loss and the scattering angle of the beam-like heavy particles. It is segmented in 24 rings on the one side where as the other side is segmented in 32 sectors. The S3d2 is a thick silicon ($\sim 500\,\mu m$) detector used to measure the remaining energy and scattering angle of beam-like heavy particles. The S3d2 detector is segmented in same way as the S3d1 detector. Both the S3d1 and the S3d2 are placed downstream of the target.

The energy and angle measurements of the reaction products allows us to reconstruct the missing mass spectrum, which is necessary for the identification of elastic reaction.

3.2.4 Scintillator and SSB detectors

The IRIS facility has a zero degree silicon surface barrier (SSB) detector, which is intermittently placed in the beamline to measure the remaining energy of unscattered beam particle after passing through the target. This is used to determine the thickness of silver foil in target cell. The facility also employs a scintillator placed

Fig. 3.5. S3d1 and S3d2 detector.

at zero degrees at the end of the beamline to count the number of beam particles. The ratio of the scintillator to ionization chamber counts helps in monitoring the overall beam transmission through the chamber during the entire experiment. These detectors are placed in the last separate vacuum chamber. The unreacted beam is eventually stopped and counted using a radiation hard inorganic scintillator (YAP:Ce) read out by a photomultiplier tube (PMT).

3.3 Signal Processing and Trigger Logic

In this section we provide a brief overview of schematics of electronics used in the data acquisition for the ^{10}C(p,p)^{10}C experiment. We know that when an incident charged particle interacts with the detector, it produces electric charge carriers (electron-ion pair in case of ionization chamber, and electron-hole pair in semiconductor detectors) which carry the information about the energy deposited in the detector by the particle. To construct an electrical signal for further analysis, the electric charges produced are collected by applying an electric field on the detector volume.

The initial elements in signal processing are the *preamplifier* and *shaping amplifier* shown in figure 3.6(a). The main purpose of the preamplifier is to extract

a voltage pulse from the detector while adding as little noise as possible. The preamplifiers are thus located close to the detectors, minimizing the length of the cable connecting them to the detector. The preamplifers used in the experiment were of charge-sensitive type. The output pulse from a preamplifiers is shown in figure 3.6(a). Once the energy signal passes through the preamplifier, it is sent into a shaping amplifier unit for further amplification and processing. The pulse is shaped in a manner that does not affect its maximum amplitude and reduce its pulse width drastically. In general, the shaping amplifier unit involves a capacitor-resistor (CR) network followed by few successive resistor-capacitor (RC) networks. The purpose of the CR network is to improve the signal-to-noise ratio (SNR) by blocking the low-frequency components which contain a lot of noise. On the other hand, the RC network attenuates the high-frequency components, which also contains a lot of noise, thereby enhancing the SNR. We have used model MSCF-16, a 16-channel shaper and timing amplifier with leading edge discriminator (LED) unit [90]. The MSCF-16 contains CR-RC^5 network which amplifies and transforms the preamplifier signal into a Gaussian pulse. The pulse pile-up (overlap between successive pulses) is greatly reduced on changing the preamplifier pulse waveform into the Gaussian waveform. The MSCF-16 unit also incorporates the baseline restorer that ensures that the baseline between pulses is at the ground potential. The purpose of the discriminator in the MSCF-16 unit is to respond only to the input signals with a pulse height greater than a specified threshold value. We set the threshold value to reject the pulses coming from the electronic noise. The discriminator (in the MSCF-16 unit) used in this experiment was a leading edge discriminator, whose purpose was to generate a trigger pulse at the moment the pulse crosses the threshold voltage level. The schematics of generating the shaped pulse and trigger signal (a logic signal which represents the presence and absence of an event in the detector) are shown in figure 3.6(b).

Since the amplitude of the voltage signal from shaping amplifier contains the information on the energy deposited in that detector, we need to translate the

analog voltage signal into something more useful: an equivalent digital signal. The amplified energy signal received from the shaper unit goes into the analog-to-digital converter (ADC). The purpose of the ADC is to convert the amplitude of an analog voltage signal into a proportional digital number. The ADCs (model number MADC32) employed in the experiment were of peak-sensing type. The ADCs have a resolution of 12 bits, thereby covering a range from 1 to 4096 channels. Since we were interested in analysing the scattered particles detected via the YY1/S3 detectors, we performed a Logic-OR operation on the trigger signals obtained from the MSCF-16 unit of the YY1/S3 detectors. The obtained Logic-OR signal is called "free trigger". We know that for the data acquisition system (DAQ), it takes a finite amount of time to process an event, hence, the DAQ can not store all the events occurred in the detectors. The free trigger is then fed into the Quad Gate generator unit (M794) to acquire the data in coincidence, which essentially generates a gate pulse with a user-defined time window (usually 2 µs). The generated gate signal is then fed into the ADCs which enabled the ADC to know when to start taking the data and for how long. We have shown the further electronics in detail, required to digitize the analog data and store it in the computer in figure 3.8. The electronic modules together with the data acquisition system provide the necessary signal processing.

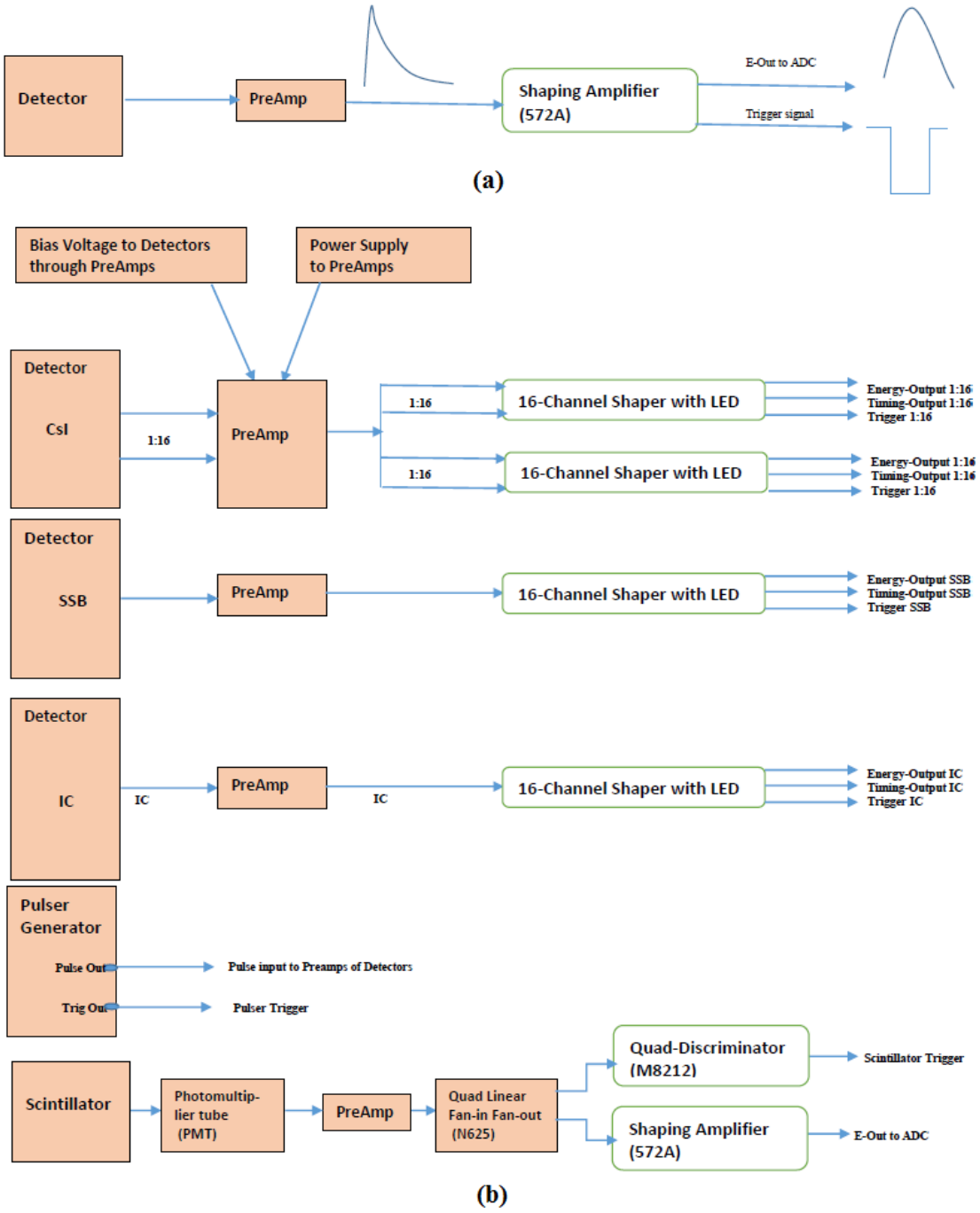

Fig. 3.6. Pulse processing. (a) Output from a preamplifier unit and a shaping amplifier for a general detector. (b) Output from the shaping amplifier for CsI(Tl), SSB, IC, Pulser, and scintillator.

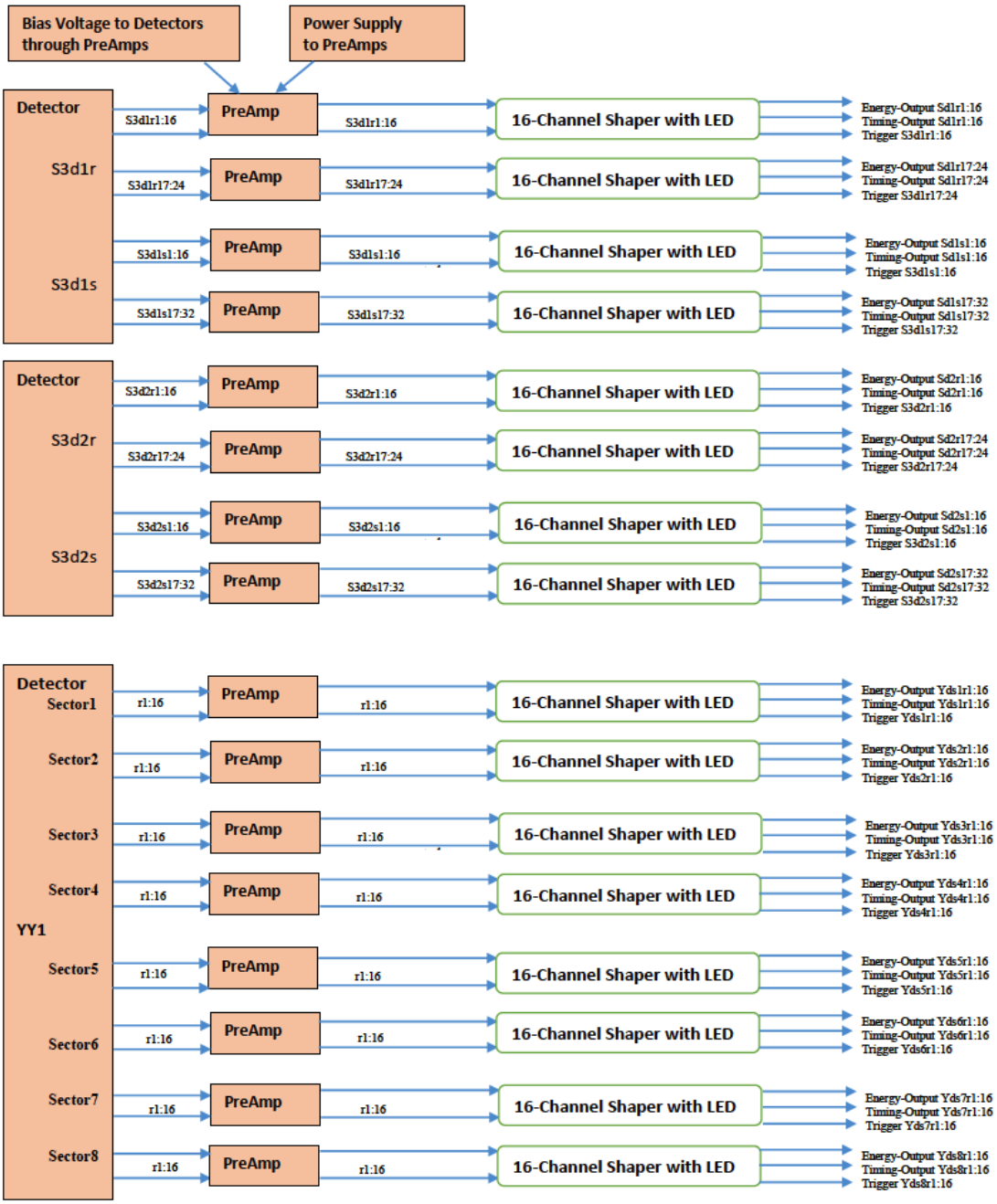

Fig. 3.7. Output from the shaping amplifier for S3d1, S3d2 and YY1 detector.

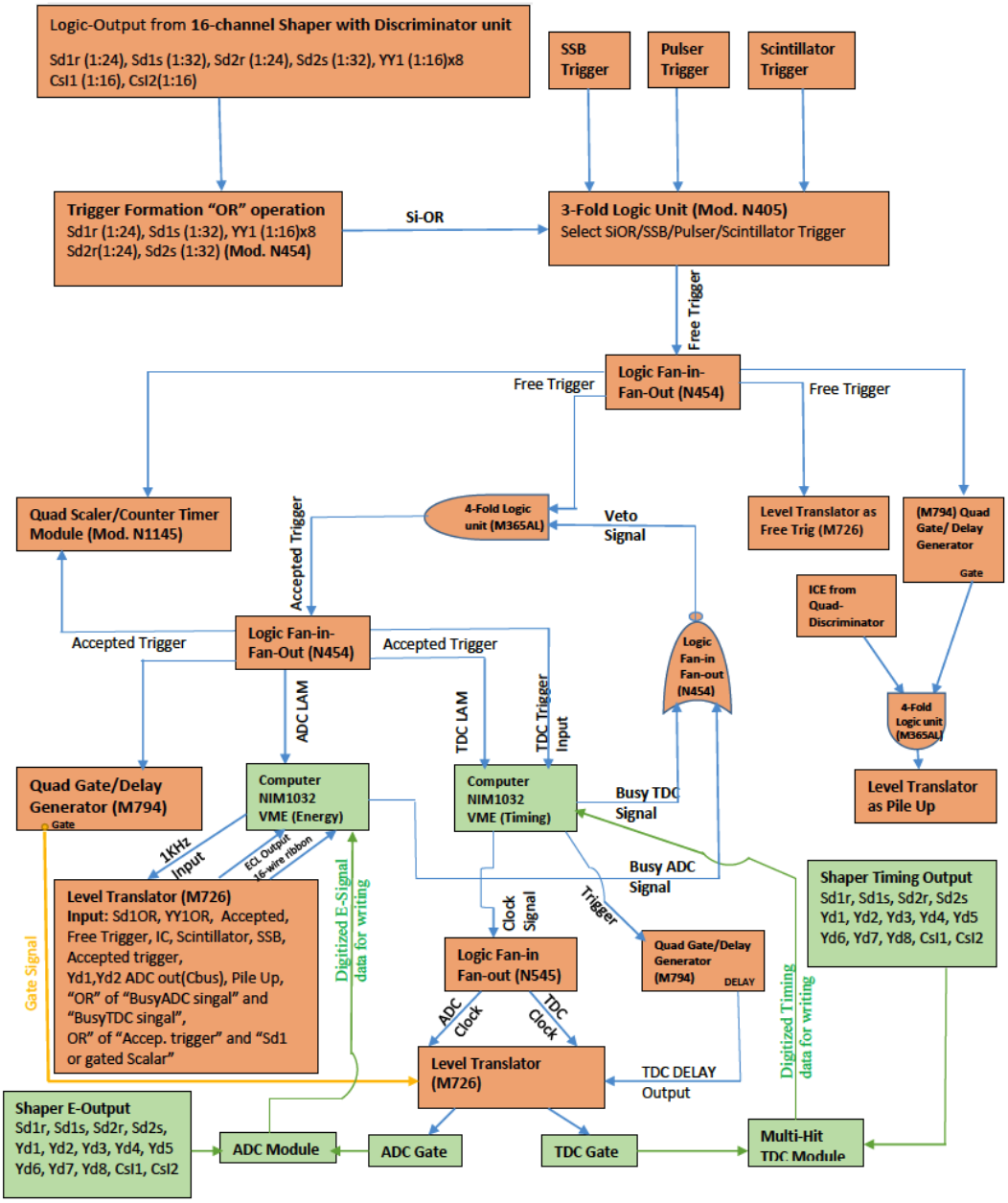

Fig. 3.8. Formation of trigger logic and analog to digital conversion to record the data.

Chapter 4

Analysis of elastic scattering ^{10}C(p,p)^{10}C

In this chapter the analysis of the data to extract the physics information will be described. To do that, the first step was to calibrate the detectors employed in the experiment. This essentially maps these digitized analog-to-digital converter (ADC) channels to a physical quantity, namely the energy. Next, we will discuss methods to identify the particles detected in the experiment. We will also show how the solid H_2 target thickness has been measured throughout the experiment. We will also discuss the missing mass spectrum technique which enables us to identify the ^{10}C(p,p)^{10}C elastic reaction channel. Finally, we will present the measurement of the differential cross section.

4.1 Identification of beam particles

The ionization chamber (IC) is placed upstream of the target to provide us with the information about the atomic number of the particles present in the beam. In the experiment, the beam contains ^{10}B particles as contamination. Two ADC spectra of the IC detector are shown. Figure 4.1a is for IC operated at 8 Torr pressure, and figure 4.1b is for the IC detector operated at 19.5 Torr. We can see that there are two peaks present in these spectra that correspond to ^{10}B and ^{10}C particles.

Since the ^{10}C particle has a higher atomic number than the ^{10}B particle, the energy loss for the ^{10}C is more than the ^{10}B particle. So the ^{10}C peak should

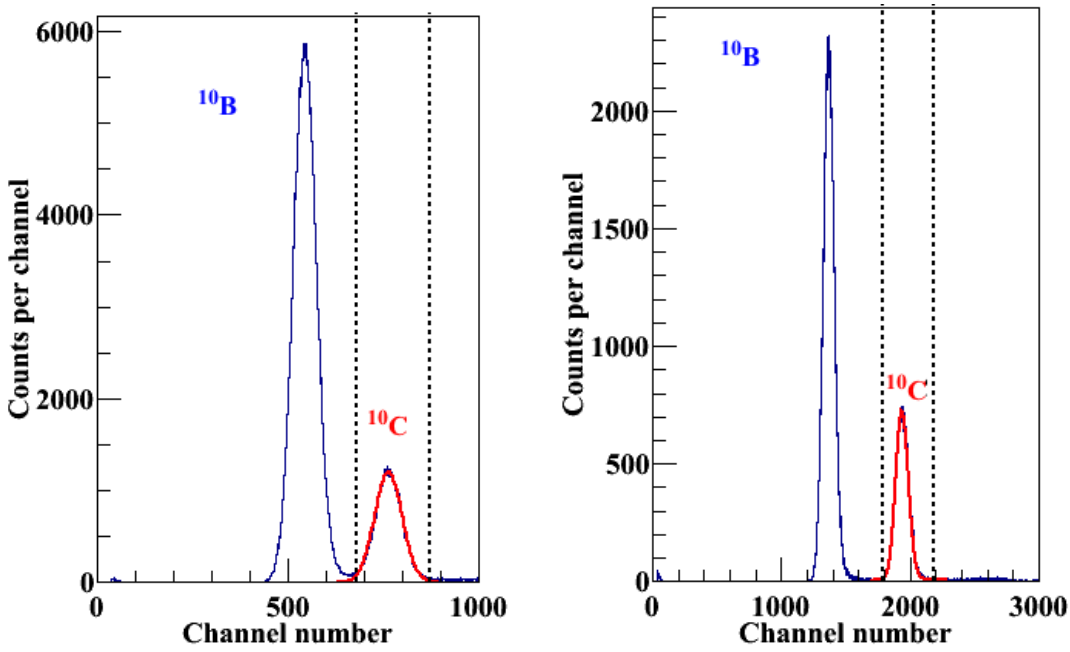

Fig. 4.1. ADC spectrum of IC. (a) For 8 Torr pressure. (b) For 19.5 Torr pressure.

appear at a higher channel number than the ^{10}B peak. It can be understood from the equation of the stopping power (dE/dx) of a charged particle passing through the matter, which is defined as energy loss per unit length given as:

$$-\frac{dE}{dx} \propto \frac{Z^2}{v^2} \tag{4.1}$$

where Z and v are atomic number and velocity of the charged particle, respectively. From these ADC spectra of the IC, we have selected the events corresponding to the ^{10}C peak. The selection of the region is shown by the vertical lines in figure 4.1 and has been used for further analysis of the ^{10}C(p,p)^{10}C reaction.

4.2 Detector Calibration

In this section we describe the energy calibration of the detectors that provides the basic foundation for the data analysis. We know that when a charged particle passes through a detector, it deposits a certain amount of energy and we get a voltage pulse from the detector which is digitized in the form of a channel number

using a peak sensing ADC. The meaning of the calibration is to convert the channel number into the energy deposited in the detector. We employ the following linear equation for the calibration of the detectors:

$$E = \text{gain} * (\text{ChannelNumber} - \text{Pedestal}) \tag{4.2}$$

where E is the energy deposited by an incident charged particle in the detector, "ChannelNumber" is the peak position of the incident particle in the ADC spectrum, "Pedestal" is a zero-energy point in the ADC spectrum, and gain is a channel to energy conversion factor for a particular ADC. The unit of gain is MeV/channel if E is in MeV. The equation 4.2 describes the linear relation between the ADC channel number and the physical quantity energy. Once we have found the gain and pedestal for a detector, the detector is said to be calibrated. In this section we will discuss the calibration of S3d1, S3d2, YY1 and CsI(Tl) charged particle detectors using the calibration equation 4.2. But, before we explain that, we need to determine the silver foil thickness, without which we will not be able to perform the required energy loss calculation.

4.2.1 Silver foil thickness determination

The thickness of silver foil, which is the backing of the solid H2 target, is one of the unknown quantities that needs to be determined. We have used the energy information from the silicon surface barrier (SSB) detector (in absence of H_2 target) to measure the thickness of silver foil.

We have shown the material layers which have been taken into account in the energy loss calculation of the beam particles (figure 4.2). As explained above the beam has the ^{10}C as well as the ^{10}B particles, which after passing through the IC and the silver foil, deposit their remaining energy into the SSB detector. The ^{10}C peak in the SSB ADC spectrum should appear at lower channel number than the ^{10}B peak since the former has lower energy at the exit end of the silver foil. For various thicknesses of the silver foil we performed the energy loss calculation and

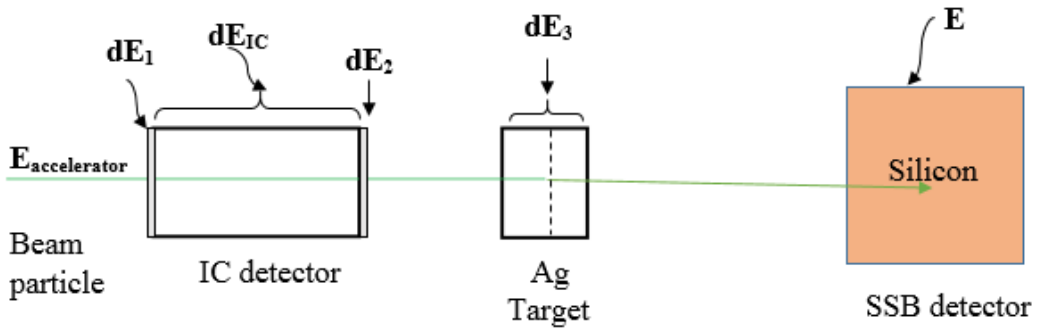

Fig. 4.2. Layout of material layers for the energy loss calculation in the SSB detector.

computed the gain g_1 and g_2 of SSB ADC given as

$$g_1 = \frac{E_C}{Peak_C - Pedestal} \tag{4.3}$$

$$g_2 = \frac{E_B}{Peak_B - Pedestal} \tag{4.4}$$

where E_C and E_B are energies deposited by the ^{10}C and the ^{10}B particles in the SSB detector after passing through the silver foil, respectively; $Peak_C$ and $Peak_B$ are the respective peak positions of the ^{10}C and the ^{10}B particles in the ADC spectrum of the SSB detector. *Pedestal* is a zero-point of the SSB ADC. The gain should be independent of the particle type and is a fixed quantity for a specific amplifier setting of that ADC. Therefore, for the actual thickness of the silver foil the gain g_1 and g_2 would be same.

We choose the silver foil thickness for which the ratio $\left|\frac{g_1-g_2}{g_1}\right|$ was minimal (figure 4.4). We found the thickness of Ag-foil to be 5.44 $\pm$ 0.27 µm which also agreed with the thickness determined from a measurement of the weight of the foil. With this, we can move onto the discussion of the calibration of S3d1 and S3d2 detectors.

4.2.2 S3d1 and S3d2 detectors

In this subsection, we will discuss the calibration of S3d1 and S3d2 detectors. To calibrate these detectors we have used the experimental data taken in the absence

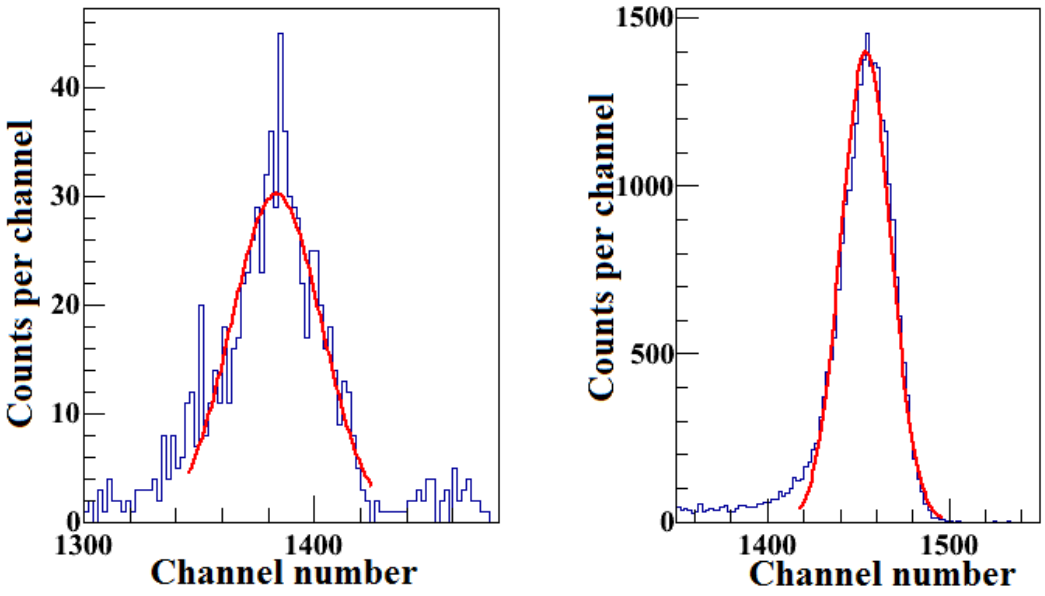

Fig. 4.3. ADC spectrum of the SSB detector with SSB trigger. (a) The peak of ^{10}C particles using the IC ^{10}C events gate. (b) The peak of ^{10}B particles using the IC ^{10}B events gate.

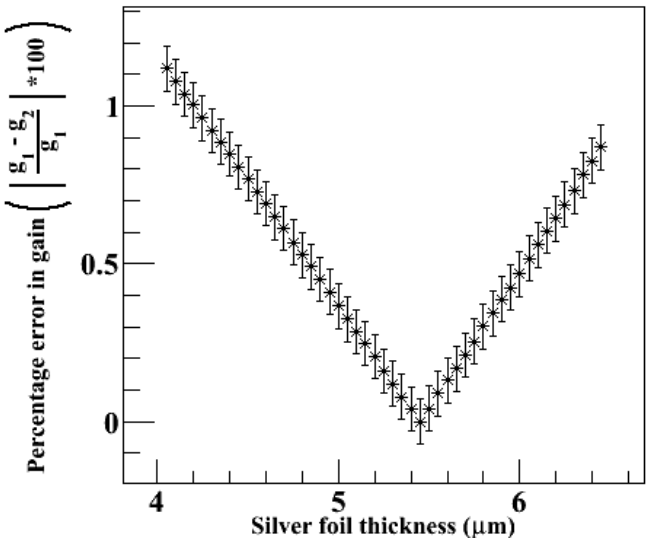

Fig. 4.4. Relative gain difference found using equation 4.3 and 4.4 versus thickness of Ag foil thickness.

of the solid H_2 target. For this scenario we have shown the material layers through which the beam particles pass (figure 4.5). From the energy loss calculation based on the stopping power table one can see that ^{10}B passes through the S3d1 detector for both 19.5 Torr and 8 Torr IC pressure settings (figure 4.6.b), whereas the ^{10}C particle only passes through S3d1 for 8 Torr IC pressure and deposits energy around $\sim$ 3.5 MeV in the active silicon region of the S3d2 detector (figure 4.6.a).

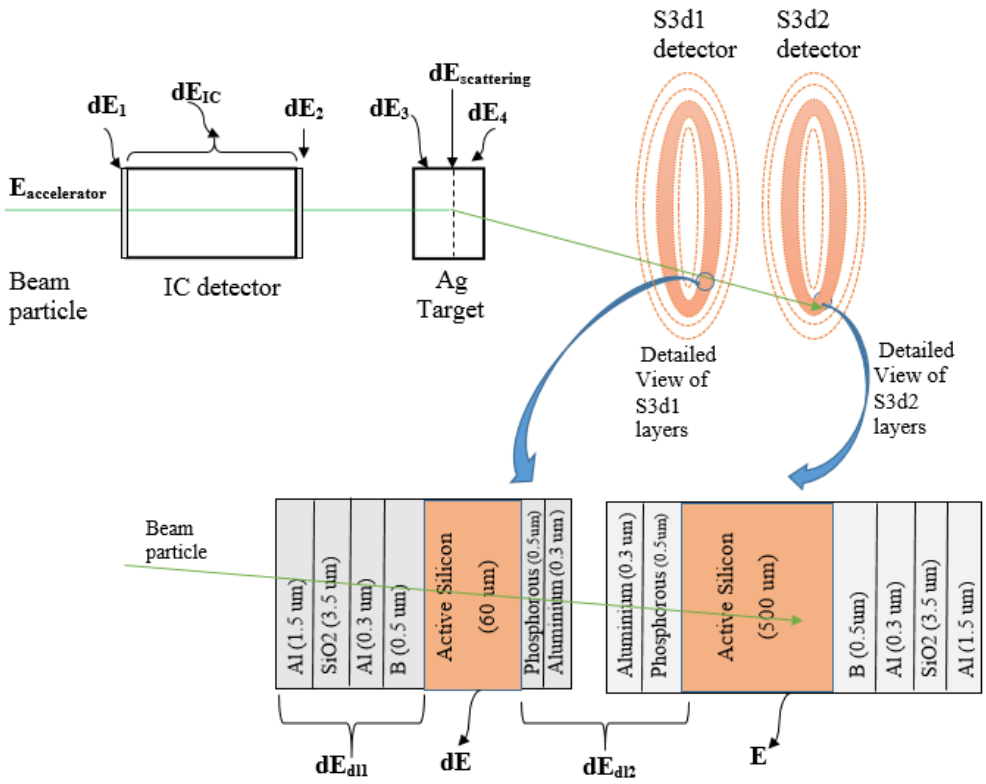

Fig. 4.5. Layout of material layers for energy loss calculation in the S3d1 and S3d2 detectors in the absence of solid H_2 target.

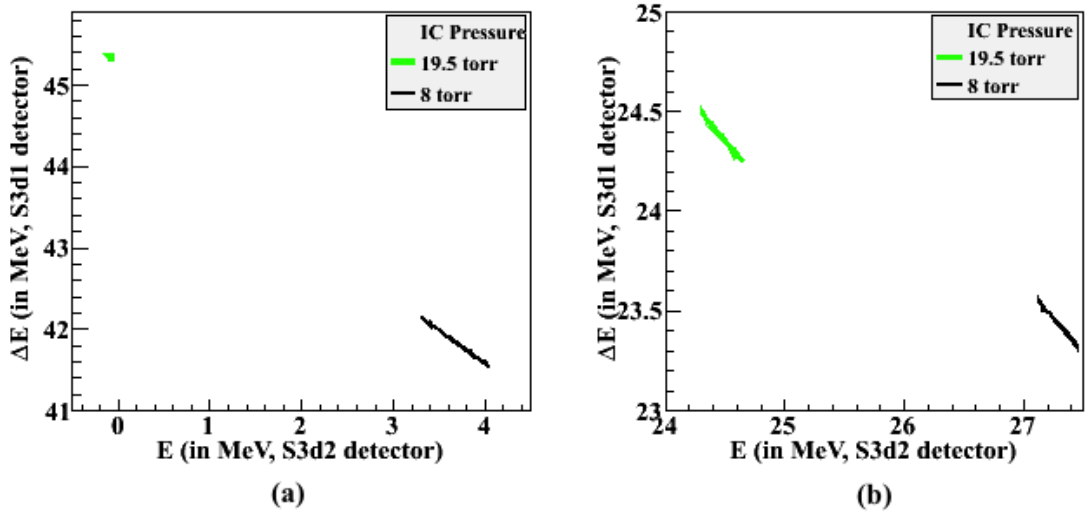

Fig. 4.6. Energy loss calculation in the S3d1 and S3d2 detector. (a) For ^{10}C particle. (b) For ^{10}B particle.

In the S3d1 detector, one side is segmented into 24 rings and each of these rings serves as an independent detector. Its opposite side is segmented into 32 sectors and each of these sectors also serves as an independent detector. Our aim is to find the gain and the pedestal for these rings and sectors. To accomplish

this, we have used the ^{10}C events from the experimental data (without solid H_2 target) taken at 19.5 Torr IC pressure. In order to calculate energy loss by the ^{10}C beam particle for a ring, we accounted for the energy loss of the incident beam in the IC. The elastic scattering ^{10}C(^{109}Ag,^{109}Ag)^{10}C at the middle of the Ag-target was used for the calibration. Energy losses in the dead layers of the S3d1 detector were also taken into account. We have used the stopping power tables [91] for the energy loss calculations. The pedestal for each ring is found using the experimental data obtained in the absence of the beam. In figure 4.7a, we have shown the pedestal data for the first ring of S3d1 detector. We have used Gaussian fitting for finding the peak position of the ^{10}C events. The mean value of the Gaussian curve ($Peak_C$) will be the peak of ^{10}C events and should correspond to the actual energy loss (E_C) by the ^{10}C scattered particle in the first ring of the S3d1 detector (figure 4.7b). Thus, the gain (g) for the first ring can be calculated as

$$g = \frac{E_C}{(Peak_C - Pedestal)} \tag{4.5}$$

The obtained gain is the quantity of our interest. Using a similar procedure we have found the gain and the pedestal for other rings of the S3d1 detector.

Once we have calibrated the detector it is advisable to check the validity of the found parameters: gain and pedestal. We can perform this check by converting the channel number of the ^{10}C events into energy using the found gain and the pedestal, and compare it with the expected energy obtained from the stopping power calculation. We have depicted the result of this verification in figure 4.8. We see discrepancies between energies obtained from the stopping power calculation and the calibrated data at higher laboratory angles. The reason for this is that the statistics are very low at higher laboratory angles (figure 4.7c). To calibrate each sector of the S3d1 detector we have used the energy deposited by the ^{10}C particle in the active silicon of the S3d1 by averaging over all the rings (difference between the energy deposition by the ^{10}C particle in the first ring and the last ring

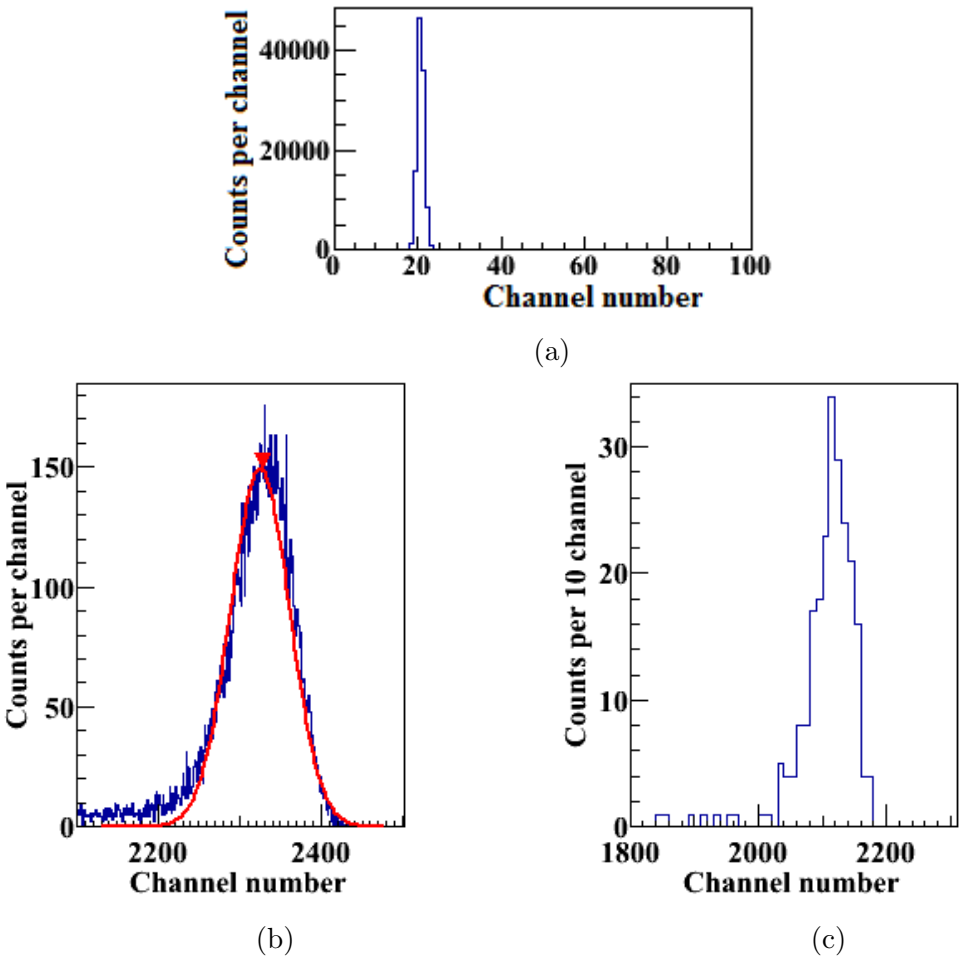

Fig. 4.7. Calibration of the S3d1 detector. (a) Pedestal data for the first ring. (b) Gaussian fitting of ^{10}C peak in ADC spectrum for first ring. (c) ADC spectrum for ^{10}C events in the outermost ring of S3d1 detector at 19.5 Torr IC pressure (without SHT target).

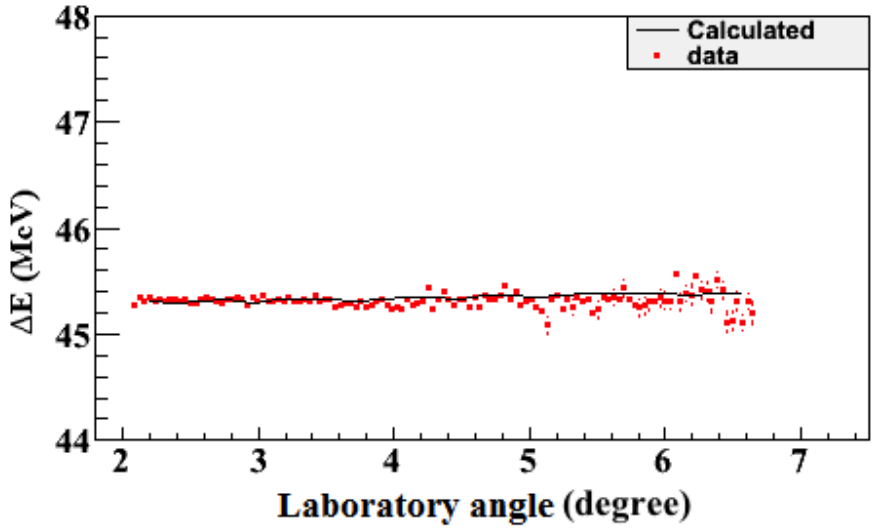

Fig. 4.8. The parameter check for the S3d1 detector calibration.

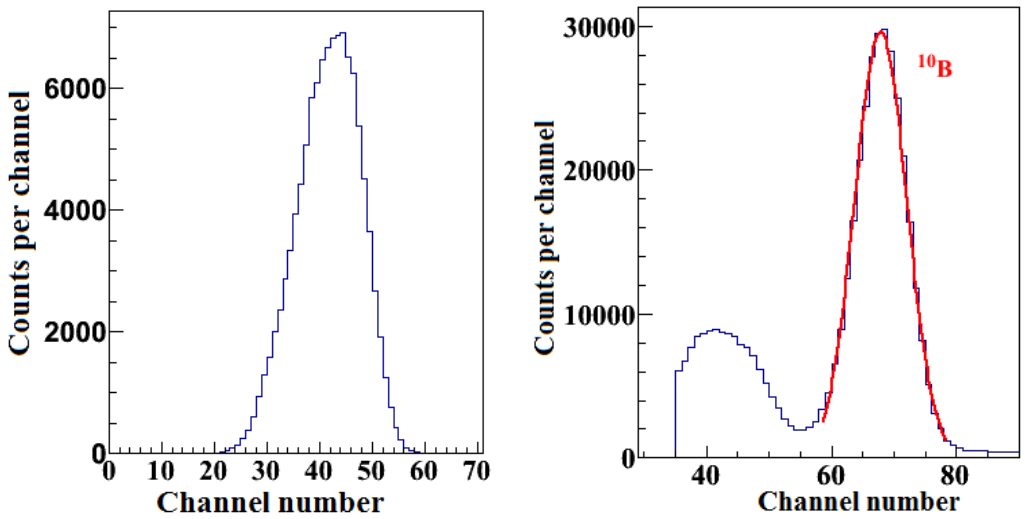

(a) (b)

Fig. 4.9. Calibration of the S3d2 detector. (a) Pedestal data for first ring of the S3d2 detector. (b) ADC spectrum for the first ring of the S3d2 detector at 19.5 Torr IC pressure setting.

of the S3d1 is $\sim$ 100 keV) and its measured peak position in the ADC spectrum.

Next, we move onto the calibration of the S3d2 detector. The S3d2 detector's ring side and sector side dead layers are the same as the S3d1 detector, but its orientation is opposite to the S3d1 detector. Its sector side is facing upstream and ring side faces downstream with respect to the direction of the incoming beam. Since the S3d2 is a thick detector ($\sim$ 500 µm), the beam particles after passing through the S3d1, deposit all the remaining energy in the active silicon of the S3d2 detector. The procedure for the calibration of the S3d2 detector is same as the S3d1 detector. Since, the ^{10}C particles are not able to reach the S3d2 detector, so we have used the ^{10}B beam events to calibrate the S3d2 detector. For each ring, we have found the energy deposited in the active silicon of the S3d2 detector for elastic scattering ^{10}C(^{109}Ag,^{109}Ag)^{10}C at the middle of the silver foil. We have shown the pedestal and the ^{10}B peak for the first ring of the detector in figures 4.9a and 4.9b. A similar procedure has been applied to calibrate the sectors of the S3d2 detector.

4.2.3 YY1 detector

In this section we describe how to calibrate the YY1 detector. We use a standard triple alpha source for this calibration. In this approach one places a radioactive source emitting alpha particles of known energies in front of the detector. The alpha source used in the experiment contained the radioactive isotopes of ^{239}Pu, ^{241}Am and ^{244}Cm, details of which are given in the table 4.1.

Table 4.1. Standard triple alpha source energies.

Isotope	Energy (MeV)	Branching Ratio (%)
^{239}Pu	5.155	73.3
	5.143	15.1
	5.105	11.5
^{241}Am	5.546	0.25
	5.513	0.12
	5.486	86.0
	5.443	12.7
	5.389	1.3
^{244}Cm	5.805	73.3
	5.763	23.6

The YY1 silicon detector is segmented in 8x16 parts (8 sectors, each having 16 rings), each of which part acts like an independent detector. We have used the triple alpha source energies corresponding to the highest branching ratio namely (5.155 MeV, 5.486 MeV, 5.805 MeV) for this calibration. For each of these incident energies of the alpha particles, we calculated energy losses in the dead layers of 0.1 µm Al and 0.05 µm Boron (equivalent 0.2 µm silicon) taking the incident angle into account. Using the stopping power calculation [91], we found that the alpha particle losses all its energy in the active silicon ($\sim$ 100 µm).

The three peaks in ADC histogram correspond (see figure 4.10) to three different energies deposited by the three different alpha particles present in the triple alpha source. We performed the least square fit to our standard calibration equation 4.2 and found the gain. We have shown the fitting of the three alpha peaks for the data obtained from the triple alpha source run (see figure 4.10).

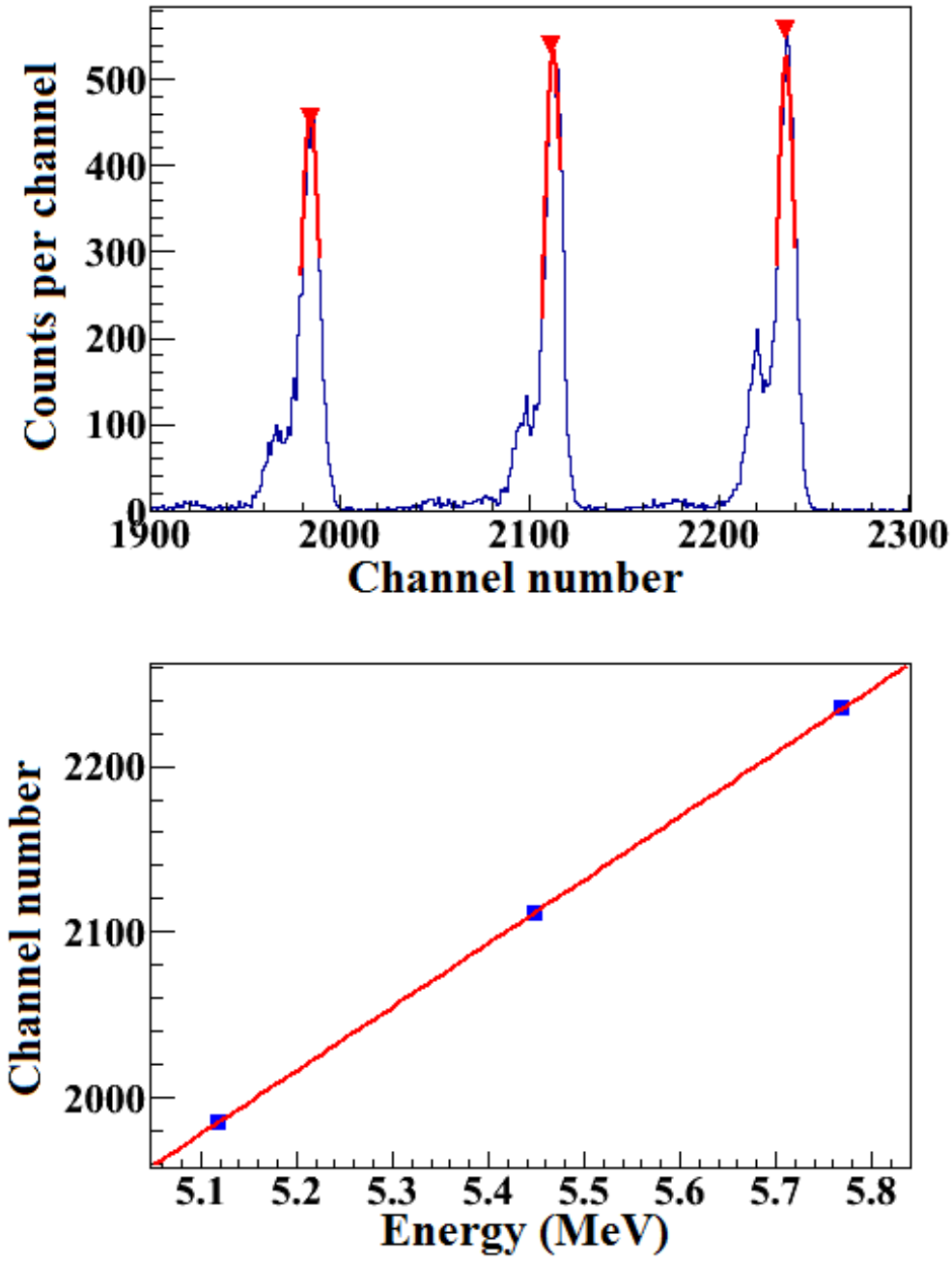

Fig. 4.10. Calibration of the YY1 detector. The top panel shows the ADC spectrum and Gaussian fitting to the peak. The bottom panel shows the least square fit to the standard calibration equation 4.2 where three data points correspond to three alpha peaks.

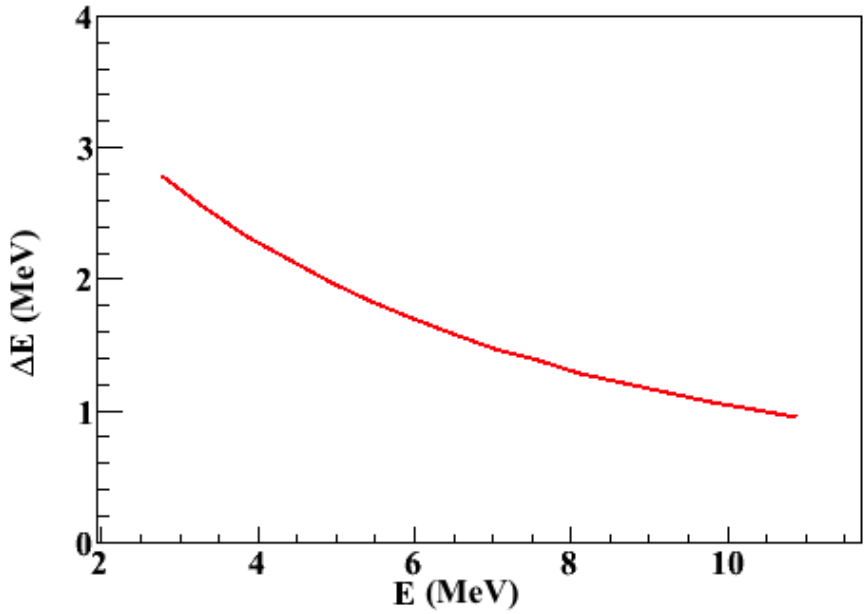

Fig. 4.11. Plot of ΔE-E for protons from ^{10}C+p elastic scattering (for incident ^{10}C energy 48.6 MeV and 100 µm SHT). ΔE and E represent the energy deposited by proton in silicon and CsI(Tl) detectors, respectively.

A similar procedure may be employed to calibrate the CsI(Tl) detector using standard energy triple alpha source and is known to be not the best way to perform the CsI(Tl) calibration for few reasons I'm going to discuss next. The CsI(Tl) is a position-sensitive detector based on the light collection through the photodiodes [92]. The light output in CsI(Tl) detector depends not only on the atomic number (Z), but also on the mass number (A) of the incident particle [93, 94]. It has also been known to show the strong dependence on the energy of the incident particle. Since our goal is to identify the light target-like particles, especially protons, which are expected to deposit energy in range of 2-12 MeV in the CsI(Tl) detector (figure 4.11), one should not use the triple-alpha source (table 4.1) for the CsI(Tl) calibration because the triple-alpha source particles deposit energy around $\sim$ 4 MeV in CsI(Tl) after passing through the mylar layer ($\sim$ 6 µm) in front of the CsI(Tl) detector, and their nature (Z, A) is very different from the protons whose identification is crucial for our experiment. However, if we use the proton particles from the experimental data ejected from the solid H_2 target due to the elastic scattering with the ^{10}C for the calibration of the CsI(Tl) detector, we can overcome our problems in following manner:

- For the protons reaching the CsI(Tl) detector we can obtain incident angle using the ring information from the YY1 detector since the detection system is designed in a coincidence manner. Hence, we can account for the position dependence in the light collection for a crystal of the CsI(Tl).

- In our experiment we are going work with the protons from the ^{10}C(p,p)^{10}C reaction. So, it is advantageous to calibrate the detector using the same particle as it automatically accounts for dependencies in Z, A and energy of incident radiation on the light production in the CsI(Tl) detector.

For these reasons we should calibrate our CsI(Tl) detector using the protons produced from the scattering of the ^{10}C with the solid H_2 target. To find the energy deposited by protons (ejected from the scattering of ^{10}C with the solid H_2) and thus use it for the calibration, the thickness of the solid H_2 target is needed. The target thickness is expected to vary with time (due to H_2 evaporation). We have therefore discussed below in Subsection 4.2.4 the procedure to measure the solid H_2 target thickness.

4.2.4 Monitoring the solid H_2 target thickness

In section 3.2.2 we discussed the formation of the solid H_2 target. Throughout the experiment we need to monitor the solid H_2 target thickness, which is of paramount importance because the yield of protons at our detectors is going to depend on it. Since we have calibrated both the thin and thick silicon detectors, we can proceed to calculate the SHT thickness.

For 19.5 Torr IC pressure, we performed the energy loss calculation in relevant material layers and found that the ^{10}C particle deposits all its energy in the S3d1 detector (figure 4.6.a), and hence the ^{10}C events in the S3d1 detector alone can be used to find the SHT thickness. Since the ^{10}C particles detected by the S3d1 detector are coming mostly from the elastic scattering with the silver foil backing of the target cell, we are going to assume the ^{10}C(^{109}Ag,^{109}Ag)^{10}C elastic reaction taking place at the middle of Ag foil while calculating the energy of the scattered

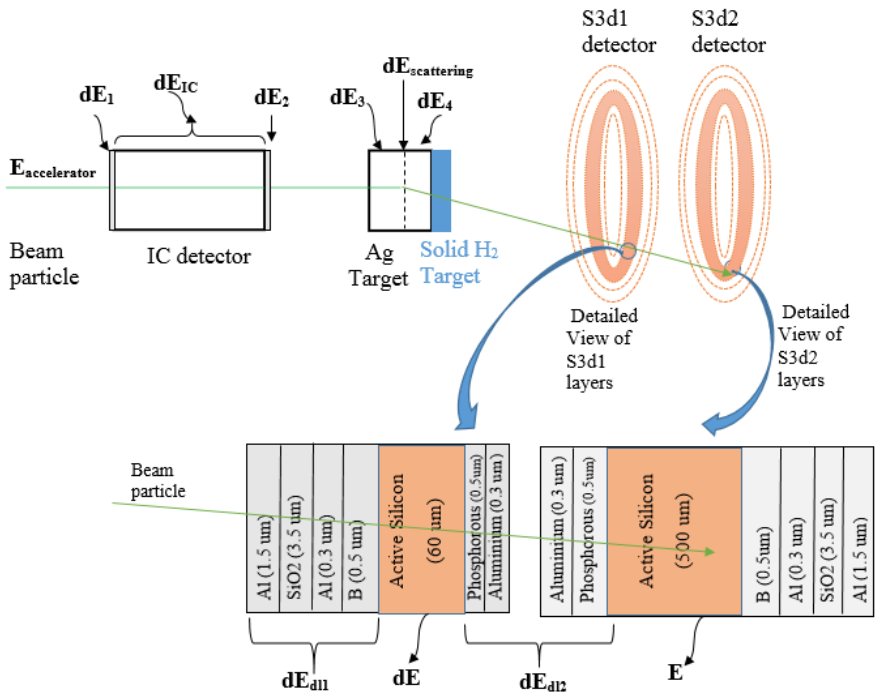

Fig. 4.12. Illustration of different region where energy losses must be taken into account to find SHT thickness. Note that the ^{10}C particles stop in the S3d1 detector for the 19.5 Torr IC pressure condition.

^{10}C. The SHT thickness can be found using stopping power calculation if the ^{10}C particle energy before and after the SHT are known. The energy of ^{10}C beam particle at the entrance of the SHT can be found if we account for the energy loss in the IC including mylar windows, and energy loss of the beam in the first half-thickness of Ag-foil and the energy of scattered ^{10}C by the remaining half thickness of the Ag-foil (figure 4.12). Thus, energy at the entrance (E_i) of the SHT target can be written as

$$E_i = E_{accelerator} - (dE_1 + dE_{IC} + dE_2 + dE_3 + dE_{scattering} + dE_4) \tag{4.6}$$

where $E_{accelerator}$ is the energy of the beam particle delivered by the accelerator; dE_1, dE_{IC} and dE_2 are the energy loss by the beam particle on passing through the mylar window at the entrance of the IC, the gas inside the IC, the mylar window at exit channel of the IC, respectively; dE_3 is the energy loss by beam

particle on passing through the first half-thickness of Ag-foil, $dE_{scattering}$ is energy change in the beam particle due to scattering at the centre of Ag-foil and dE_4 is energy loss by the beam particle on passing through the remaining half-thickness of the Ag foil.

Once we found the ^{10}C particle's energy at the entrance of the SHT, next we aim to find out the ^{10}C particle's energy after passing through SHT. From figure 4.12, it is clear that it should be the sum of the ^{10}C's energy loss in the ring side dead layer of S3d1 and the ^{10}C's energy deposited in the active silicon of the S3d1. So, the energy after passing (E_f) through the SHT can be written as

$$E_f = dE_{dl1} + dE \tag{4.7}$$

where dE_{dl1} is the energy loss by scattered beam particle on passing through the dead layer at the entrance of S3d1 detector and dE is the energy deposited by beam particle in the active silicon of S3d1 detector. Now, the SHT thickness can be written as

$$\text{thickness} = \int_{E_i}^{E_f} \frac{1}{S(E)} dE \tag{4.8}$$

where $S(E)$ is the stopping power of beam particle passing through solid H_2 target given by $-dE/dx$.

The SHT thickness variation over the time duration of the experiment is shown in figure 4.13. To find the SHT thickness for 8 Torr data run, we have used the ^{10}B beam particles. The reason for this is that the ^{10}C beam particles deposit a small amount of energy ($\sim$ 5 MeV) in the S3d2 detector, and hence its peak appears near the pedestal region in the ADC spectrum of S3d2 detector (figure 4.6). So, we planned to use the ^{10}B events to find the SHT thickness. The procedure was same as for the case of 19.5 Torr IC pressure data. We have shown the material layers in figure 4.12 where energy losses must be taken into account to find the SHT thickness.The SHT thickness for data runs at 19.5 Torr and 8 Torr IC pressure is shown in figure 4.13. The first 85 hours in the plot corresponds to the data at 19.5

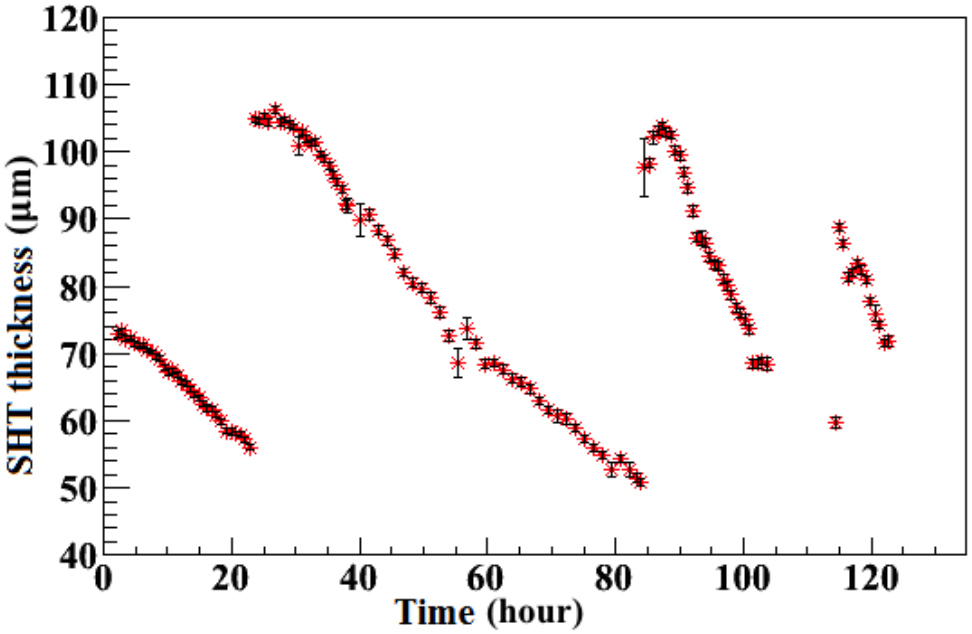

Fig. 4.13. The solid H_2 target thickness determined throughout the experiment.

Torr IC pressure and the remainder corresponds to the data at 8 Torr IC pressure

.

4.2.5 CsI(Tl) detector

In previous subsections we discussed the calibration of the S3d1, S3d2 and YY1 detectors. In this section we discuss the calibration of the CsI(Tl) detector. As it was mentioned in section 3.2.3, the CsI(Tl) detector array has 16 crystals forming an annular disk. It is positioned behind the YY1 detector in such a way that the two-crystals of the CsI(Tl) detector cover one sector of the YY1 detector. For calibration of this detector, we have used the protons detected by the CsI(Tl) detector, produced from the ^{10}C(p,p)^{10}C elastic scattering. We have fitted our standard calibration equation 4.2 with the expected energy deposited by the proton in the CsI(Tl) detector, and the ADC channel number for these proton events. For each experimental data run ($\sim$ 1 hour long), the proton statistics from the ^{10}C(p,p)^{10}C reaction were very poor, and hence we decided to combine few consecutive data runs together over which the SHT thickness did not vary significantly. We identified thirteen consecutive data runs to get good statistics. For these data

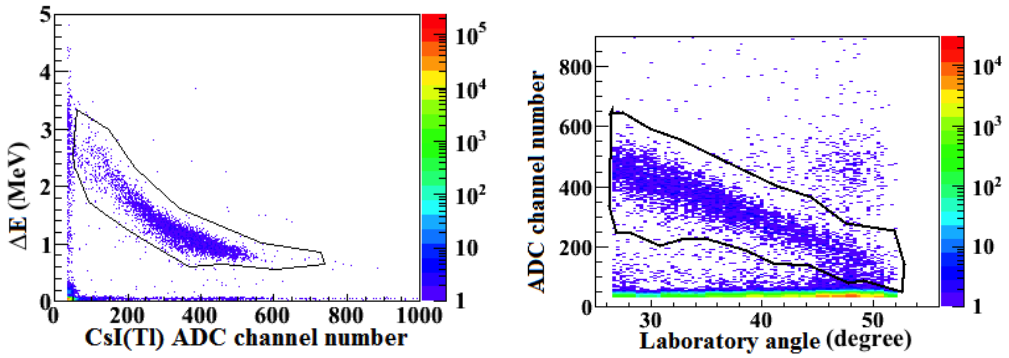

(a) (b)

Fig. 4.14. Selection of the proton events generated from the scattering of the ^{10}C particle with protons in the solid H_2 target. (a) Proton event selection from ^{10}C beam particle using silicon and CsI(Tl) detector. (b) Selection of elastic proton events from $^{10}C + p$ scattering using CsI(Tl) detector.

runs SHT thickness varied from 97.8 µm to 106 µm . Below, we outline the steps used for calibrating the CsI(Tl) detector.

1. **Identification of protons**

   To identify the target-like particles after reaction in the target we can use the energy loss (ΔE in YY1) information and the remaining total energy deposited (E in CsI(Tl)) by particles, as these quantities depend on the atomic number (Z) number and the mass number (A) of the incident particle, respectively. Figure 4.14a shows the energy deposited (ΔE) in the YY1 detector and the CsI(Tl) ADC's channel number with ^{10}C events selected by the ionization chamber. The events inside the polygon are the selected scattered proton events. To identify the elastic proton events we constructed the kinematic plot of protons energy (in form of ADC channel number) versus the measured scattering angle. We have inscribed the locus of elastic proton in the figure 4.14b.

2. **Determining the proton energy at the entrance of the CsI(Tl) detector**

   In our next step, we performed the stopping power calculations to find the energy of the proton at the entrance of the CsI(Tl) detector. We assumed

$^{10}C + p$ elastic scattering at the centre of the SHT ($\sim$ 101.9 µm). We have shown a layout of the material layers in figure 4.15 through which energy losses have been taken into account. We have shown the proton energy deposited in the active region of the CsI(Tl) detector for different laboratory angles in figure 4.16.

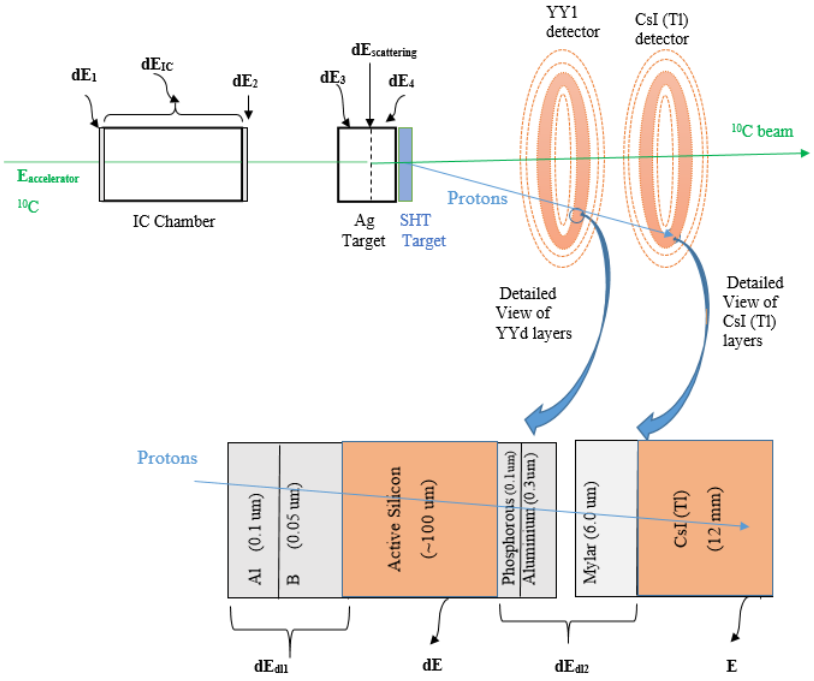

Fig. 4.15. Material layers to account for energy loss for the purpose of calibration of CsI(Tl) detector.

3. Proton peak determination in CsI(Tl) ADC spectrum

Although each CsI(Tl) crystal uses a single shaper amplification unit we need to find the shaper's gain for each angular bin to take into account any dependence on light collection efficiency. We grouped the 16 YY1 rings into 4 groups for the purpose of this calibration (based on statistics). Next, we construct the ADC spectrum of CsI(Tl) for each of these groups with events that are inside the proton polygon and the elastic proton polygon generated in step 1, and fall inside the ^{10}C ionization chamber gate (figure 4.1b).

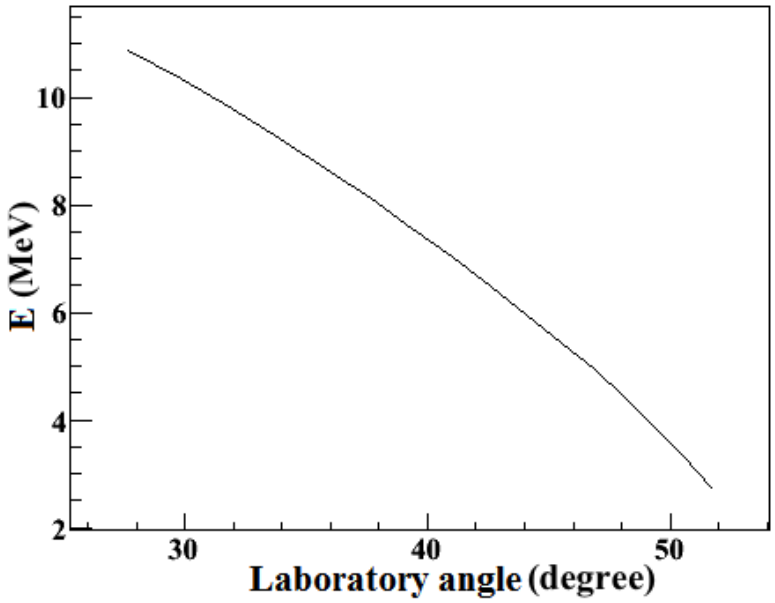

Fig. 4.16. Kinematics of the proton from elastic scattering of ^{10}C (E_{lab}=48.6 MeV) with the solid H_2 target. The quantity E on Y-axis represents the energy at the entrance of the CsI(Tl) detector after energy loss in the target and detector dead layers.

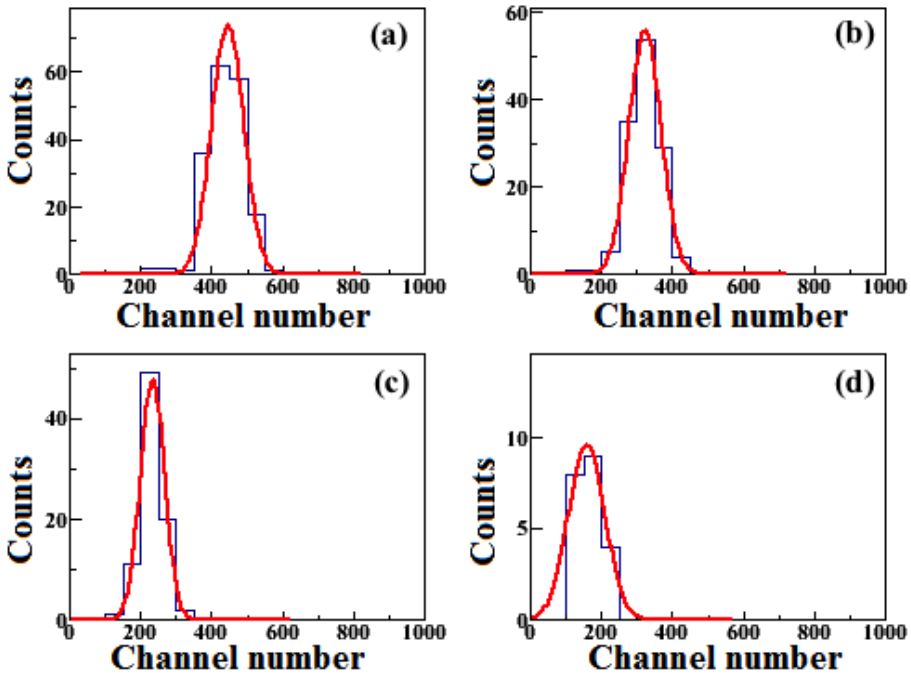

Fig. 4.17. CsI(Tl) ADC spectrum for one of the 16 crystals in CsI(Tl) array to find the proton's peak. ^{10}C IC gate (figure 4.1b) and proton events inside the polygon (figure 4.14a and 4.14b) as condition have been used to select the protons from ^{10}C+p elastic scattering. (a) For YY1 rings 1-4. (b) For YY1 rings 5-8. (c) For YY1 rings 9-12. (d) For YY1 rings 13-16.

We have shown such a plot for one of the 16 crystals of the CsI(Tl) detector in figure 4.17. For each of the spectra we found the peak position using Gaussian fitting.

4. **Finding gain for amplifier of CsI(Tl)**

We define four groups of the YY1 rings, each of which consists of four consecutive rings. For each such group, we calculated the average proton energy deposited in the CsI(Tl) detector. We used the peak position found in the step 3 and the calculated average proton energy, to fit the linear equation 4.2, and thus we found the gain for that group of rings in a CsI(Tl) crystal. Similarly we found the gain for other 3 group of rings in a CsI(Tl) crystal.

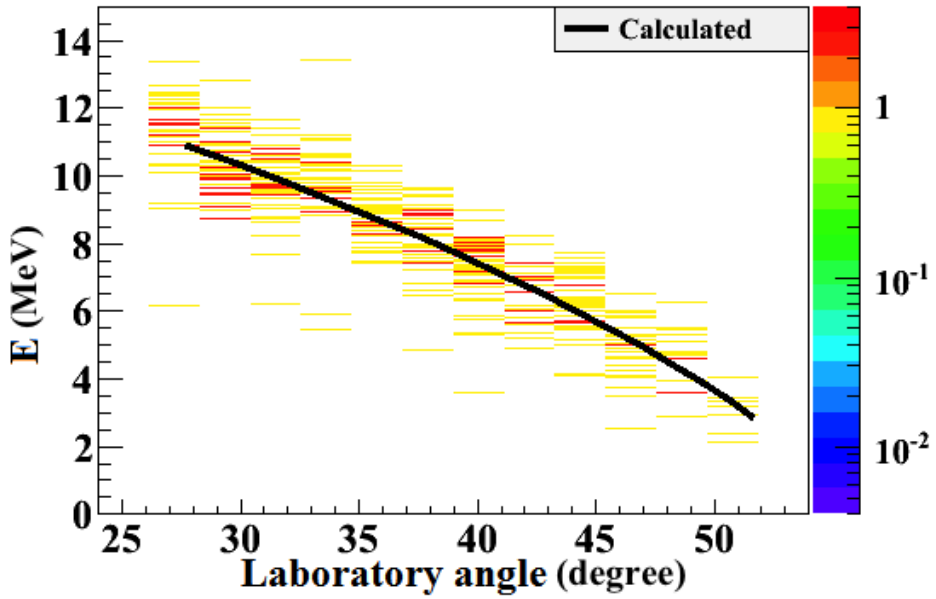

Fig. 4.18. The measured energy (E in CsI(Tl)) and scattering angle of the scattered protons from the ^{10}C+p elastic scattering. The black curve shows the calculated values.

We have shown the calibrated energy (E in CsI(Tl)) in figure 4.18 for the different laboratory angles. The calculated energy curve obtained from stopping power calculation is also overlaid for comparison.

4.3 Particle identification using ΔE-E analysis

The calibrated energies allow us to define the final identification condition for the scattered particles. The target-like particles ejected from the solid H_2 target were detected using the thin silicon detector (YY1) followed by the thick CsI(Tl) detector. Since the YY1 detector is thin, all the ejectiles pass through it, losing energy ΔE, and stop in the thick CsI(Tl). We know that the energy loss (ΔE) depends on the atomic number of the impinging particle and the energy deposited (E) depends on the mass number of impinging particle. Hence the two signals: the energy signal from the YY1 detector and the CsI(Tl) detector, can be used to identify the target-like particles, and thus serves as a ΔE-E telescope. The particle identification spectrum is shown in (figure 4.19). The protons identified by this technique include both elastic and inelastic scattering channels. We observed only protons in our experiment because the beam particles do not have enough energy to produce the deuterons and tritons. The required energies (in laboratory frame) are listed in table 4.2 for different combinations of reactions that could happen hypothetically.

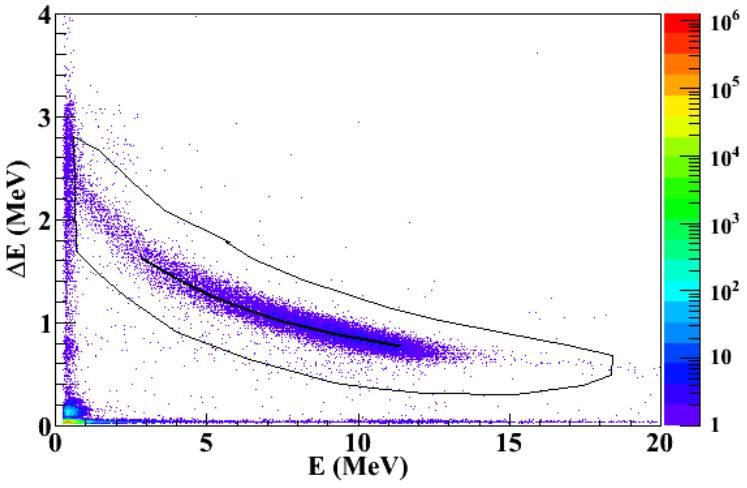

Fig. 4.19. Particle identification plot for the light target-like particles. Events inside the polygon are protons. ΔE and E represent the energy deposited in silicon (YY1) and CsI(Tl) detectors, respectively.

In a similar manner, we have used the energy signal from the thin S3d1 detector and the thick S3d2 detector, which also form a ΔE-E telescope, and enables us to

Table 4.2. Kinematic calculations for nuclear reactions. The KE^{lab}_{min} is the energy (in laboratory frame) required to initiate the given reaction with proton as target at rest. Expression for Q-value is given in equation 4.9.

Reaction	Q-value (in MeV)	KE^{lab}_{min} (in MeV)
$^{10}C(p,p)^{10}C$	0.	0.
$^{10}C(p,d)^{9}C$	-19	208.1
$^{10}C(p,t)^{8}C$	-27	295.4

identify the beam-like particles (see figure 4.20). We observe two clusters in the ΔE-E spectrum of the beam-like particles.

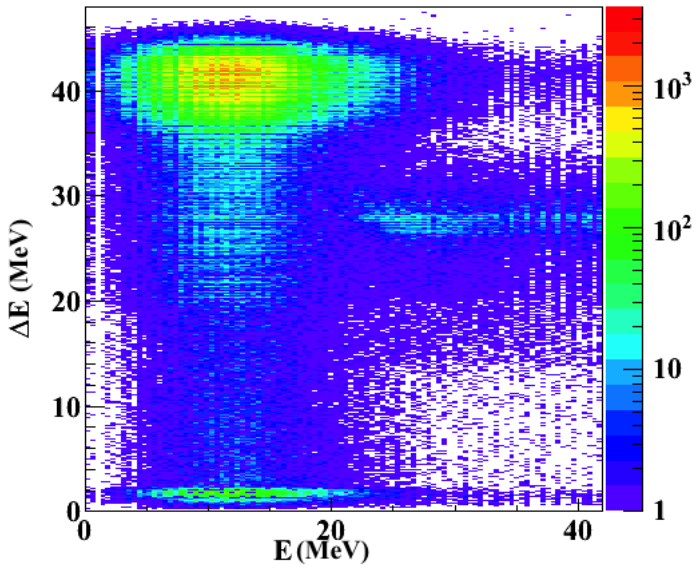

Fig. 4.20. Particle Identification plot for heavy particles in the experiment.

The cluster of events peaked with higher energy in the S3d1 detector corresponds to the ^{10}C particles whereas the other cluster corresponds to the ^{10}B particles present in the beam as contamination.

4.4 Kinematics of protons

To find the kinematic locus of the protons we have used the energy information from the YY1 and the CsI(Tl) detector. The measured energy overlaid with the calculated curve is shown in figure 4.21, clearly identifying the locus of the elastic protons.

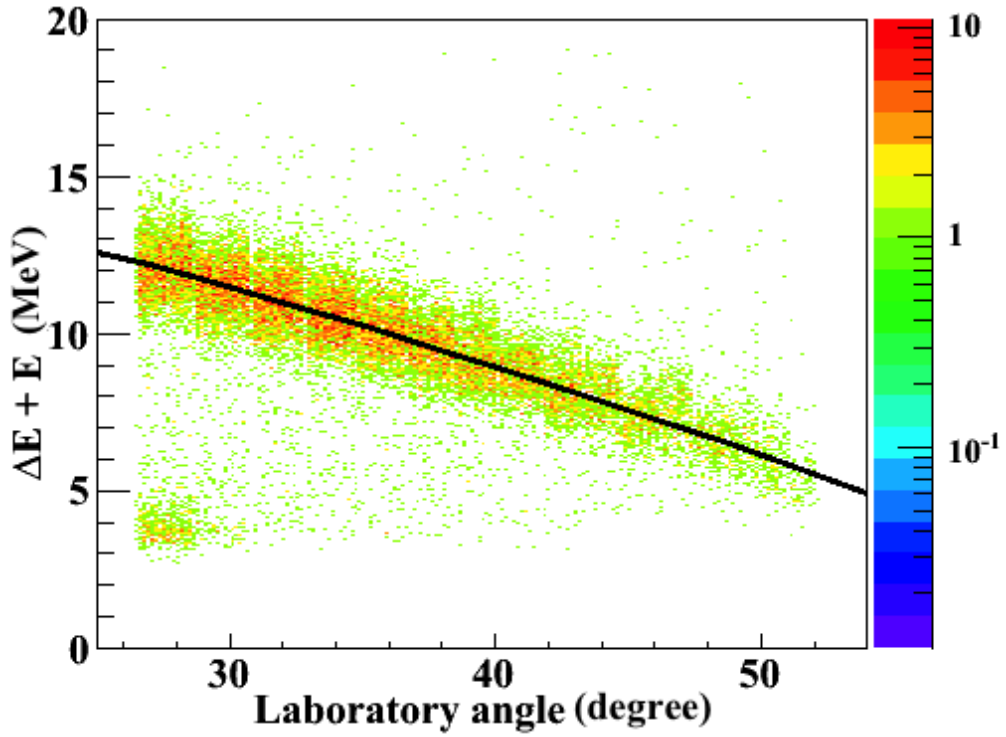

Fig. 4.21. Plot of proton energy deposited in the detectors versus laboratory angle.

4.5 Excitation energy spectrum for ^{10}C

In section 4.3 we discussed the identification of protons from the $^{10}C+p$ scattering, and it was not clear whether the events inside the proton selection condition (see figure 4.19) belong to the elastic or inelastic $^{10}C + p$ reaction channel. To identify this, we reconstructed the Q-value spectrum from the measured energy and scattering angle.

The Q-value of a reaction is defined as the change in the total kinetic energy of particles in initial state to the final state. It can also be written as a difference in the total mass energy of particles in the initial state to the final state. In general, for a reaction: $a + b \rightarrow c + d$, the Q-value can be written as

$$Q = m_a + m_b - m_c - m_d \tag{4.9}$$

where m_a, m_b, m_c, and m_d are the masses of the species a, b, c, and d, respectively; the equation is written in natural units (speed of light is taken as unity).

If the species c or d is in an excited state, its mass will be different from the rest mass and hence, the Q-value becomes an unknown quantity. It can be measured from the experiment if we can convert the right-hand-side (RHS) of the equation 4.9 into quantities that can be measured in the experiment. By performing a little bit of algebra we can write the RHS of equation 4.9 in terms of the kinetic energy and the scattering angle of the final state ground state species. Consider the species d is in the excited state, then we can write equation 4.9 as

$$\begin{aligned} Q =& m_a + m_b - m_c \\ & - \sqrt{\begin{array}{l} m_a^2 + m_c^2 - m_b^2 + 2m_b(KE_a + m_a) \\ \quad - 2(KE_a + m_a + m_b)(KE_c + m_c) + 2P_aP_c\cos(\theta_c) \end{array}} \end{aligned} \tag{4.10}$$

where KE_a and KE_c are the kinetic energy of the species a and c, respectively. P_a and P_c are the relativistic momenta of the species a and c, respectively. θ_c is the laboratory angle of species c. The relativistic momentum can be found using energy-momentum relation given as

$$P_a = \sqrt{(KE_a + m_a)^2 + m_a^2}, \tag{4.11}$$

and

$$P_c = \sqrt{(KE_c + m_c)^2 + m_c^2}. \tag{4.12}$$

We used equation 4.10 to determine the Q-value of the reaction ^{10}C(p,p)^{10}C with a being ^{10}C, b being the protons, c is the scattered protons detected by YY1/CsI(Tl) detector. This technique to measure the Q-value of a nuclear reaction is also called the missing mass technique.

We have shown the obtained Q-value spectra for the ^{10}C(p,p)^{10}C reaction in figure 4.22. We observed two peaks in each spectrum. The peak with Q-value around zero MeV should correspond to the ground state of ^{10}C (elastic channel) whereas the peak with Q-value around 3 MeV corresponds to the first excited

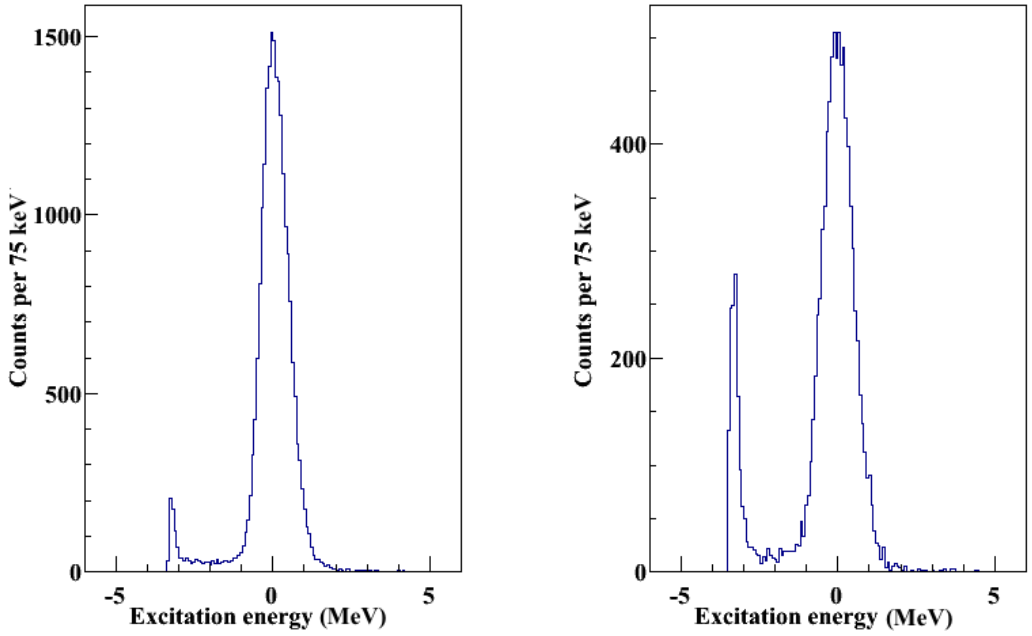

(a) (b)

Fig. 4.22. Q-value spectrum of ^{10}C(p,p)^{10}C reaction. (a) Data at 19.5 Torr IC pressure setting. We have used proton events inside polygon (see figure 4.19) and ^{10}C IC events (see figure 4.1b) as gate. (b) Data at 8 Torr IC pressure setting. We have used proton events inside polygon (see figure 4.19) and ^{10}C IC events (see figure 4.1a) as gate.

state of ^{10}C (inelastic channel).

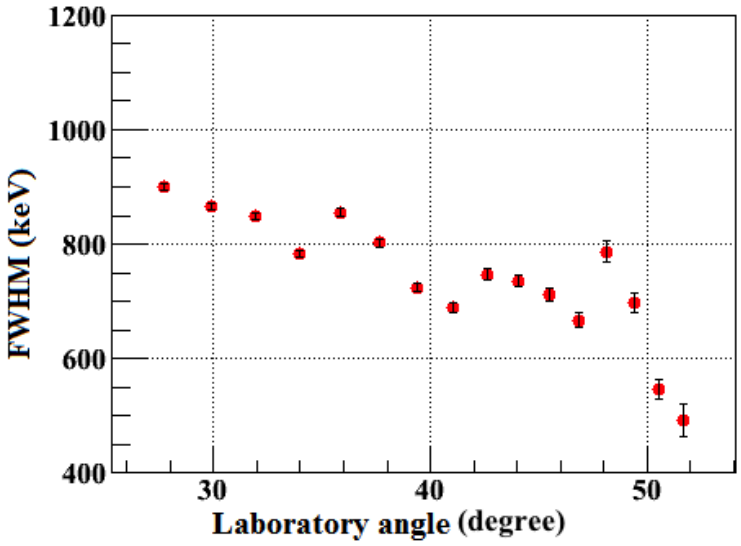

Fig. 4.23. Full-width at half-maxima (FWHM) for the ground state of ^{10}C.

We have made a few simplifications while constructing the Q-value spectrum. We have assumed that the scattering of ^{10}C with a proton has occurred at the

centre of the solid H_2 target. We have also assumed that the ejected protons passed through the centre of the angular bin of the detector. These assumptions affect the calculated energy of proton at the scattering centre, and hence, give rise to an additional energy spread in the Q-value spectrum. For each angular bin, we have shown the Full-Width-at-Half-maxima (FWHM) for the ground state of ^{10}C in figure 4.23. The higher value of FWHM for lower scattering angle is due to the fact that the size of angular bin for the lower scattering angle is large as compared to the size of angular bin at larger scattering angle. Overall, the Q-value peak for the elastic channel has FWHM = 833 ± 2 keV.

4.6 Measurement of differential cross section

The final goal of this study was to measure the differential cross section ($d\sigma/d\Omega$) of the ^{10}C(p,p)^{10}C elastic reaction for each scattering angle. The differential cross section is given as:

$$\frac{d\sigma}{d\Omega} = \left[\frac{N^s}{N^{in}}\right] \times \left[\frac{M_t}{N_A} * \frac{1}{\rho T} * \frac{1}{d\Omega}\right] \tag{4.13}$$

where N^s and N^{in} are the number of scattered and incident particles, respectively. $d\Omega$ is the differential solid angle, M_t and ρ are the molar mass and density of the solid H_2 target, respectively, N_A is the Avogadro's number, and T is the thickness of the solid H_2 target.

4.6.1 Counting scattering flux

To find the differential cross section for each scattering angular bin, we need to first measure the scattering flux, i.e. the number of elastic protons produced from the $^{10}C + p$ reaction for each ring (angular bin) of the YY1 detector. Note our charged particle detector (YY1) is segmented in 16 concentric rings so we can measure the differential cross section for 16 different scattering angular bins. In section 4.5, we discussed how the excitation spectra (Q-value spectra) can be used to identify the elastic protons. We used this method and constructed the Q-value spectra for

each ring of the YY1 detector. To count the number of particles produced from elastic scattering, we fitted the peak in the excitation spectra corresponding to the ground state of ^{10}C using a Gaussian and a linear function together (figure 4.24). Note here we have assumed that the background under the peak is linear throughout. The fitting function can be written as

$$f(x) = \left[H * e^{\left(-0.5*\left[\frac{x-\mu}{\sigma}\right]^2\right)} \right] + [c_0 + c_1 * x] \tag{4.14}$$

where μ, σ and H are the peak position, standard deviation width and amplitude of the Gaussian peak, respectively. c_0 and c_1 are constant parameters of the linear background function.

In the spectrum (figure 4.24), the two vertical lines show the 3σ region around the mean position. The 3σ region around the mean in the Gaussian function covers 99.7% of the area under the peak. We also measured the signal-to-noise ratio (SNR) defined as

$$SNR = \frac{\text{Number of particles inside the } 3\sigma \text{ range in the histogram}}{\text{Number of background events inside the } 3\sigma \text{ region}}. \tag{4.15}$$

For the given angular bin (YY1 ring) based on the fitting (figure 4.24) , the total number scattered protons for the entire data runs can be written as

$$N^{proton}_{scattered} = N^{total} - N^{background} \tag{4.16}$$

where, N^{total} is the number of particles in the histogram within the 3σ range, $N^{background}_i$ is the number of particles under the estimated linear background function within the 3σ range.

The quantity $N^{proton}_{scattered}$ has been used as N^s in equation 4.13 to evaluate the differential cross section.

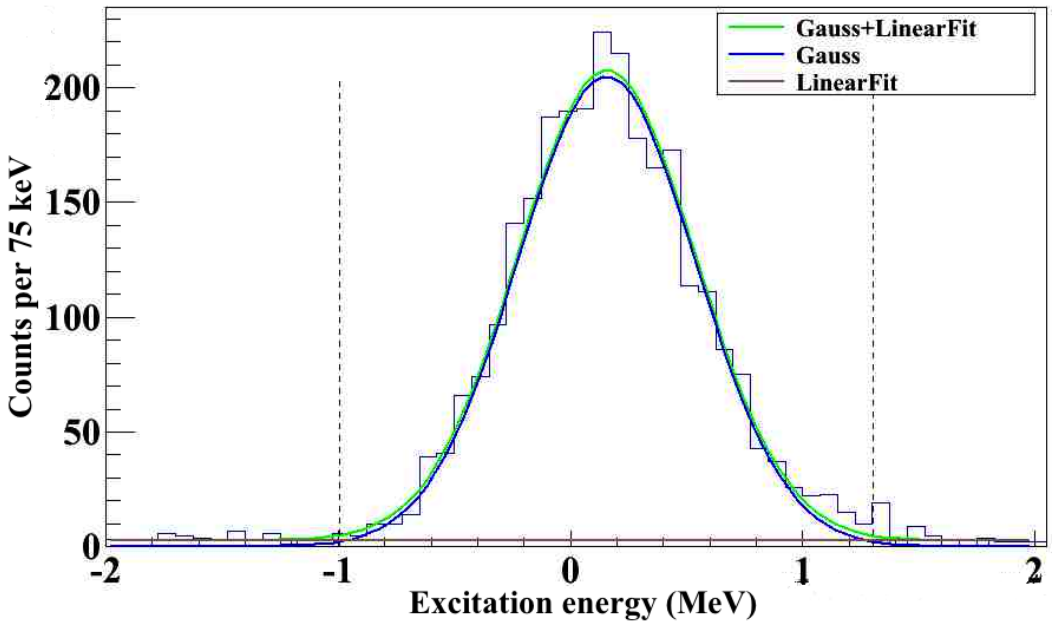

Fig. 4.24. Q-value spectrum for ^{10}C(p,p)^{10}C reaction at IC pressure of 19.5 Torr for the first ring of the YY1. The two vertical dashed lines show the 3σ range around the peak position.

4.6.2 Counting incident flux

To count the incident ^{10}C particles we used the information from IC scaler measurements. We know from the IC ADC spectrum (see figure 4.1) that the ^{10}C as well as the ^{10}B particles are present in the beam, thus IC scaler measurements include the counting of both ^{10}C and ^{10}B particles. We can scale the total IC scaler counts to estimate the incident ^{10}C particles using the IC ADC spectrum. We must use the same ^{10}C IC ADC spectrum gate window defined in section 4.1 (see figure 4.1) since we analysed the scattered protons for that selection window in the data analysis. We have measured the ^{10}C particles for each data run separately. For this we have found the ratio of the integral of ^{10}C particles (using defined gate window) to the total integral in IC ADC spectrum, together with the data acquisition live-time (DAQ) correction. The data acquisition live-time (τ) is an important feature that must be included while counting the incident flux. The data acquisition system can not process all the events incident on the YY1 or S3d1 (YY1 and S3d1 was in trigger) detectors because it requires a finite time to process and store these events. The events from our charged particle detectors are

stored only when there is an accepted trigger, thus we need to correct the incident ^{10}C beam particle by the same ratio. The DAQ live-time is given as:

$$\tau = \frac{\text{Total accepted trigger}}{\text{Total free trigger}}. \tag{4.17}$$

Thus, the effective number of the incident ^{10}C particles (N_i^{10C}) in an i^{th} run can be written as

$$N_i^{10C} = (\text{IC scaler counts in the } i^{th} \text{ run}) * \tau_i * \frac{N_i^{ADC\_10C}}{N_i^{ADC\_total}} \tag{4.18}$$

where τ_i is DAQ live-time for the i^{th} data run, N^{ADC_10C} is the number of ^{10}C particles in the IC ADC spectrum for the i^{th} data run, and $N_i^{ADC\_total}$ is the total number of particles in the IC ADC spectrum for the i^{th} data run. The quantity N^{in} in equation 4.13 can be expressed as

$$N^{in} = \sum_i N_i^{10C} \tag{4.19}$$

As we have seen that there is a term for solid H_2 target thickness in the formula of the differential cross section (equation 4.13), which is not constant in time, and we have already measured its variation for each data run in section 3.2.2. To calculate the differential cross section systematically, we have to modify the term "$N^{in} * T$" in equation 4.13 in following manner

$$N^{in} * T = N_1^{10C} * t_1 + N_2^{10C} * t_2 + ... \tag{4.20}$$

where t_i is the solid H_2 target thickness for i^{th} data run.

The DAQ live-time for each data run is shown in figure 4.25.

4.6.3 Solid angle

The solid angle for each angular bin (one ring of the YY1 detector) is given as

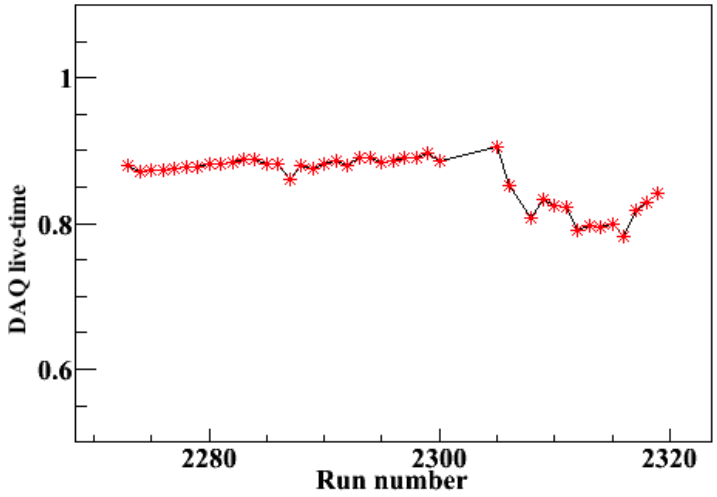

Fig. 4.25. DAQ live-time for data runs at 8 Torr IC pressure setting.

$$d\Omega = 8d\phi * \sin(\theta_{lab}) * d\theta_{lab}, \tag{4.21}$$

where

$$\begin{aligned} \theta_{lab} &= \frac{\theta_{lab}^{out} + \theta_{lab}^{in}}{2}, \\ d\theta_{lab} &= \theta_{lab}^{out} - \theta_{lab}^{in}, \end{aligned} \tag{4.22}$$

with θ_{lab}^{out} and θ_{lab}^{in} are angle subtended by the outer circumference and the inner circumference of a given ring of the YY1 detector at the scattering centre, respectively, and θ_{lab} is an average of angles subtended by the outer radius and the inner radius of the given ring of the YY1 detector at the scattering center, and $d\phi$ represents the azimuthal angle corresponding to one of the 8 sectors of the YY1 detector. The factor of $8d\phi$ in equation 4.21 comes from the integration over the azimuthal angle.

4.6.4 Geometric efficiency correction

The geometric efficiency of a detector for a given angle is defined as a ratio of total number of particles incident at the detector to the total number of particles detected by the detector at that angle. We used the Monte Carlo (MC) technique

to estimate the geometric efficiency of the YY1/CsI(Tl) detector. We have shown its variation over laboratory angles in figure 4.26.

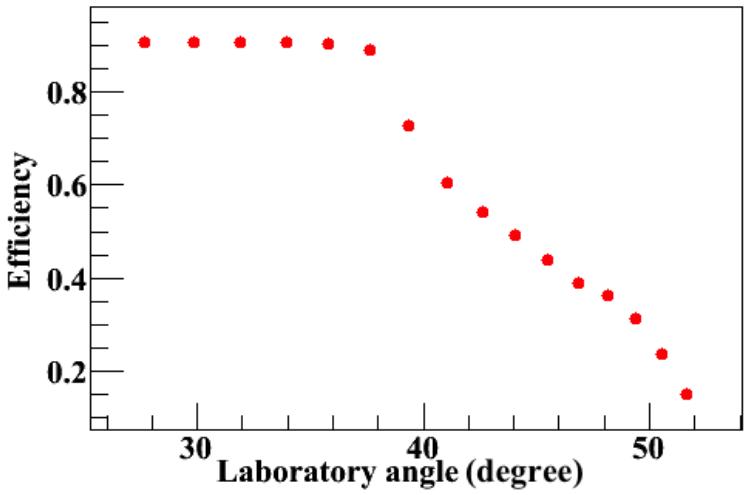

Fig. 4.26. Simulated geometric efficiency of YY1/CsI(Tl) detector.

We know that the efficiency of the detector also depends on the exposure time to radiation which has not been accounted for in the calculations.

4.6.5 Uncertainty in the measurement of differential cross section

The final expression used to measure the differential cross section is

$$\frac{d\sigma}{d\Omega} = \left[\frac{N_{scattered}^{proton}}{\sum_i N_i^{10C} * t_i}\right] * \left[\frac{M_t}{N_A} * \frac{1}{\rho} * \frac{1}{d\Omega_{eff}}\right] * 10^{31} \text{ mb/sr} \tag{4.23}$$

with

$$d\Omega_{eff} = 8d\phi * \text{Efficiency} * \sin(\theta_{lab}) * d\theta_{lab} \tag{4.24}$$

where

$M_t = 2 * 1.008$ g/mol (Molar mass of H_2),

$\rho = 0.086 * 10^6$ g/m^3 (Density of the solid H_2 target),

$N_A = 2 * 6.023 * 10^{23}$ (Avogadro's number),

Efficiency = Geometric efficiency of the YY1 detector.

To measure the uncertainty, we found the uncertainty in the number of scat-

tered particles, solid H_2 target thickness and the solid angle detection efficiency of the detector. We have taken the uncertainty in the SHT thickness as 5% (due to the uncertainty in stopping power tables) and detection efficiency as 5% (due to uncertainty from the detector geometry and Monte Carlo simulation). Note that there is no uncertainty in the number of incident particle. Hence, we can write the uncertainty in the measurement of the differential cross section as:

$$\Delta\left(\frac{d\sigma}{d\Omega}\right) = \frac{d\sigma}{d\Omega} * \sqrt{\left[\frac{\sigma^2_{N^{proton}_{scattered}}}{(N^{proton}_{scattered})^2} + \frac{\sum_i \sigma^2_{t_i} * (N^{10C}_i)^2}{(\sum_i N^{10C}_i * t_i)^2} + \frac{\sigma^2_{Eff}}{(\text{Efficiency})^2}\right]} \tag{4.25}$$

with

$$\begin{aligned}
\sigma^2_{N^{proton}_{scattered}} &= N^{total}_i + N^{background}_i, \\
N^{proton}_{scattered} &= N^{total}_i - N^{background}_i, \\
\sigma^2_{t_i} &= \frac{25}{10000} * (t_i)^2, \\
\sigma^2_{Eff} &= \frac{25}{10000} * (\text{Efficiency})^2.
\end{aligned} \tag{4.26}$$

The differential cross sections measured in the laboratory frame for ^{10}C incident energy E_{lab} = 45.45 MeV and 48.21 MeV, are displayed in the figure 4.27.

The differential cross section measured in laboratory frame can be converted into the centre-of-mass (CM) frame by finding the Jacobian of the transformation ($J_{lab\rightarrow cm}$) from the laboratory frame to the CM frame. Thus, the differential cross section in the CM frame can be written as:

$$\frac{d\sigma}{d\Omega_{cm}} = \frac{d\sigma}{d\Omega_{lab}} * J_{lab\rightarrow cm} \tag{4.27}$$

where

$$J_{lab\rightarrow cm} = \frac{d\Omega_{lab}}{d\Omega_{cm}} = \left[\frac{\sin(\theta_{lab}) * d\theta_{lab}}{\sin(\theta_{cm}) * d\theta_{cm}}\right]. \tag{4.28}$$

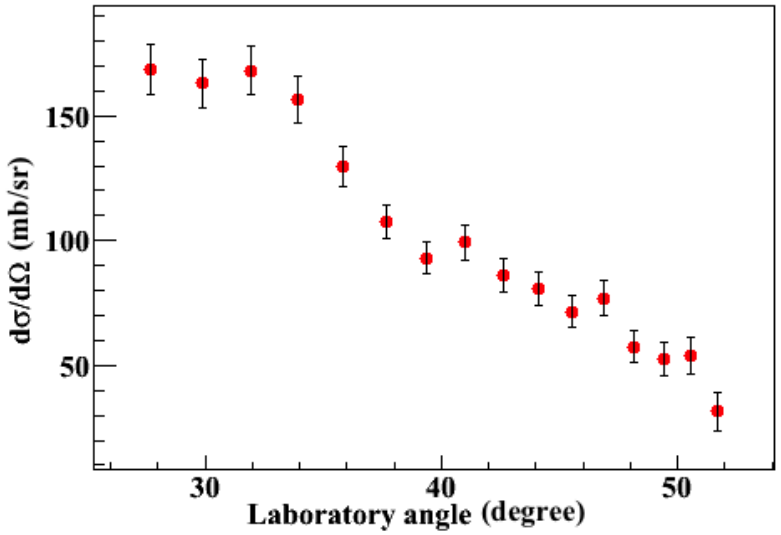

(a)

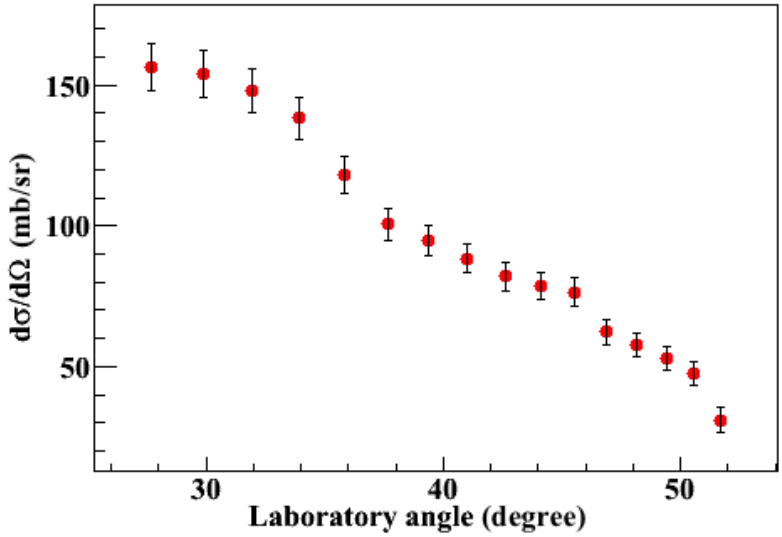

(b)

Fig. 4.27. Differential cross section in laboratory frame for ^{10}C(p,p)^{10}C elastic reaction. (a) For incident ^{10}C energy E_{lab} = 48.21 MeV (8 Torr IC pressure setting). (b) For incident ^{10}C energy E_{lab} = 45.45 MeV (19.5 Torr IC pressure setting).

The laboratory angle and the CM angle are connected via the formula:

$$\tan(\theta_{lab}) = \frac{\sin(\theta_{cm})}{\gamma\left(v\frac{E_c^{cm}}{P_c^{cm}} - \cos(\theta_{cm})\right)} \tag{4.29}$$

where

$v = \frac{\sqrt{(KE_a+m_a)^2-m_a^2}}{KE_a+m_a+m_b}$ (Velocity of the CM frame relative to the laboratory frame)

$\gamma = \frac{1}{\sqrt{1-v^2}}$ (Lorentz factor)

$E_c^{cm} = \frac{E_{cm}^2 - m_d^2 + m_c^2}{2E_{cm}}$ (Scattered proton's energy in the CM frame)

$E_{cm} = \sqrt{m_a^2 + m_b^2 + 2E_a m_b}$ (CM energy of the $^{10}C + p$ system)

$P_c^{cm} = \sqrt{(E_c^{cm})^2 - m_c^2}$ (Relativistic momentum of the scattered proton in the CM frame).

The equation 4.29 is written in natural units (speed of light is taken as unity). We have displayed the graph of the CM angle and the laboratory angle for the ^{10}C(p,p)^{10}C elastic reaction in figure 4.28.

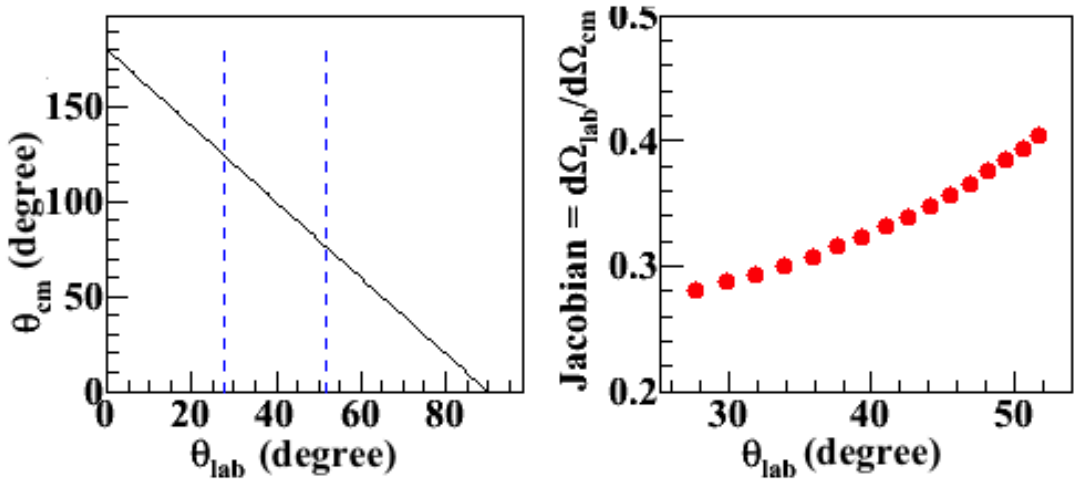

Fig. 4.28. (a) The plot of centre-of-mass scattering angle versus scattering angle in the laboratory frame. Detector coverage is shown by two vertical dashed lines. (b) The Jacobian of the transformation from the laboratory frame to the centre-of-mass frame.

Chapter 5

Results and Discussion

In this section we summarize and discuss the results obtained from our study.

5.1 Differential cross section

This study is the first attempt to explore the effects of the three-nucleon (3N) force on the angular distribution of the nucleus-proton scattering for an unstable nucleus. The no-core shell model with continuum (NCSMC) based *ab initio* calculations (with chiral forces as input) were performed to predict the angular distribution of $^{10}C+p$ elastic scattering by our theory group collaborators Navratil *et al.* [87]. Here, we present the comparison of the experimental results and the preliminary theoretical predictions on the angular distribution of $^{10}C + p$ elastic scattering. The nuclear potential used in the NCSMC calculations contained chiral NN-N^{3}LO and 3N-N^{2}LO terms (see the nuclear potential diagram in figure 2.4).

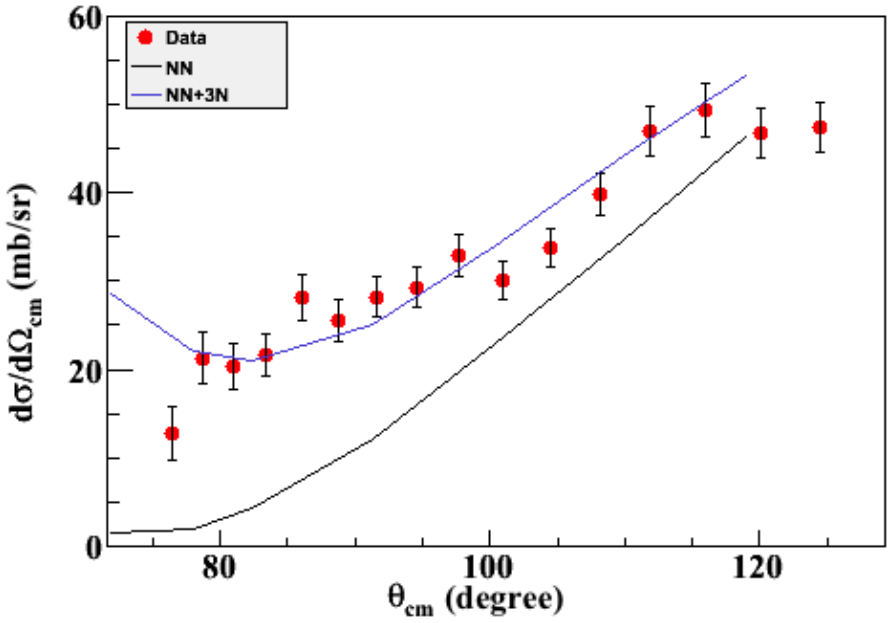

(a)

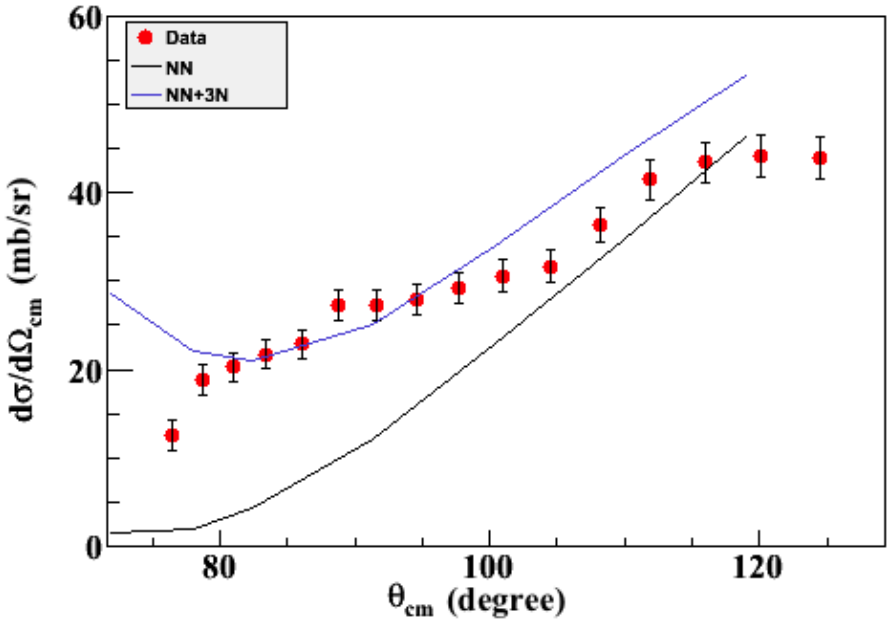

(b)

Fig. 5.1. The differential cross section of ^{10}C(p,p)^{10}C elastic reaction. The solid curves (blue and black) represent the NCSMC calculations: The black solid curve shows the calculation based on the chiral NN force (N^{3}LO), and the blue curve shows the calculation based on the chiral NN + 3N force (NN-N^{3}LO + 3N-N^{2}LO). The red dots represent the data points from the experiment.
(a) For $E_{cm} = 4.4$ MeV. (b) For $E_{cm} = 4.16$ MeV.

Using the IRIS facility, we performed the reaction ^{10}C(p,p)^{10}C with beam energy 6A MeV for two different ionization chamber (IC) pressure settings (8 and 19.5 Torr). The two different IC pressure settings result in two different

energies of ^{10}C at the entrance of the solid H_2 target. At the entrance of the solid H_2 target, the ^{10}C nuclei have energies E_{lab} = 45.45 MeV (or E_{cm}= 4.16 MeV) for 19.5 Torr IC pressure setting, and E_{lab} = 48.21 MeV (or E_{cm} = 4.4 MeV) for 8 Torr IC pressure setting. We have shown the differential cross sections for ^{10}C(p,p)^{10}C elastic reaction in figure 5.1. The theoretical calculation predicts that the differential cross section found using NN+3N chiral forces has a higher value than the one found solely based on the chiral NN forces. Therefore, the calculations also show a very strong effects of the 3N force in the elastic scattering angular distribution.

The experimentally measured cross section for E_{cm} = 4.4 MeV is well described by NN+3N force based calculation but for the energy E_{cm} = 4.16 MeV there are discrepancies between the theory and experiment for several data points. Our study claims that the experimentally observed differential cross section for both the incident ^{10}C energies can be well described by *ab initio* NCSMC model with chiral NN+3N force (see figure 5.1a and 5.1b). We observed that the effects of the 3NF are extremely significant for the lower centre-of-mass angle. For future perspective the NCSMC calculations should be extended to include the higher order terms (N^3LO and N^4LO) in the 3N forces to better understand the missing physics. However, overall the NCSMC appears to be a promising unified *ab initio* model to predict both the bound state properties as well scattering state properties of nuclei.

Bibliography

[1] R. Machleidt and D. R. Entem, "Chiral effective field theory and nuclear forces," *Physics Reports*, vol. 503, no. 1, pp. 1–75, 2011.

[2] D. Tilley, J. Kelley, J. Godwin, D. Millener, J. Purcell, C. Sheu, and H. Weller, "Energy levels of light nuclei," *Nuclear Physics A*, vol. 745, no. 3–4, pp. 155 – 362, 2004.

[3] W. Glöckle and H. Kamada, "Alpha-particle binding energies for realistic nucleon-nucleon interactions," *Phys. Rev. Lett.*, vol. 71, pp. 971–974, Aug 1993.

[4] A. Nogga, A. Kievsky, H. Kamada, W. Gloeckle, L. Marcucci, *et al.*, "The Three nucleon bound state using realistic potential models," *Phys.Rev.*, vol. C67, p. 034004, 2003.

[5] S. C. Pieper, K. Varga, and R. B. Wiringa, "Quantum monte carlo calculations of $a = 9, 10$ nuclei," *Phys. Rev. C*, vol. 66, p. 044310, Oct 2002.

[6] S. C. Pieper and R. B. Wiringa, "Quantum monte carlo calculations of light nuclei1," *Annual Review of Nuclear and Particle Science*, vol. 51, no. 1, pp. 53–90, 2001.

[7] B. S. Pudliner, V. R. Pandharipande, J. Carlson, S. C. Pieper, and R. B. Wiringa, "Quantum monte carlo calculations of nuclei with $A \leq 7$," *Phys. Rev. C*, vol. 56, pp. 1720–1750, Oct 1997.

[8] S. Coon, M. Scadron, P. McNamee, B. Barrett, D. Blatt, and B. McKellar,

"The two-pion-exchange three-nucleon potential and nuclear matter," *Nuclear Physics A*, vol. 317, no. 1, pp. 242 – 278, 1979.

[9] S. A. Coon, M. D. Scadron, and B. R. Barrett, "The Three-Body Force, Off-Shell Pion Nucleon Scattering, and Binding Energies in Nuclear Matter," *Nucl.Phys.*, vol. A242, p. 467, 1975.

[10] B. S. Pudliner, V. R. Pandharipande, J. Carlson, and R. B. Wiringa, "Quantum monte carlo calculations of $A \leq 6$ nuclei," *Phys. Rev. Lett.*, vol. 74, pp. 4396–4399, May 1995.

[11] B. R. Barrett, P. Navratil, and J. P. Vary, "Ab initio no core shell model," *Prog. Part. Nucl. Phys.*, vol. 69, pp. 131–181, 2013.

[12] C. Forssen, R. Roth, and P. Navratil, "Systematics of 2^+ states in c isotopes from the no-core shell model," *Journal of Physics G: Nuclear and Particle Physics*, vol. 40, no. 5, p. 055105, 2013.

[13] P. Navratil, S. Quaglioni, I. Stetcu, and B. R. Barrett, "Recent developments in no-core shell-model calculations," *Journal of Physics G: Nuclear and Particle Physics*, vol. 36, no. 8, p. 083101, 2009.

[14] P. Navrátil, V. G. Gueorguiev, J. P. Vary, W. E. Ormand, and A. Nogga, "Structure of $a = 10 - 13$ nuclei with two- plus three-nucleon interactions from chiral effective field theory," *Phys. Rev. Lett.*, vol. 99, p. 042501, Jul 2007.

[15] S. Baroni, P. Navrátil, and S. Quaglioni, "Unified *ab initio* approach to bound and unbound states: No-core shell model with continuum and its application to ^{7}he," *Phys. Rev. C*, vol. 87, p. 034326, Mar 2013.

[16] G. Hupin, J. Langhammer, P. Navrátil, S. Quaglioni, A. Calci, and R. Roth, "*Ab initio* many-body calculations of nucleon-^{4}he scattering with three-nucleon forces," *Phys. Rev. C*, vol. 88, p. 054622, Nov 2013.

[17] G. Hupin, S. Quaglioni, and P. Navrátil, "Unified description of ^{6}Li structure and deuterium-^{4}He dynamics with chiral two- and three-nucleon forces," *Phys. Rev. Lett.*, vol. 114, p. 212502, May 2015.

[18] H. Simon, "Halo nuclei, stepping stones across the drip-lines," *Physica Scripta*, vol. 2013, no. T152, p. 014024, 2013.

[19] R. Machleidt, "Nuclear forces," *AIP Conference Proceedings*, vol. 1541, no. 1, pp. 61–103, 2013.

[20] T. Ericson and M. Rosa-Clot, "The deuteron asymptotic d-state as a probe of the nucleon-nucleon force," *Nuclear Physics A*, vol. 405, no. 3, pp. 497 – 533, 1983.

[21] O. Haxel, J. H. D. Jensen, and H. E. Suess, "On the "magic numbers" in nuclear structure," *Phys. Rev.*, vol. 75, pp. 1766–1766, Jun 1949.

[22] M. G. Mayer, "On closed shells in nuclei," *Phys. Rev.*, vol. 74, pp. 235–239, Aug 1948.

[23] R. D. Woods and D. S. Saxon, "Diffuse surface optical model for nucleon-nuclei scattering," *Phys. Rev.*, vol. 95, pp. 577–578, Jul 1954.

[24] A. Ozawa, T. Kobayashi, T. Suzuki, K. Yoshida, and I. Tanihata, "New magic number, $N = 16$, near the neutron drip line," *Phys. Rev. Lett.*, vol. 84, pp. 5493–5495, Jun 2000.

[25] D. Steppenbeck, S. Takeuchi, N. Aoi, P. Doornenbal, M. Matsushita, H. Wang, H. Baba, N. Fukuda, S. Go, M. Honma, J. Lee, K. Matsui, S. Michimasa, T. Motobayashi, D. Nishimura, T. Otsuka, H. Sakurai, Y. Shiga, P. A. Soderstrom, T. Sumikama, H. Suzuki, R. Taniuchi, Y. Utsuno, J. J. Valiente-Dobon, and K. Yoneda, "Evidence for a new nuclear /'magic number/' from the level structure of 54ca," *Nature*, vol. 502, pp. 207–210, 10 2013.

[26] Y. H., "On closed shells in nuclei," *Proc. Phys. Math. Soc.*, vol. 17, 1935.

[27] S. Machida, S. Onuma, and M. Taketani, "On the fourth-order nuclear potential," *Progress of theoretical physics*, vol. 6, pp. 904–905, oct 1951.

[28] M. Taketani, S. Nakamura, and M. Sasaki, "On the method of the theory of nuclear forces," *Progress of Theoretical Physics*, vol. 6, no. 4, pp. 581–586, 1951.

[29] L.-B. Wang, "Determination of the helium-6 nuclear charge radius using high-resolusion laser spectroscopy," *Ph.D Thesis https://www.phy.anl.gov/mep/atta/publications/libangUwangUthesis.pdf*, 2004.

[30] N. Hoshizaki and S. Machida, "Two-nucleon potential with full recoil. ii: Two-pion-exchange potential," *Progress of Theoretical Physics*, vol. 27, no. 2, pp. 288–314, 1962.

[31] R. A. Bryan and B. L. Scott, "Nucleon-nucleon scattering from one-boson-exchange potentials," *Phys. Rev.*, vol. 135, pp. B434–B450, Jul 1964.

[32] K. Erkelenz, "Current status of the relativistic two-nucleon one boson exchange potential," *Physics Reports*, vol. 13, no. 5, pp. 191 – 258, 1974.

[33] M. M. Nagels, T. A. Rijken, and J. J. de Swart, "Low-energy nucleon-nucleon potential from regge-pole theory," *Phys. Rev. D*, vol. 17, pp. 768–776, Feb 1978.

[34] R. Machleidt, K. Holinde, and C. Elster, "The bonn meson-exchange model for the nucleon—nucleon interaction," *Physics Reports*, vol. 149, no. 1, pp. 1 – 89, 1987.

[35] M. M. Nagels, T. A. Rijken, and J. J. de Swart, "Low-energy nucleon-nucleon potential from regge-pole theory," *Phys. Rev. D*, vol. 17, pp. 768–776, Feb 1978.

[36] R. B. Wiringa, R. A. Smith, and T. L. Ainsworth, "Nucleon-nucleon potentials with and without $\delta(1232)$ degrees of freedom," *Phys. Rev. C*, vol. 29, pp. 1207–1221, Apr 1984.

[37] W. N. Cottingham, M. Lacombe, B. Loiseau, J. M. Richard, and R. V. Mau, "Nucleon-nucleon interaction from pion-nucleon phase-shift analysis," *Phys. Rev. D*, vol. 8, pp. 800–819, Aug 1973.

[38] M. Lacombe, B. Loiseau, J. M. Richard, R. V. Mau, J. Côté, P. Pirès, and R. de Tourreil, "Parametrization of the paris $n-n$ potential," *Phys. Rev. C*, vol. 21, pp. 861–873, Mar 1980.

[39] M. Lacombe, B. Loiseau, J. M. Richard, R. V. Mau, P. Pires, and R. de Tourreil, "New semiphenomenological soft-core and velocity-dependent nucleon-nucleon potential," *Phys. Rev. D*, vol. 12, pp. 1495–1498, Sep 1975.

[40] V. G. J. Stoks, R. A. M. Klomp, C. P. F. Terheggen, and J. J. de Swart, "Construction of high-quality *NN* potential models," *Phys. Rev. C*, vol. 49, pp. 2950–2962, Jun 1994.

[41] R. Machleidt, "The High precision, charge dependent Bonn nucleon-nucleon potential (CD-Bonn)," *Phys.Rev.*, vol. C63, p. 024001, 2001.

[42] R. B. Wiringa, V. G. J. Stoks, and R. Schiavilla, "Accurate nucleon-nucleon potential with charge-independence breaking," *Phys. Rev. C*, vol. 51, pp. 38–51, Jan 1995.

[43] J. Carlson and R. Schiavilla, "Structure and dynamics of few-nucleon systems," *Rev. Mod. Phys.*, vol. 70, pp. 743–841, Jul 1998.

[44] S. C. Pieper and R. B. Wiringa, "Quantum monte carlo calculations of light nuclei1," *Annual Review of Nuclear and Particle Science*, vol. 51, no. 1, pp. 53–90, 2001.

[45] J. L. Friar, G. Payne, V. Stoks, and J. de Swart, "Triton calculations with the new Nijmegen potentials," *Phys.Lett.*, vol. B311, p. 4, 1993.

[46] H. Primakoff and T. Holstein, "Many-body interactions in atomic and nuclear systems," *Phys. Rev.*, vol. 55, pp. 1218–1234, Jun 1939.

[47] J.-i. Fujita and H. Miyazawa, "Pion theory of three-body forces," *Progress of Theoretical Physics*, vol. 17, no. 3, pp. 360–365, 1957.

[48] H. T. Coelho, T. K. Das, and M. R. Robilotta, "Two-pion-exchange three-nucleon force and the ^{3}H and ^{3}He nuclei," *Phys. Rev. C*, vol. 28, pp. 1812–1828, Oct 1983.

[49] Epelbaum, E., "Four-nucleon force using the method of unitary transformation," *Eur. Phys. J. A*, vol. 34, no. 2, pp. 197–214, 2007.

[50] C. Ordóñez, L. Ray, and U. van Kolck, "Nucleon-nucleon potential from an effective chiral lagrangian," *Phys. Rev. Lett.*, vol. 72, pp. 1982–1985, Mar 1994.

[51] C. Ordóñez, L. Ray, and U. van Kolck, "Two-nucleon potential from chiral lagrangians," *Phys. Rev. C*, vol. 53, pp. 2086–2105, May 1996.

[52] U. van Kolck, "Few-nucleon forces from chiral lagrangians," *Phys. Rev. C*, vol. 49, pp. 2932–2941, Jun 1994.

[53] S. Weinberg, "Nuclear forces from chiral lagrangians," *Physics Letters B*, vol. 251, no. 2, pp. 288 – 292, 1990.

[54] S. Weinberg, "Effective chiral Lagrangians for nucleon - pion interactions and nuclear forces," *Nucl.Phys.*, vol. B363, pp. 3–18, 1991.

[55] S. Weinberg, "Three-body interactions among nucleons and pions," *Physics Letters B*, vol. 295, no. 1–2, pp. 114 – 121, 1992.

[56] S. Bacca, N. Barnea, G. Hagen, M. Miorelli, G. Orlandini, and T. Papenbrock, "Giant and pigmy dipole resonances in ^{4}He, ^{16,22}O, and ^{40}Ca from chiral nucleon-nucleon interactions," *Phys. Rev. C*, vol. 90, p. 064619, Dec 2014.

[57] L. Coraggio, A. Covello, A. Gargano, and N. Itaco, "Shell-model calculations for neutron-rich carbon isotopes with a chiral nucleon-nucleon potential," *Phys. Rev. C*, vol. 81, p. 064303, Jun 2010.

[58] L. Coraggio, A. Covello, A. Gargano, N. Itaco, T. T. S. Kuo, D. R. Entem, and R. Machleidt, "Microscopic nuclear structure based upon a chiral NN potential," *Phys. Rev. C*, vol. 66, p. 021303, Aug 2002.

[59] L. Coraggio, A. Covello, A. Gargano, N. Itaco, T. T. S. Kuo, and R. Machleidt, "Nuclear structure calculations and modern nucleon-nucleon potentials," *Phys. Rev. C*, vol. 71, p. 014307, Jan 2005.

[60] A. Deltuva and A. C. Fonseca, "*Ab initio* four-body calculation of n-^{3}He, p-^{3}H, and d-d scattering," *Phys. Rev. C*, vol. 76, p. 021001, Aug 2007.

[61] S. Fujii, R. Okamoto, and K. Suzuki, "Publisher's note: Ground-state and single-particle energies of nuclei around ^{16}**O**, ^{40}Ca, and ^{56}Ni from realistic nucleon-nucleon forces [phys. rev. lett. **103** , 182501 (2009)]," *Phys. Rev. Lett.*, vol. 103, p. 199903, Nov 2009.

[62] G. Hagen, T. Papenbrock, D. J. Dean, and M. Hjorth-Jensen, "Medium-mass nuclei from chiral nucleon-nucleon interactions," *Phys. Rev. Lett.*, vol. 101, p. 092502, Aug 2008.

[63] P. Navrátil and E. Caurier, "Nuclear structure with accurate chiral perturbation theory nucleon-nucleon potential: Application to ^{6}Li and ^{10}B," *Phys. Rev. C*, vol. 69, p. 014311, Jan 2004.

[64] A. Ekström, R. Jansen, G. A. Wendt, K. G. Hagen, T. Papenbrock, S. Bacca, B. Carlsson, and D. Gazit, "Effects of three-nucleon forces and two-body

currents on gamow-teller strengths," *Phys. Rev. Lett.*, vol. 113, p. 262504, Dec 2014.

[65] G. Hagen, M. Hjorth-Jensen, G. R. Jansen, R. Machleidt, and T. Papenbrock, "Continuum effects and three-nucleon forces in neutron-rich oxygen isotopes," *Phys. Rev. Lett.*, vol. 108, p. 242501, Jun 2012.

[66] G. Hagen, M. Hjorth-Jensen, G. R. Jansen, R. Machleidt, and T. Papenbrock, "Evolution of shell structure in neutron-rich calcium isotopes," *Phys. Rev. Lett.*, vol. 109, p. 032502, Jul 2012.

[67] H. Hergert, S. K. Bogner, S. Binder, A. Calci, J. Langhammer, R. Roth, and A. Schwenk, "In-medium similarity renormalization group with chiral two-plus three-nucleon interactions," *Phys. Rev. C*, vol. 87, p. 034307, Mar 2013.

[68] J. W. Holt, N. Kaiser, and W. Weise, "Chiral three-nucleon interaction and the ^{14}c-dating β decay," *Phys. Rev. C*, vol. 79, p. 054331, May 2009.

[69] R. Jansen, G. J. Engel, G. Hagen, P. Navratil, and A. Signoracci, "*Ab Initio* coupled-cluster effective interactions for the shell model: Application to neutron-rich oxygen and carbon isotopes," *Phys. Rev. Lett.*, vol. 113, p. 142502, Oct 2014.

[70] A. Nogga, P. Navrátil, B. R. Barrett, and J. P. Vary, "Spectra and binding energy predictions of chiral interactions for ^{7}Li," *Phys. Rev. C*, vol. 73, p. 064002, Jun 2006.

[71] T. Otsuka, T. Suzuki, J. D. Holt, A. Schwenk, and Y. Akaishi, "Three-body forces and the limit of oxygen isotopes," *Phys. Rev. Lett.*, vol. 105, p. 032501, Jul 2010.

[72] R. Roth, S. Binder, K. Vobig, A. Calci, J. Langhammer, and P. Navrátil, "Medium-mass nuclei with normal-ordered chiral nn+3n interactions," *Phys. Rev. Lett.*, vol. 109, p. 052501, Jul 2012.

[73] R. B. Wiringa, S. C. Pieper, J. Carlson, and V. R. Pandharipande, "Quantum monte carlo calculations of $a = 8$ nuclei," *Phys. Rev. C*, vol. 62, p. 014001, Jun 2000.

[74] P. Navrátil, J. P. Vary, and B. R. Barrett, "Large-basis ***ab initio*** no-core shell model and its application to ^{12}c," *Phys. Rev. C*, vol. 62, p. 054311, Oct 2000.

[75] P. Navrátil, J. P. Vary, and B. R. Barrett, "Properties of ^{12}c in the *Ab Initio* nuclear shell model," *Phys. Rev. Lett.*, vol. 84, pp. 5728–5731, Jun 2000.

[76] P. Navrátil and S. Quaglioni, "*Ab initio* many-body calculations of deuteron-^{4}He scattering and ^{6}Li states," *Phys. Rev. C*, vol. 83, p. 044609, Apr 2011.

[77] S. Quaglioni and P. Navrátil, "*Ab Initio* many-body calculations of n-^{3}H, n-^{4}He, p-^{3,4}He, and $n-^{10}$Be scattering," *Phys. Rev. Lett.*, vol. 101, p. 092501, Aug 2008.

[78] S. Quaglioni and P. Navrátil, "*Ab initio* many-body calculations of nucleon-nucleus scattering," *Phys. Rev. C*, vol. 79, p. 044606, Apr 2009.

[79] S. Baroni, P. Navrátil, and S. Quaglioni, "*Ab Initio* description of the exotic unbound ^{7}He nucleus," *Phys. Rev. Lett.*, vol. 110, p. 022505, Jan 2013.

[80] E. Epelbaum, H. Krebs, D. Lee, and U.-G. Meißner, "*Ab Initio* calculation of the hoyle state," *Phys. Rev. Lett.*, vol. 106, p. 192501, May 2011.

[81] W. E. Ormand and P. Navrátil, "*ab initio* shell model with a genuine three-nucleon force for the p-shell nuclei," September 203.

[82] D. Tilley, C. Cheves, J. Godwin, G. Hale, H. Hofmann, J. Kelley, C. Sheu, and H. Weller, "Energy levels of light nuclei a=5, 6, 7," *Nuclear Physics A*, vol. 708, no. 1–2, pp. 3 – 163, 2002.

[83] A. F. Lisetskiy, M. K. G. Kruse, B. R. Barrett, P. Navratil, I. Stetcu, and J. P. Vary, "Effective operators from exact many-body renormalization," *Phys. Rev. C*, vol. 80, p. 024315, Aug 2009.

[84] P. Navrátil and W. E. Ormand, "*Ab Initio* shell model calculations with three-body effective interactions for *p*-shell nuclei," *Phys. Rev. Lett.*, vol. 88, p. 152502, Apr 2002.

[85] P. Navrátil and E. Caurier, "Nuclear structure with accurate chiral perturbation theory nucleon-nucleon potential: Application to ^{6}Li and ^{10}B," *Phys. Rev. C*, vol. 69, p. 014311, Jan 2004.

[86] P. Navrátil, C. A. Bertulani, and E. Caurier, "^{7}be(p,γ)^{8}b *s* factor from *ab initio* no-core shell model wave functions," *Phys. Rev. C*, vol. 73, p. 065801, Jun 2006.

[87] P. N. et. al., "private communication,"

[88] R. Kanungo, "Iris: The isac charged particle reaction spectroscopy facility for reaccelerated high-energy isol beams," *Hyperfine Interactions*, vol. 225, no. 1-3, pp. 235–240, 2014.

[89] "http://www.micronsemiconductor.co.uk/pdf/s.pdf,"

[90] *Mesytec Nuclear Physics tool, Webpage: http://www.mesytec.com/datasheets/MSCF-16-F.pdf.*

[91] LISE++ *Webpage: http://lise.nscl.msu.edu.*

[92] F. Benrachi, B. Chambon, B. Cheynis, D. Drain, C. Pastor, D. Seghier, K. Zaid, A. Giorni, D. Heuer, A. Llères, C. Morand, P. Stassi, and J. Viano, "Investigation of the performance of csi(tl) for charged particle identification by pulse-shape analysis," *Nuclear Instruments and Methods in Physics Research Section A: Accelerators, Spectrometers, Detectors and Associated Equipment*, vol. 281, no. 1, pp. 137 – 142, 1989.

[93] Y. Larochelle, L. Beaulieu, B. Djerroud, D. Doré, P. Gendron, E. Jalbert, R. Laforest, J. Pouliot, R. Roy, M. Samri, and C. St-Pierre, "Energy-light relation for csi(t1) scintillators in heavy ion experiments at intermediate energies," *Nuclear Instruments and Methods in Physics Research Section A: Accelerators, Spectrometers, Detectors and Associated Equipment*, vol. 348, no. 1, pp. 167 – 172, 1994.

[94] A. Wagner, W. Tan, K. Chalut, R. Charity, B. Davin, Y. Larochelle, M. Lennek, T. Liu, X. Liu, W. Lynch, A. Ramos, R. Shomin, L. Sobotka, R. de Souza, M. Tsang, G. Verde, and H. Xu, "Energy resolution and energy–light response of csi(tl) scintillators for charged particle detection," *Nuclear Instruments and Methods in Physics Research Section A: Accelerators, Spectrometers, Detectors and Associated Equipment*, vol. 456, no. 3, pp. 290 – 299, 2001.